INFORMATION TO USERS

This manuscript has been reproduced from the microfilm master. UMI films the text directly from the original or copy submitted. Thus, some thesis and dissertation copies are in typewriter face, while others may be from any type of computer printer.

The quality of this reproduction is dependent upon the quality of the copy submitted. Broken or indistinct print, colored or poor quality illustrations and photographs, print bleedthrough, substandard margins, and improper alignment can adversely affect reproduction.

In the unlikely event that the author did not send UMI a complete manuscript and there are missing pages, these will be noted. Also, if unauthorized copyright material had to be removed, a note will indicate the deletion.

Oversize materials (e.g., maps, drawings, charts) are reproduced by sectioning the original, beginning at the upper left-hand corner and continuing from left to right in equal sections with small overlaps. Each original is also photographed in one exposure and is included in reduced form at the back of the book.

Photographs included in the original manuscript have been reproduced xerographically in this copy. Higher quality 6" x 9" black and white photographic prints are available for any photographs or illustrations appearing in this copy for an additional charge. Contact UMI directly to order.

UMI

USE OF SYNTHETIC APERTURE RADAR IN ESTIMATION

OF WAVE CLIMATE FOR COASTAL ENGINEERING DESIGN

A

THESIS

Presented to the Faculty

of the University of Alaska Fairbanks

in Partial Fulfillment of the Requirements

for the Degree of

DOCTOR OF PHILOSOPHY

By

Jill Ellen Blackstone, B.S.
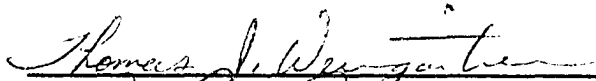
Fairbanks, Alaska

August 1995

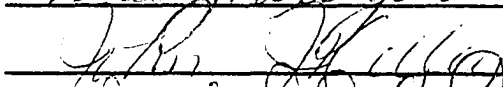UMI Number: 9608417

UMI

300 North Zeeb Road
Ann Arbor, MI 48103

Use of Synthetic Aperture Radar in Estimation of Wave Climate for Coastal Engineering Design

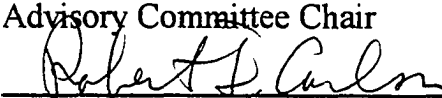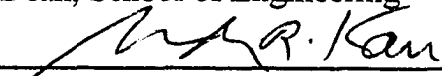**By: Jill Ellen Blackstone**

Recommended:

Advisory Committee Chair

Department Head

Approved:

Dean, School of Engineering

Dean of the Graduate School

7 - 28 - 95

Date

Abstract

Development of Alaska's maritime resources requires design of efficient, reliable, safe facilities by coastal engineers who have a thorough knowledge of site specific wave climate: wave height, length, period, direction, and storm duration. Unfortunately, lack of wave information and validated hindcast models along the Alaskan coast often results in costly overdesigned facilities or underdesigned coastal structures which have a high risk of performance failure. To expand the nearshore wave climate availability, use of spaceborne synthetic aperture radar (SAR) data to estimate wave parameters was evaluated.

SAR data were examined in raw and filtered forms, and the extracted wave climate compared to field measured data at three sites. Based on this comparison, the applications and limitations of SAR estimated parameters were established and incorporation of the information into current design practice was addressed.

SAR based spectra were dominated by low frequency spectral peaks, likely due to random noise associated with SAR images, as these peaks were not present in the

iii

field measured spectra. Due to discrepancies between SAR and measured spectra, wave height, and storm duration could not be determined. Although error ranged from 12.5% to over 100% for SAR estimated wave lengths, the fact that wave lengths, although inaccurate, could be determined from SAR is promising. SAR based wave direction compared favorably to theoretical propagation directions which affirms the potential of wave parameter extraction from SAR data. However, directional field data were not available for comparison. Due to the current errors associated with SAR based wave estimations, SAR estimated wave climate cannot be incorporated into coastal design practice at this time.

Research results suggest SAR data still hold great potential for estimating wave parameters. Examination of SAR based wave climate in an extensively monitored, open ocean setting would be beneficial, and the influence of environmental factors on SAR imaging of waves warrants additional investigation. Furthermore, development of a tandem SAR platform with temporal resolution on the order of seconds would be useful for wave period estimation and interferometric wave height determination. After this background research has been accomplished, another evaluation of SAR based nearshore wave climate would be worthwhile.

Table of Contents

List of Figures

List of Tables

Definition of Symbols and Variables

a =   Wave amplitude as measured about the still water line [L]

a_n =   Amplitude of the nth wave as measured about the still water line [L]

b   =   Distance between wave rays [L]

c   =   Propagation speed of electromagnetic radiation [L/t]

C   =   Wave celerity [L/t]

C_g =   Group velocity defined by Cn [L/t]

cn(u)   =   Jacobian elliptic function

d   =   Water depth measured from the still water line [L]

D   =   Antenna diameter [L]

D   =   Set of numerical intensity values collected by SAR sensor

E   =   Average total energy per unit area $[m/t^2]$

E_w =   Total energy per unit width $[mL/t^2]$

g   =   Gravitational constant $[L/t^2]$

H   =   wave height as measured from crest to trough [L]

i   = $\sqrt{-1}$

k   =   Wave number equal to $2\pi/L$ where L is the wave length [1/L]

k   =   Function of amplitude, a, wave length, L, and water depth, d

k_n =   Wave number of the nth wave equal to $2\pi/L_n$ where L_n is the wave length

                   of the nth wave

KE   =   Average kinetic energy per unit area [m/t²]

L   =   Wave length [L]

                   When used as [L] denotes units of length

m   =   Any positive integer

M   =   Number of rows in matrix

n   =   Ratio relating the group speed to the celerity of a single wave

                   equal to $\dfrac{1}{2}\left[1 + \dfrac{2kd}{\sinh(2kd)}\right]$

n   =   Number of rows

n   =   Number of rows and number of columns in the original matrix

N   =   Number of samples

N   =   Number of columns in matrix

PE   =   Average potential energy per unit area [m/t²]

R_r =   Range resolution as measured along the ground surface [L]

R_{rs} =   Slant range resolution measured along the direction of pulse propagation

                   [L]

S   =   Slant range distance to the object from the sensor [L]

t   =   Time [t]

t   =   Time required for signal to leave and return to the sensor [t]

T   =   Period [t]

u	=	0, 1, 2, ..., M-1
u	=	0, 1, 2, ..., N-1
u	=	Row of interest in transformed matrix
v	=	0, 1, 2, ..., N-1
v	=	Column of interest in transformed matrix
x,y	=	Distances traveled measured along perpendicular axes [L]
x	=	Row of interest in the original matrix
x	=	0, 1, 2, ..., N-1
x	=	0, 1, 2, ..., M-1
x	=	Distance in the direction of wave propagation [L]
y	=	Column of interest in original matrix
y	=	0, 1, 2,..., N-1

γ	=	Depression angle [rad]
ϵ_n	=	Phase of the nth wave
η	=	Water surface elevation referenced to the still water level [L]
$\eta(t)$	=	Water surface elevation as a function of time, t, referenced to the still water level [L]
$\eta(x,y,t)$	=	Water surface elevation as a function of time and direction, referenced to the still water level [L]
λ	=	Wavelength of the propagating pulse [L]
ρ	=	Density of water [m/L^3]
σ	=	Angular wavae frequency equal to $2\pi/T$ where T is the wave period [1/t]
σ_n	=	Angular wave frequency of the nth wave equal to $2\pi/T$ where T is the wave period [1/t]

τ =   Duration of the transmitted pulse [t]

ϕ =   Incidence angle [deg]

ϕ_n =   Angle between x^{th} axis and wave propagation direction [rad]

$f(x)$ =   Numerical intensity value collected by SAR sensor and assigned to a given pixel, x

$F(k,X)$ =   Notation for elliptic integral of the first kind with modulus k and Jacobian amplitude X. Note k = function of amplitude, wave length, and water depth and is not equal to the wave number.

$\mathscr{F}$ =   Average energy flux $[mL/t^3]$

$\mathfrak{S}[f(x,y)]$=   Two dimensional discrete Fourier Transform F(u,v)

$\mathfrak{S}[f(x)]$ =   Discrete Fourier Transform of f(x) given by F(u)

[deg]   =   Units of degrees

[L]   =   Units of length

[m]   =   Units of mass

[rad]   =   Units of radians

[t]   =   Units of time

Acknowledgments

I would not have been able to complete this research without the guidance and support of several people and the funding from several agencies. My husband, Brad Blackstone, deserves so much for his patience, support, and assistance with the figures included in this report. Thank you. I would also like to thank my parents, John and Kay Abrams, for the countless hours they spent editing this dissertation. Throughout the entire project Dr. Robert Carlson has been a wonderful mentor, giving me freedom to make my own decisions and mistakes, nudging me when I ran behind schedule, and encouraging me to catch up. I have learned so much, not only about engineering, but about life from him. He will forever have my respect. Chris Yerkes', visiting professor of electrical engineering, knowledge of and patient ability to explain SAR signal processing, as well as his contribution of Matlab code were crucial to the completion of this project. A special thanks is deserved by the other members of my graduate committee: Dr. John Kelley, Dr. Thomas Weingartner, Ken Dean, and Dr. Mohamed Succarieh. I also owe Shari George, the systems manager

xxi

of ADVAL, so much for her time, guidance, and friendship. Dr. Orson Smith of the Corps of Engineers and Dr.John Kelley of the Institute of Marine Science deserve special acknowledgment for installation of a WaveRider Buoy in Resurrection Bay. Additionally, thank you to Harvey Smith and Ruth Carter, the State Coastal Engineers for DOT, Dennis Nottingham of Peratrovich, Nottingham and Drage, the staff at the School of Engineering, faculty and staff at the Geophysical Institute, and all those who prayed for me.

My sincere thanks to all of you who helped me complete this project.

Introduction

The coastal zone of Alaska holds vast amounts of this Nation's maritime resources. All of the marine industries require coastal facilities which must be designed for efficiency, reliability, and safety. Conversations with Alaskan coastal engineers confirm that the general lack of wave data available for the State makes it difficult to accomplish this goal (Britch 1994; Nottingham 1994; Smith, H. 1994; Smith, O. 1993).

The primary coastal design consideration is wave climate: wave spectra, height, length, period, direction, and duration of wave storm events. The long period waves of tsunamis, tides, and storm surges determine the nature of coastal flooding, current movements, safety of transportation routes and placement of port facilities. Short period waves and swells caused by intense storm activity are important for the placement of harbors and docking facilities, and sediment movement. Efficient and safe design of coastal structures requires a thorough knowledge of the local wave and

1

current climate (McDonald 1988; CERC 1984). Each coastal facility design requires the prediction, in a statistical sense, of the wave and current parameters which may be expected during the life of the project (CERC 1984).

Currently, limited wave and wind data can be obtained from archives at the Arctic Environmental Information and Data Center (AEIDC), Anchorage, Alaska, harbor master logs, and wind records from anemometers around the state (Britch 1994; Smith, O. 1994). In some cases the only data available are sporadic wind speeds recorded at airports located miles inland (Smith, O. 1993). All coastal engineering firms that were consulted used the methods described in the *Shore Protection Manual* (CERC 1984) for conversion of wind speeds to nearshore wave heights. Both the measured waves and the converted wind data are limited in their usefulness because only a single wave height is determined rather than an entire wave spectrum (Nottingham 1994; Smith, H. 1994). An additional concern raised by engineers is the lack of an official archiving system where reduced data can easily be stored and accessed. The lack of a central archiving system has resulted in multiple engineering firms reducing identical wind data to wave climate without the knowledge that others have performed the same transformations (Nottingham 1994).

Alaska's economic future is heavily dependent on resource development in its coastal zone. Fisheries, mining development, petroleum development and critical transportation links depend on the design and construction of coastal facilities. Spaceborne SAR products have the potential to greatly increase the effectiveness of coastal engineering design by providing site-specific wave climate consisting of wave height, wave length, wave direction, wave period, and duration of storm events. This would save state and federal governments considerable money. The goal of this study was to evaluate the feasibility of converting synthetic aperture radar (SAR) data into useable wave climate information for coastal engineering.

Background

The use of synthetic aperture radar (SAR) to examine nearshore ocean waves is an interdisciplinary pursuit involving a thorough understanding of coastal engineering and remote sensing. To facilitate the reader's comprehension of the combined topic, a summary of basic coastal engineering and remote sensing topics pertinent to the study has been assembled.

2.1 Coastal Engineering

The coastal engineering field is based on the practical application of oceanographic concepts to coastal facility design. Central concepts of the field include wave theory, spectral descriptions of the ocean surface, modification of waveforms as they propagate shoreward, energy associated with waves, and prediction of expected wave climate.

2.1.1 Wave Theory

Numerous wave theories exist describing water particle motion and the displacement of the water surface due to the passage of a wave: Airy, cnoidal, solitary, Stokes, and trochoidal.

2.1.1a Airy Theory

The Airy wave theory, also known as the sinusoidal or linear wave theory, describes simple waves having relatively small heights in comparison to water depth, and is given by the following equation.

$$\eta = a\cos[kx - \sigma t] \tag{2.1}$$

where η = water surface elevation referenced to the still water level [L]

a = wave amplitude as measured about the still water line [L]

k = wave number equal to $2\pi/L$ where L is the wave length [1/L]

x = distance in the direction of wave propagation [L]

σ = angular wave frequency equal to $2\pi/T$ where T is the period [1/t]

t = time [t]

Water particle motion is assumed to be orbital, which implies there is no net transport of water or particulates and equal water surface displacements above and below the still water level. This is shown in Figure 2.1.
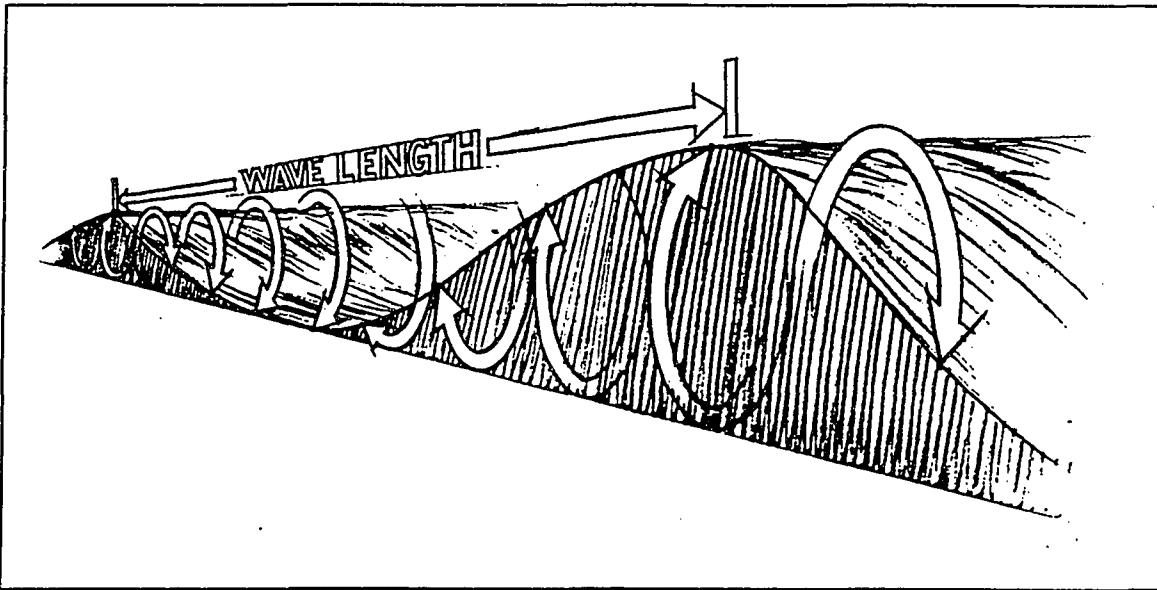
Figure 2.1. Orbital water particle motion due to the passage of a linear wave (Kampion 1989; illustration by Phil Roberts).

Additional assumptions of linear wave theory are listed below.

1) The fluid is homogeneous and incompressible.

2) Surface tension is negligible.

3) Coriolis forces are negligible.

4) Pressure at the free surface is constant.

5) The fluid may be considered inviscid due to the small water velocity gradient in the vertical direction.

6) The wave of interest does not interact with any other waves.

7) The bathymetric contours of the ocean floor are straight and parallel, or the water depth is large enough that surface waves are not influenced by the ocean

8) Waveform is invariant in time and space.

9) Waves are plane and long crested.

For the purposes of coastal engineering, the first five assumptions may be made without significantly compromising accuracy. Assumption 6 is not realistic because the sea surface is a result of a number of wave trains interacting and reinforcing each other. In reality, a single wave train may not be isolated from the others as illustrated in Figure 2.2. Therefore this assumption does introduce some error. Assumption 7, that the ocean floor is horizontal and fixed is approximately true provided the sea floor has a slope of less than 1 vertical to 10 horizontal. Waveform is not truly invariant as suggested in number 8 due to the effects of shear stress generated as the form passes over the seafloor, and permeability of the floor. However, for engineering purposes these effects may usually be safely neglected. The final assumption implies the waveforms are two dimensional, and although this is not true in the open ocean, this assumption is often valid for nearshore waves.
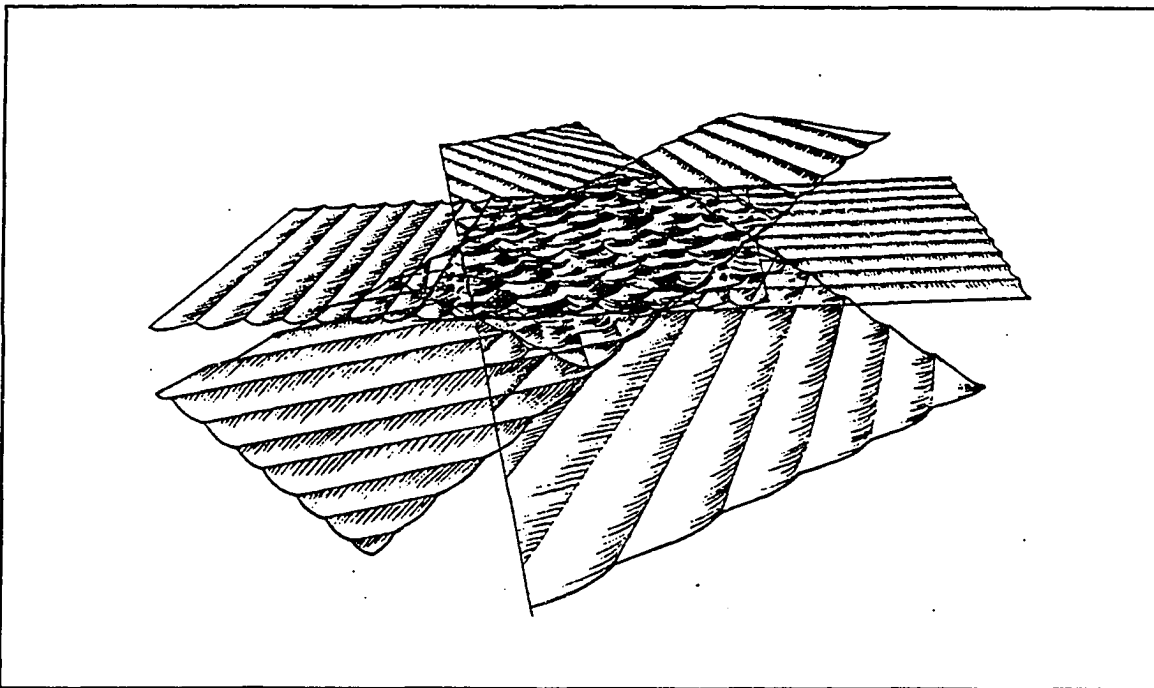
Figure 2.2. Numerous wave trains interact to form a confused sea surface (Kampion 1989; illustrated by Phil Roberts).

2.1.1b Cnoidal Wave Theory

The cnoidal wave theory describes waves in shallow water and predicts their profile from the Jacobian elliptic integral, cn(u). To be consistent with the sinusoidal or Airy theory, the shallow water theory was termed cnoidal. The water surface profile is given by the following equation (Dean and Dalrymple 1991).

$$\eta = a\ cn^2[F(k,X)] \tag{2.2}$$

where η = water surface elevation referenced to the still water level [L]

a = wave amplitude as measured about the still water line L]

cn(u) = Jacobian elliptic unction

F(k,X) = notation for elliptic integral of the first kind with modulus k

and Jacobian amplitude X

k = function of amplitude, a, wave length, L, and water depth, d

Unlike Airy waves, the crests and troughs of the cnoidal theory are not distributed symmetrically about the still water line. Approximate profiles of cnoidal waves are provided in Figure 2.3. The cnoidal theory is fairly accurate for calculating waveform variation as it moves shoreward; however, due to its complexity this method has seldom been used in coastal engineering. The advantage of providing a more realistic estimation of the waveform does not warrant its use.

$\dfrac{y_s - y_t}{H}$

Note: $k^2 = 1\text{-}10^{-2} = 1\text{-}0.01 = 0.99$
$k^2 = 1\text{-}10^{-4} = 1\text{-}0.001 = 0.999$

Location of still water level

$\dfrac{x}{L}$
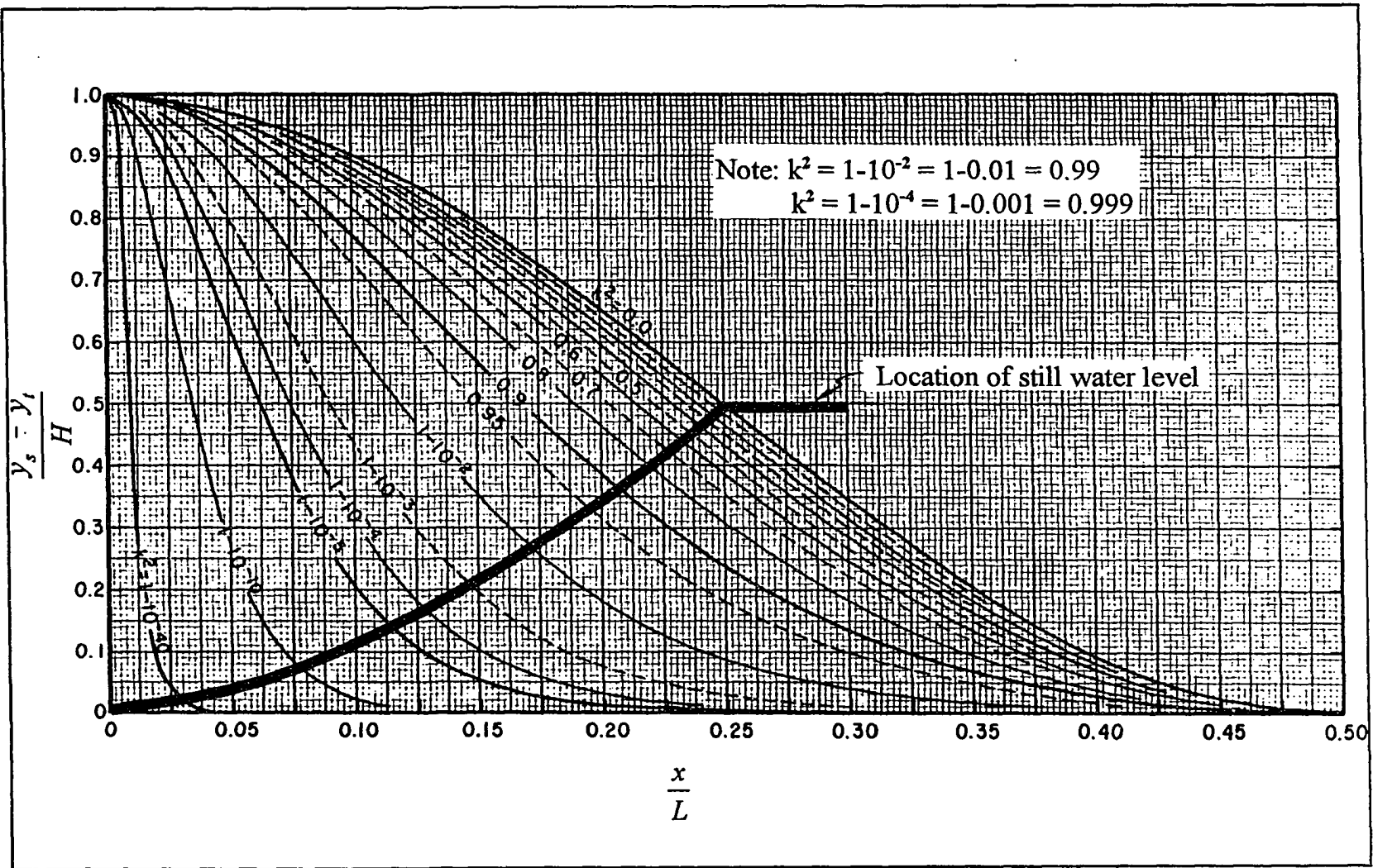
Figure 2.3. Cnoidal wave surface profiles (CERC 1984). *Note: In the above diagram k is the wave number, $2\pi/L$, and is not equal to the variable k in Equation 2.2.*

2.1.1c Solitary Wave Theory

The solitary wave theory is the shallow water extreme of the cnoidal theory, and therefore has the same limitations as the cnoidal theory. This theory describes the water surface displacement with the following equation (Dean and Dalrymple 1991).

$$\eta = a\ sech^2\left[x\ \sqrt{\frac{3\ a}{4\ d^3}}\right] \qquad (2.3)$$

where η = water surface elevation referenced to the still water level [L]

   a = wave amplitude as measured about the still water line [L]

   d = water depth measured from the still water line [L]

   x = distance traveled in the direction of wave propagation [L]

The solitary wave theory takes the asymmetrical characteristic of the cnoidal wave to the extreme in that the trough is nonexistent. Solitary waves are not oscillatory, and thus lend themselves to the description of tsunamis. The waveform is pictured in Figure 2.4.
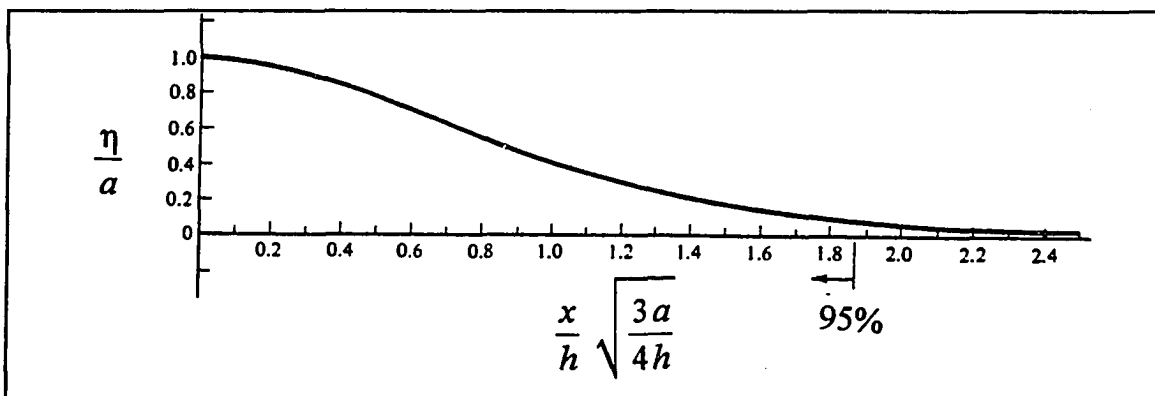
Figure 2.4. Dimensionless free surface profile of a solitary wave (Dean and Dalrymple 1991).

2.1.1d Stokes Wave Theory

The Stokes theory is a higher order wave theory which is used to evaluate finite amplitude waves through a summation process. An initial approximation is made, and depending on the precision desired, a number of successive approximations are used to correct the initial estimation. The first order approximation of this theory is simply the Airy theory discussed previously. The second order displacement of the water surface is given by the following equation (Dean and Dalrymple 1991).

$$\eta = \frac{H}{2}\cos(kx-\sigma t) + \frac{H^2}{16}\frac{\cosh(kd)}{\sinh^3(kd)}[2+\cosh(2kd)]\ \cos^2(kx-\sigma t) \quad (2.4)$$

where η = water surface elevation referenced to the still water level [L]

H = wave height as measured from crest to trough [L]

k = wave number equal to $2\pi/L$ where L is the wave length [1/L]

x = distance in the direction of wave propagation [L]

σ = angular wave frequency equal to $2\pi/T$ where T is the period [1/t]

t = time [t]

d = water depth as measured from the still water line [L]

The Stokes theory describes steep waves in deep water. The resulting wave profile is more peaked at the wave crests and flatter in the trough than the first order Stokes wave, or Airy wave. This is illustrated in Figure 2.5. As the order increases, the waveform tends to become less symmetrical about the still water line, with the maximum crest height exceeding the maximum trough depth.
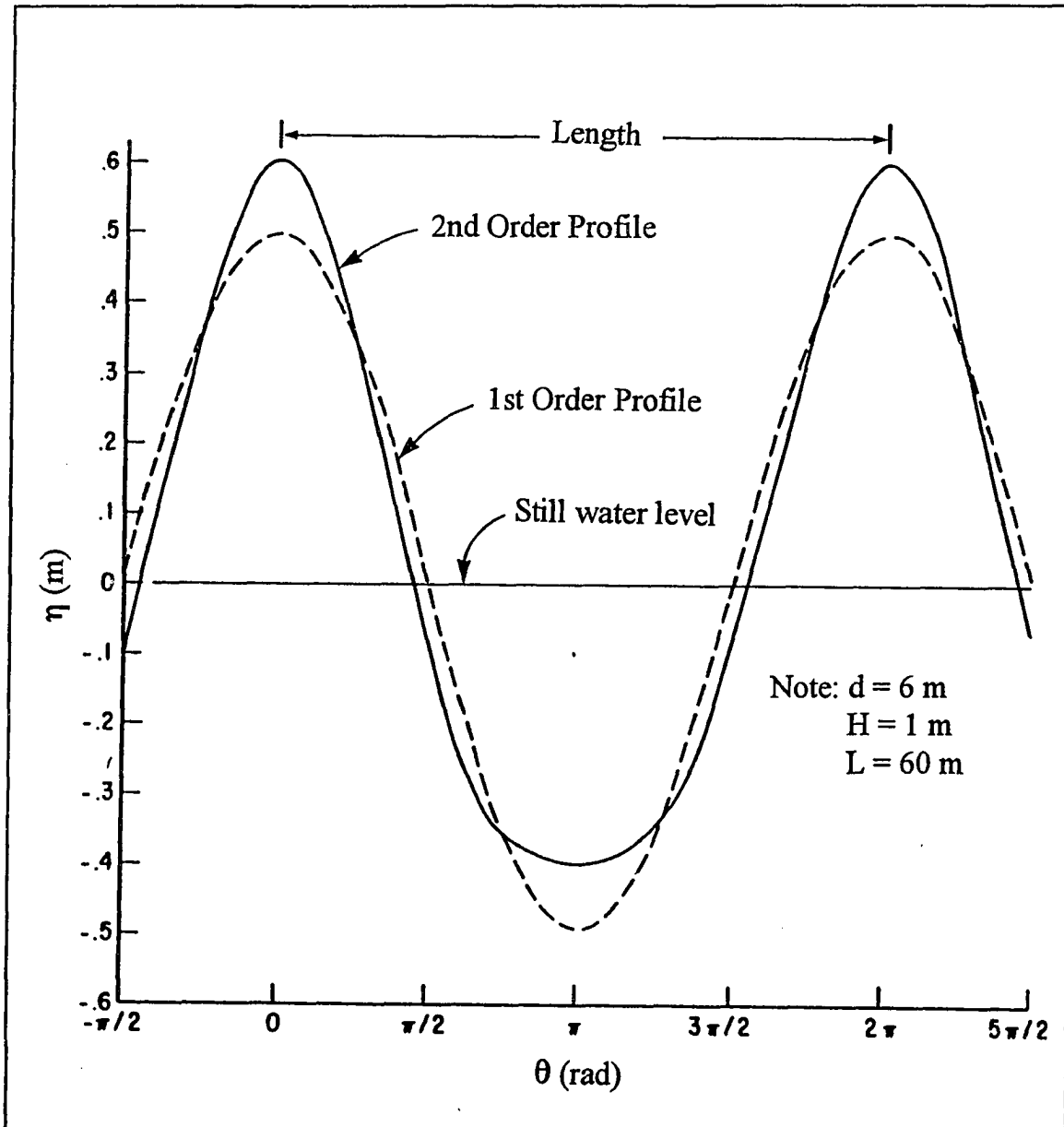
Figure 2.5. Comparison of the second order Stokes profile with the Airy theory profile (CERC 1984).

2.1.1e Trochoidal Wave Theory

The trochoidal theory, like the Stokes theory, is a finite amplitude theory which does predict the water surface profile quite accurately, but does not provide a

realistic description of the water particle motion. It is therefore not recommended for engineering purposes. The water profile predicted has the shape of a trochoid, the curve traced by a point on the perimeter of a disk as the disk rolls across a flat surface. A trochoid is shown in Figure 2.6.
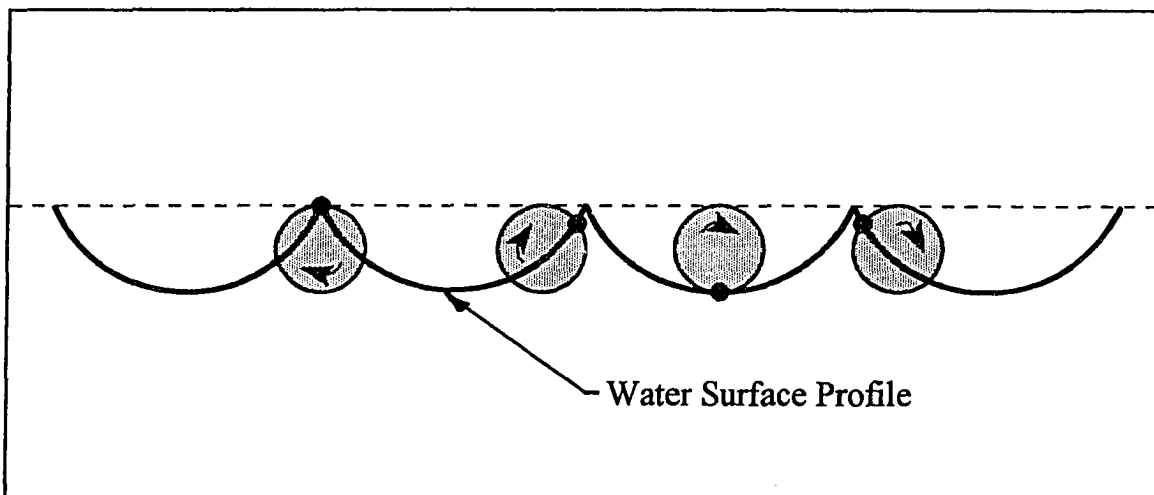
Figure 2.6. Wave profile predicted by the trochoidal wave theory.

2.1.1f Practical Application of Wave Theory

Based on the minimal advantages associated with the more rigorous theories, coastal engineers typically employ the Airy theory. The *Shore Protection Manual* (CERC 1984) states, "When concern is primarily with the oscillatory character of waves, estimates of amplitude and period must be determined from empirical data. In such problems, the uncertainty of the accurate wave height and period leads to a greater uncertainty of the ultimate answer than does neglecting the effect of nonlinear processes. Therefore, it is unlikely that the extra work involved in using nonlinear theories is justified."

2.1.2 Dispersion Relationship

Celerity is the rate at which a single wave propagates and is given by the following equation.

$$C = \frac{L}{T} \tag{2.5}$$

where C = wave celerity [L/t]

L = wave length [L]

T = period [t]

As a field of waves propagates, waves of different frequencies tend to separate, and regroup based on their varying celerities. An equation describing this phenomena relates the wave period to the wave length and the water depth at the point of interest, and is based on the solution to the linearized water wave boundary problem for a horizontal bottom. This relationship is referred to as the dispersion equation and is given below.

$$\sigma^2 = gk\tanh kd \tag{2.6}$$

where σ = angular wave frequency equal to 2π/T where T is the period [1/t]

g = gravitational constant [L/t²]

k = wave number equal to 2π/L where L is the wave length [1/L]

d = water depth as measured from the still water line [L]

2.1.3 Wave Spectra

Because wave data collected by wave buoys or measured at wave gages are

composed of a multitude of waves each with different characteristics, the information is typically summarized into a compact, useful form known as the wave spectrum. The recorded data are actually a summation of information collected from waves having different frequencies, amplitudes and phases, and may be mathematically represented by the following equation (Dean and Dalrymple 1991).

$$\eta(t) = \sum_{n=0}^{\infty} a_n \cos(\sigma_n t - \epsilon_n) \qquad (2.7)$$

where $\eta(t)$ = water surface elevation as a function of time, t, referenced to the still water level [L]

a_n = amplitude of the nth wave as measured about the still water line [L]

σ_n = angular wave frequency of the nth wave equal to $2\pi/T$ where T is period [1/t]

t = time [t]

ϵ_n = phase of the nth wave

The graph of the wave amplitude versus angular wave frequency is the amplitude spectrum, while the graph of one half the amplitude squared divided by the change in wave frequency versus the frequency is the energy density spectrum. The amplitude and energy spectra are illustrated in Figure 2.7. The energy spectrum provides a clear picture of the wave frequencies associated with the greatest energy. From the point at which peak energy occurs, the water particle velocities and accelerations can be computed, which in turn, can be used to estimate forces on coastal structures (CERC 1984).

(A) Wave amplitude spectrum   (B) Wave energy spectrum
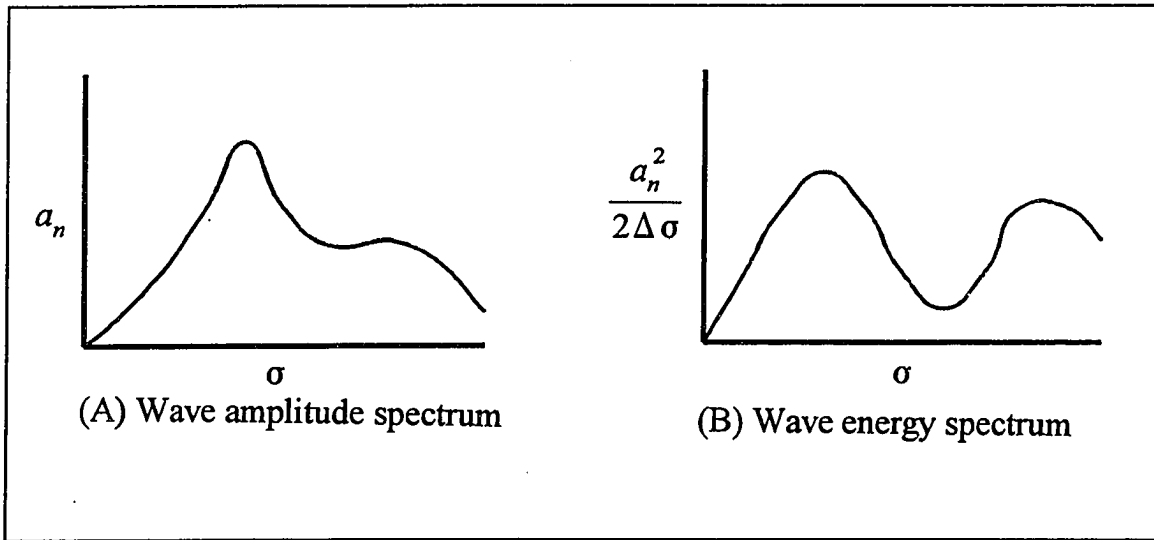
Figure 2.7. Wave spectra, where a_n is the amplitude of the nth wave and σ is the angular wave frequency equal to $2\pi/T$. T is the wave period.

Directional wave spectra, which takes the energy spectra one step further to include the varying directions of traveling waves, provides a more complete description of the wave field. The equation used to calculate the directional spectrum is given below.

$$\eta(x,y,t) = \sum_{n=0}^{\infty} a_n \cos[\sigma_n t - \phi_n - k_n(x \cos\epsilon_n + y\sin\epsilon_n)] \qquad (2.8)$$

where $\eta(x,y,t)$ = water surface elevation as a function of time and direction referenced to the still water level [L]

x,y = distances traveled measured along perpendicular axes [L]

a_n = amplitude of the nth wave as measured about the still water line [L]

σ_n = angular frequency of nth wave equal to $2\pi/T$ where T is period [1/t]

$$t = \text{time [t]}$$

ϕ_n = angle between x^{th} axis and wave propagation direction [rad]

k_n = Wave number of the nth wave equal to $2\pi/L_n$ where L_n is the wave length of the n_{th} wave [1/L]

ϵ_n = phase of the nth wave

The directional spectra, although more involved than the energy spectra allow for more efficient coastal design by indicating the direction in which the wave force will act (CERC 1984).

2.1.4 Shoaling and Refraction

As a wave generated in deep water moves toward the shore and shallower water, the wave begins to interact with the ocean floor. This interaction causes drag on the waveform, tending to slow its progression. It can be shown that the period of a given wave remains constant as it moves shoreward; therefore, from Equation 2.5, the wave length must decrease as the wave moves shoreward. Additionally the wave height increases due to the slowing of the wave and its decreasing length. This phenomena is referred to as shoaling.

Because the waveforms are modified as the wave propagates inshore, the spectra change as well. Khandekar (1989) describes two models that estimate this variation, one developed by Wang and Yang, and the other by Shemdin, et al. The Wang and Yang model includes the effects of bottom friction, an empirical wave breaking criterion which limits wave growth, and assumes straight and parallel bathymetric contours. This model, verified with data gathered during the Joint North Sea Wave Project (JONSWAP), concluded spectral peaks remain at the same frequency as the waves progress shoreward. However, the power (m^2/s) associated with the peaks increased due to shoaling. The second study, conducted by Shemdin,

et al., included wave generation, bottom friction, wave interaction, percolation, and modification of the seafloor due to waves. This study is considered the most complete analysis of spectral transformation and was verified by JONSWAP data as well. The results and indicated a slight shift of the spectral peaks toward higher frequencies and a decrease in power (m²/Hz) associated with the peaks as the waves progressed shoreward.

If the bottom nearshore bathymetric contours are straight and parallel to the incoming wave, the waveform slows uniformly along its crest, and maintains original orientation. However, if the incoming waveform is not parallel to the bottom contours, the portion of the wave crest that meets the shallower water first will slow its progression before that part of the wave which remains in deeper water. Because one portion of the wave is moving more slowly than the other, the wave crest tends to bend until it eventually approaches the beach nearly parallel to the bottom contours. This bending of the waveform is called refraction and is illustrated in Figure 2.8.
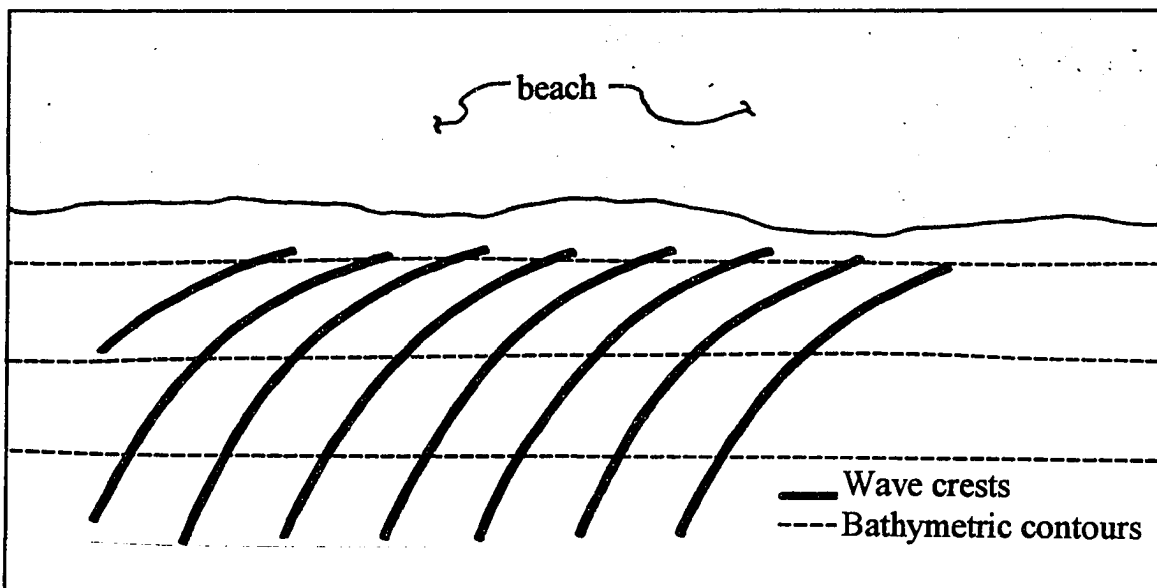
Figure 2.8. Refraction of waveforms along a uniform coastline resulting from variations in celerity along the waveform.

Carrying refraction one step further, modification of the waveform due to underwater ridges and valleys may be visualized. If a ridge exists under water, the waveform will attempt to approach parallel to the ridge. This causes the waveform to bend concavely around the ridge as illustrated in Figure 2.9. On the other hand, if a valley exists under water, the waveform will tend to enter in a convex fashion as illustrated in Figure 2.10. Figure 2.11 illustrates the directional variations of wave propagation along a coastline with headlands and bays.
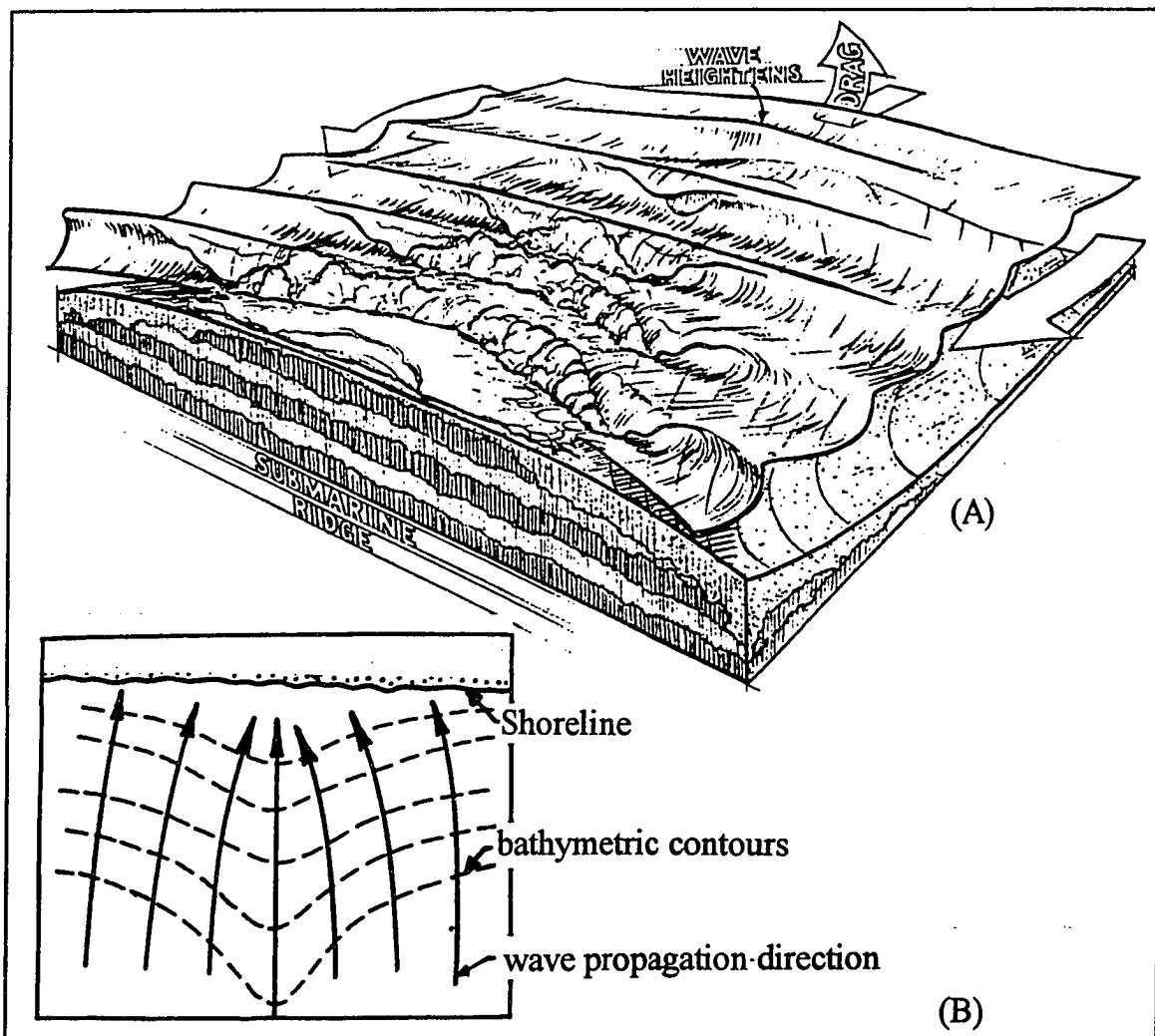
Figure 2.9. Refraction of waves around a submarine ridge. (A) depicts the waveforms (Kampion 1989; illustrated by Phil Roberts) while (B) illustrates refraction of the wave crests and focus of wave energy (CERC 1984).
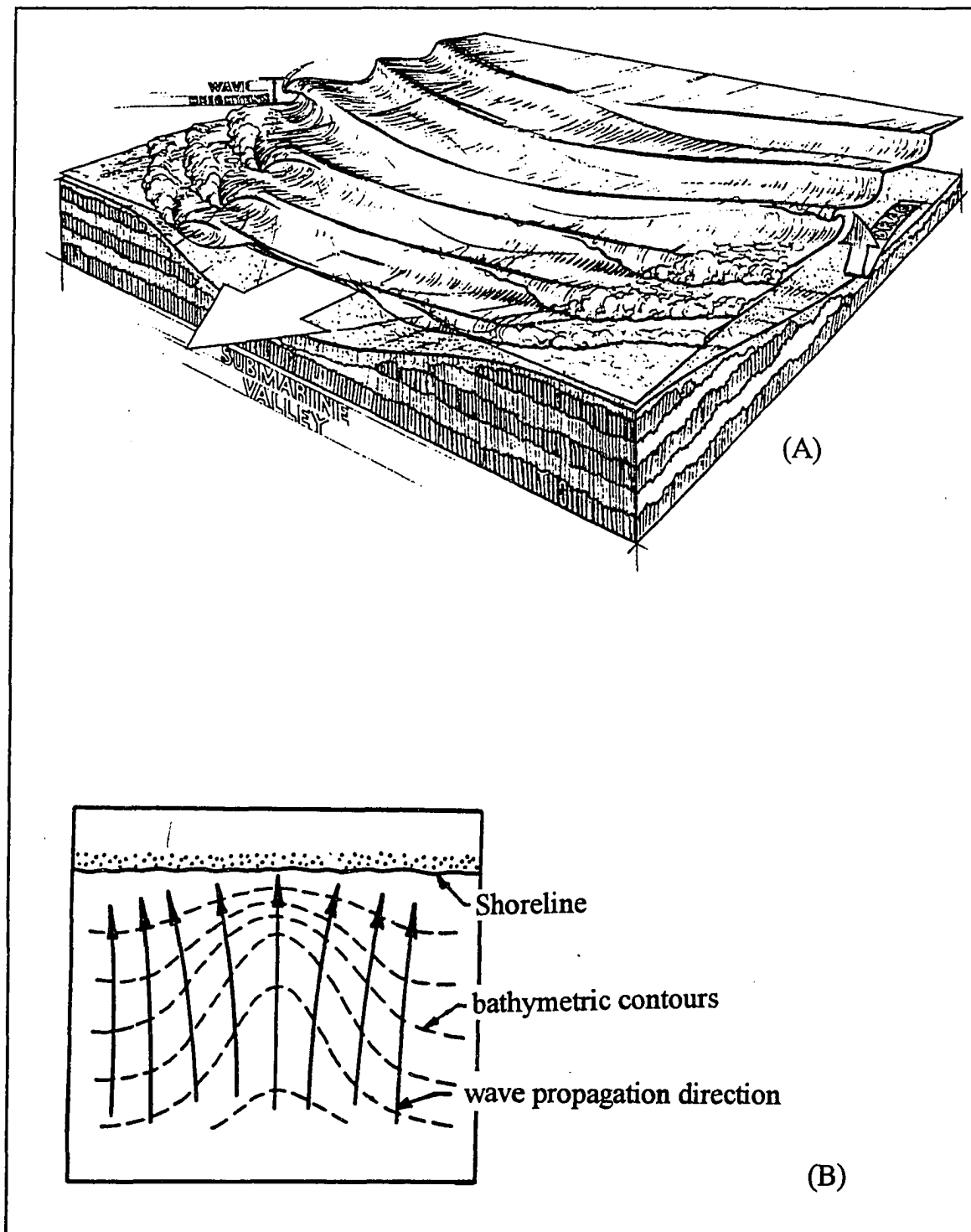
Figure 2.10. Refraction of waves due to an undersea valley. (A) depicts the waveforms (Kampion 1989; illustrated by Phil Roberts) while (B) illustrates the refraction of the wave crests and dispersion of wave energy (CERC 1984).
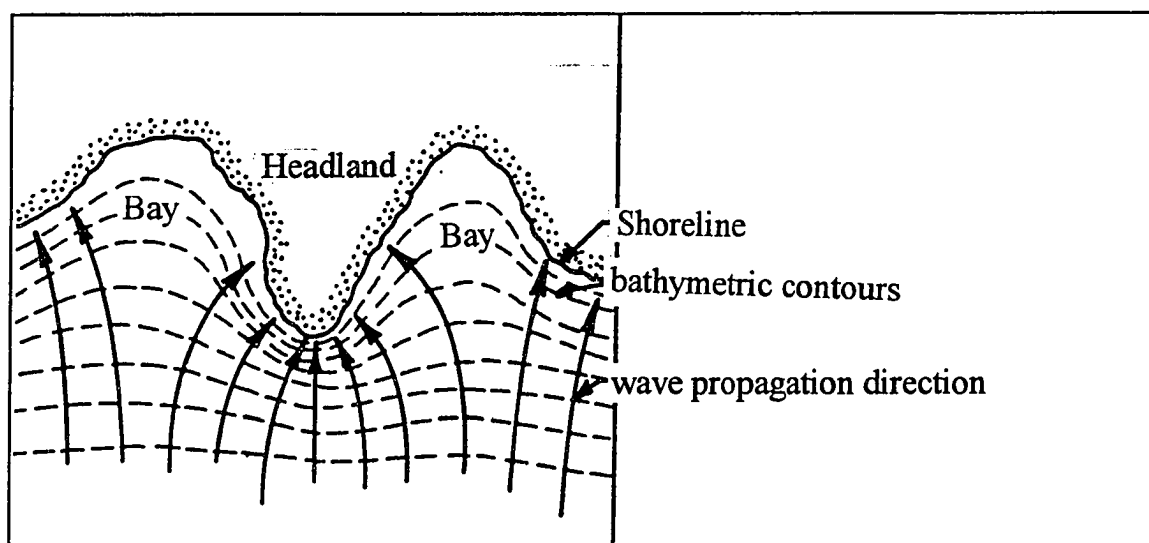
Figure 2.11. Refraction of waves due to an irregular coast (CERC 1984).

The influences of shoaling and refraction on coastal engineering are listed below:

1) Shoaling of a deep water wave determines the height the waveform will attain as it approaches the nearshore. From wave height, the wave force expected to act on a structure may be estimated.

2) As the waveform passes over bathymetric features and refracts, the focus of the wave energy is altered. As the wave bends inwardly passing over a valley, the energy is concentrated; conversely, energy is dispersed by a submarine ridge. Knowledge of the focus of wave energy also contributes to the estimation of wave forces on structures.

3) Because the local bathymetry affects the waveform so strongly, the arrangement of the waveform can be observed and the local bathymetry

may be inferred. This is important for location of structures and shipping routes.

4) Just as bathymetry modifies the characteristics of the waveform, so waves alter bathymetry. Erosion and deposition may be inferred from refraction of the waves.

2.1.5 Wave Energy

The total energy in a wave is a combination of kinetic and potential energy. The kinetic energy is due to the motion of the individual water particles, and potential energy results from the displacement of the water surface relative to the still water level as the wave passes. Equations for the average potential, kinetic and total energy for a waveform are given below.

$$PE = \frac{\rho g H^2}{16}$$

$$KE = \frac{\rho g H^2}{16} \tag{2.9}$$

$$E = \frac{\rho g H^2}{8}$$

where PE = average potential energy per unit area $[m/t^2]$

KE = average kinetic energy per unit area $[m/t^2]$

E = average total energy per unit area $[m/t^2]$

ρ = density of water $[m/L^3]$

g = gravitational constant $[L/t^2]$

H = wave height as measured from crest to trough $[L]$

The equation for total energy per unit width along a wave crest is given below.

$$E_w = \frac{\rho g H^2 L}{8}$$ (2.10)

where E_w = total energy per unit width [mL/t²]

L = wave length [L]

For the Airy theory energy flux, the rate at which energy is transferred, can be expressed as in Equation 2.11.

$$\mathscr{F} = E_w C n$$ (2.11)

where $\mathscr{F}$ = average energy flux [mL/t³]

E_w = total energy as given above [m/t²]

C = wave celerity of a single wave [L/t]

n = ratio relating the group speed to the celerity of a single wave,

equal to: $n = \frac{1}{2}\left[1 + \frac{2kd}{\sinh(2kd)}\right]$

where d = water depth measured from the still water

line [L]

k = wave number equal to 2π/L where L is the

wave length [1/L]

For shallow water n =1

For deep water n = ½

It is typically assumed that the wave energy between two wave rays, lines running

perpendicular to the wave crests, remains constant as the wave moves from deep to shallow water. From this assumption, we may write the following:

$$\mathscr{F}_1 = \mathscr{F}_2 \qquad\qquad (2.12)$$

Substituting in the equations for energy flux and energy per unit width along a wave crest, then rearranging, the ratio of wave heights between two points may be written as in Equation 2.13. The geometry of this is ilustrated in Figure 2.12.

$$\frac{H_2}{H_1} = \sqrt{\frac{C_{g1}}{C_{g2}}} \sqrt{\frac{b_1}{b_2}} \qquad\qquad (2.13)$$

where C_g = group velocity defined by $C \cdot n$ [L/t]

b = distance between wave rays [L]
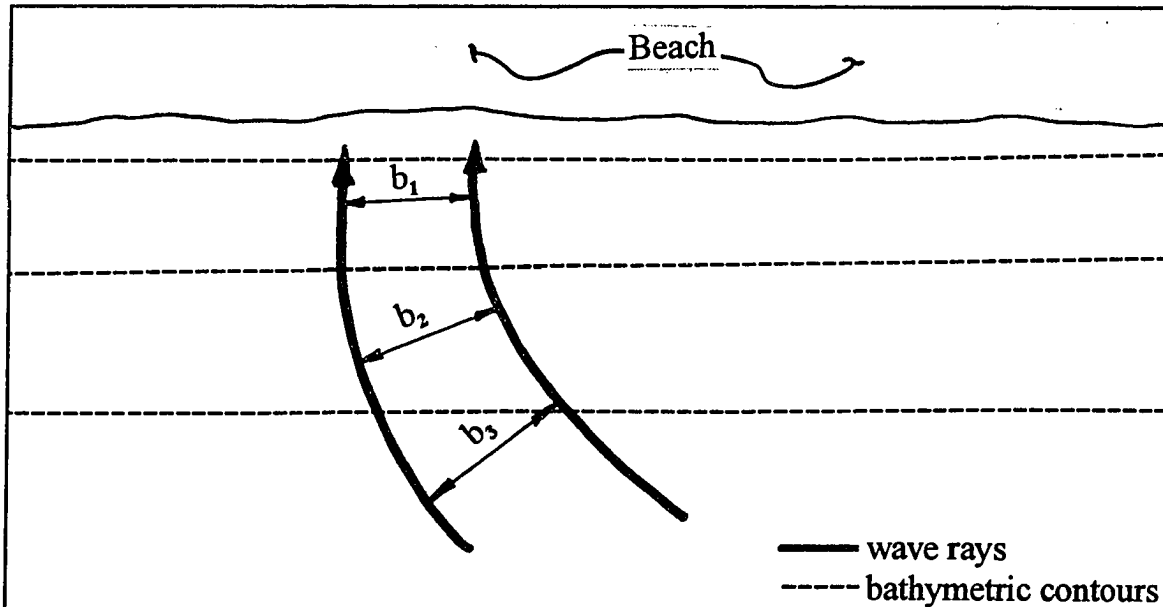
Figure 2.12. Energy flux between any two wave rays remains constant as the width, b, between the rays changes due to shoaling and refraction.

2.1.6 Hindcasting

Hindcasting is the use of past meteorological conditions to predict the wave climate. Ideally, a long record of wave and current information would be available from a nearby location. Based on these , the wave climate could be directly determined. However, along many coasts, lengthy historical wave records do not exist. It is therefore necessary to use a shorter wave record, if available, to hindcast a statistical estimation of the wave climate. Information from synoptic weather charts, wind data, and nautical charts or maps are combined to estimate the growth of waves based on wind induced shear stress across the ocean surface. Recorded wind data or data inferred from weather charts must be converted from their recorded elevation to the wind speed that would act directly on the ocean surface. Wind acting on the open ocean surface initially generates small capillary waves. However as the wind continues to blow, the waves grow. The distance over which the wind acts on the water surface is referred to as the fetch and is also considered in hindcasting. The fetch may be determined from maps or nautical charts.

Numerous analytical hindcasting methods exist of varying complexity. For engineering purposes simplified nomograms presented by CERC (1984) are usually adequate for wave climate estimation. However, along the Alaskan coast there are a general lack of wave and current information and validated hindcast models. In some areas this results in excessively conservative designs for many coastal facilities which increase cost considerably; yet in other areas coastal facilities may be underdesigned and may have a high risk of performance failure.

2.2 Remote Sensing

Sabins (1987) defines remote sensing as "collecting and interpreting information about a target without being in physical contact with the object." Because these observations may be made by sensors on aircraft and satellites, in many

instances, the observer need not be at the site area to perform the actual observation. Remote sensing has multiple applications in sparsely developed areas such as Alaska because it allows information to be gathered for areas whose accessibility is difficult at best.

2.2.1 Radar

Spaceborne radar remote sensing systems have the unique capability to record meaningful data through all weather conditions, night or day. The radar region of the electromagnetic spectrum spans between 0.1 and 30 cm in wavelength (Sabins 1987). Clouds are mostly transparent at these wavelengths, enabling radar systems to record data during all weather conditions. This feature is especially important for imaging ocean waves because the largest waves, which are of primary concern to coastal engineers, typically occur during storm events when skies are heavily clouded. The recent advent of several spaceborne SAR systems now allows data to be collected during windy or stormy weather when aircraft carrying airborne radar sensors may be grounded.

Active radar remote sensing systems transmit and record their own source of illumination. This is in contrast to passive systems, such as optical sensors which require the sun's energy to illuminate targets. Due to the active characteristic of radar remote sensing systems, they are capable of imaging both day and night, while passive optical systems are limited to daytime use.

Considering the daytime/nighttime and all-weather capabilities of spaceborne radar systems, it is prudent to explore their wave imaging capabilities.

2.2.1a Radar Terminology

Range and azimuthal distances, depression angle, ground footprints, and resolution are common terms used in the discussion of radar remote sensing. The

range and azimuthal directions, also known as the cross-track and along-track directions respectively, are used to describe the location of objects relative to the flight path of the sensor. These directions are shown as the horizontal axes in Figure 2.13. The depression angle is the angle between horizontal and the direction of the transmitted radar signal. This is also shown in Figure 2.13.

Radar signals are transmitted in short pulses which illuminate a small section of the earth's surface at an instant in time (ranging between 0.46 and 1.7 seconds for current spaceborne SAR sensors). This area is called the ground footprint, or simply the footprint, of the sensor and is illustrated in Figure 2.14. Resolution is the minimum separation distance required by the sensor to distinguish between two objects.
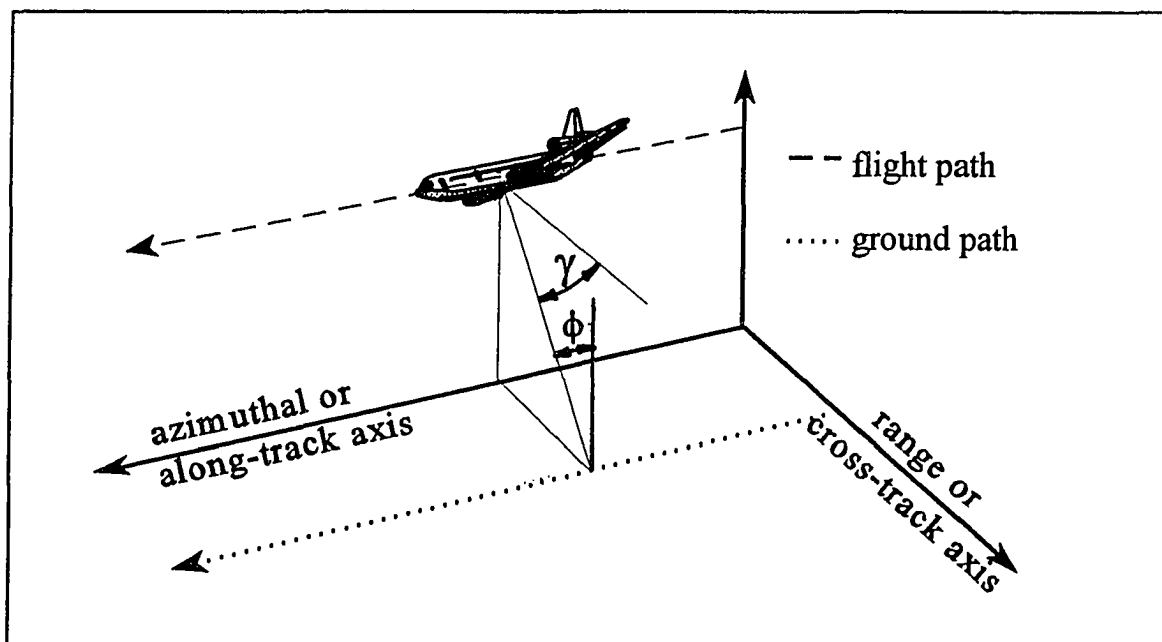
Figure 2.13. Radar imaging coordinate system. The azimuthal or along-track axis is parallel to the flight path of the radar sensor and the range or cross-track axis is perpendicular to the flight path. The depression angle is given by γ, and the incidence angle is denoted as φ.
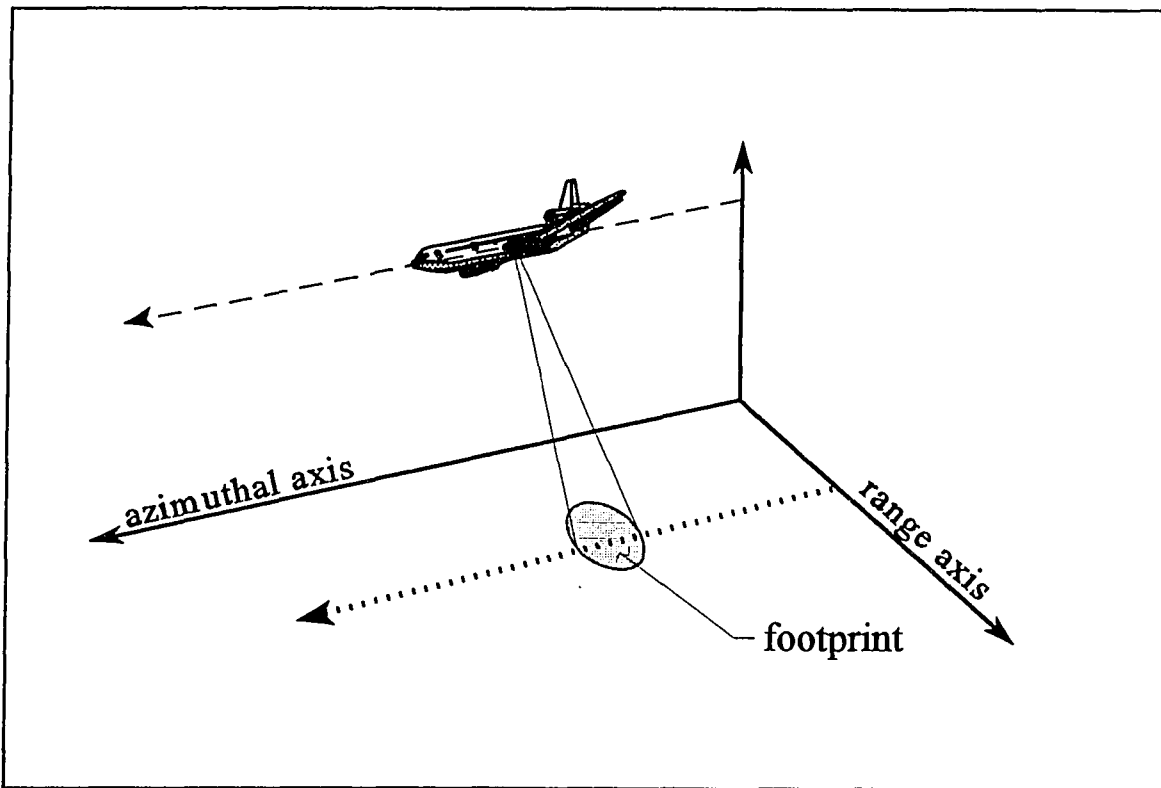
Figure 2.14. The sensor illuminates a given area, or footprint, on the earth's surface at any instant in time.

2.2.1b Range Resolution

Range resolution is the ability of the sensor to distinguish between objects in the range direction and may be determined through examination of the system's geometry. The illuminated surface causes the beam to reflect and scatter. The portion of the energy returned to the sensor is then recorded. Beams hitting the ground features closest to the sensor are reflected first, and thus returned first, while those farthest away are returned last, as illustrated in Figure 2.15.
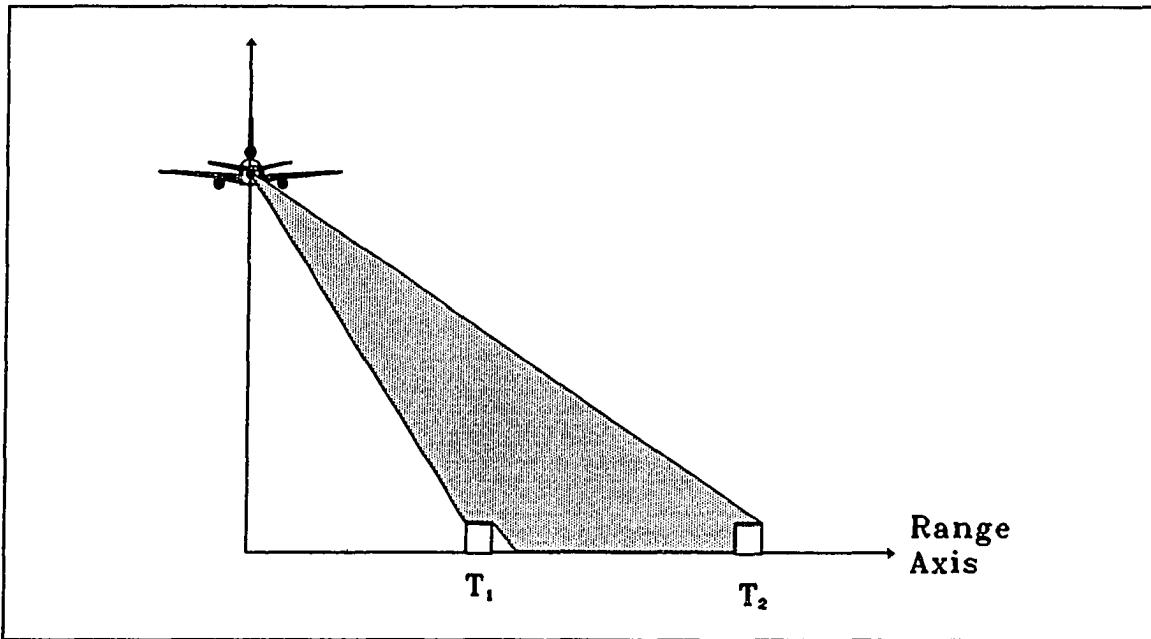
Figure 2.15. Because target T_1 is closer to the sensor than target T_2, the return signal from T_1 will reach the sensor before the return from T_2.

The location of an object in the range direction is determined by recording the time required for the radar pulse to be transmitted to and returned from the object. Combining this time with the velocity at which electromagnetic energy travels, the distance to the object can be calculated as given below (Reeves et al. 1975).

$$S = \frac{tc}{2}$$

(2.14)

where S = slant range distance to the object from the sensor [L]

t = time required for the signal to leave and return to the sensor [t]

c = propagation speed of electromagnetic radiation [L/t]

Range resolution of some radar systems is a function of the depression angle and the pulse length, or duration of the transmitted pulse, τ. If the system is to differentiate between consecutive pulses of length τ, the pulses must be separated by a time of 2τ to allow the pulse to travel to and return from the object. This concept is illustrated in Figure 2.16.
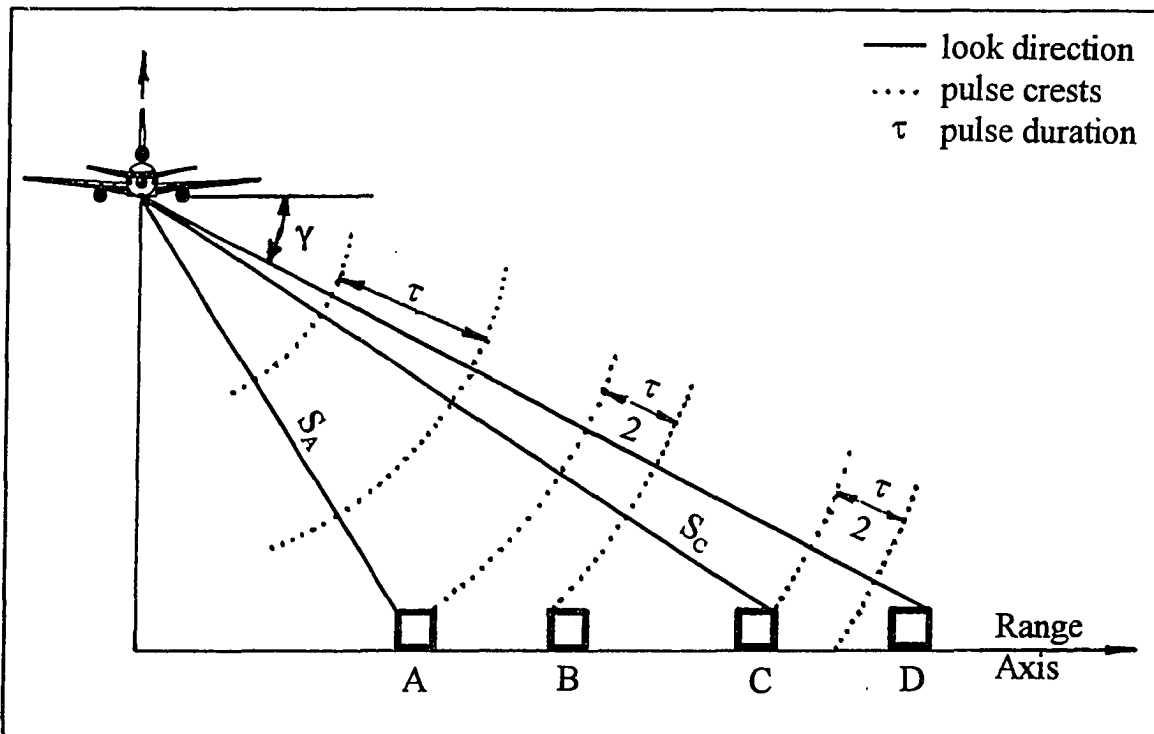
Figure 2.16. Because targets A and B are not separated by more than one half pulse length, τ, they are not resolved. However targets C and D are separated by a distance greater than $\tau/2$ and are therefore resolved in the range direction. S_A and S_C are the slant range distances to targets A and C, respectively (Sabins 1987).

Substituting twice the slant range resolution, $2R_{rs}$ for S and $t = 2\tau$ into Equation 2.14 and rearranging, the following may be written.

$$2\tau = \frac{2 \cdot 2 R_{rs}}{c}$$ (2.15)

where τ = duration of the transmitted pulse [t]

R_{rs} = slant range resolution measured along the direction of pulse

propagation [L]

c = propagation speed of electromagnetic radiation [L/t]

Rearranging this, the range resolution as measured along the slant distance from the sensor to the object may be written.

$$R_{rs} = \frac{\tau c}{2}$$ (2.16)

However, rather than slant range distance, the range resolution is typically described in terms of distance along the ground surface. This may be obtained by dividing the right hand side of Equation 2.16 by the cosine of the depression angle as shown below.

$$R_r = \frac{\tau c}{2\cos\gamma}$$ (2.17)

where R_r = range resolution as measured along the ground surface [L]

τ = duration of the transmitted pulse [t]

c = propagation speed of electromagnetic radiation [L/t]

γ = depression angle [deg]

The concept of range resolution is illustrated in Figure 2.17 (Sabins 1987).
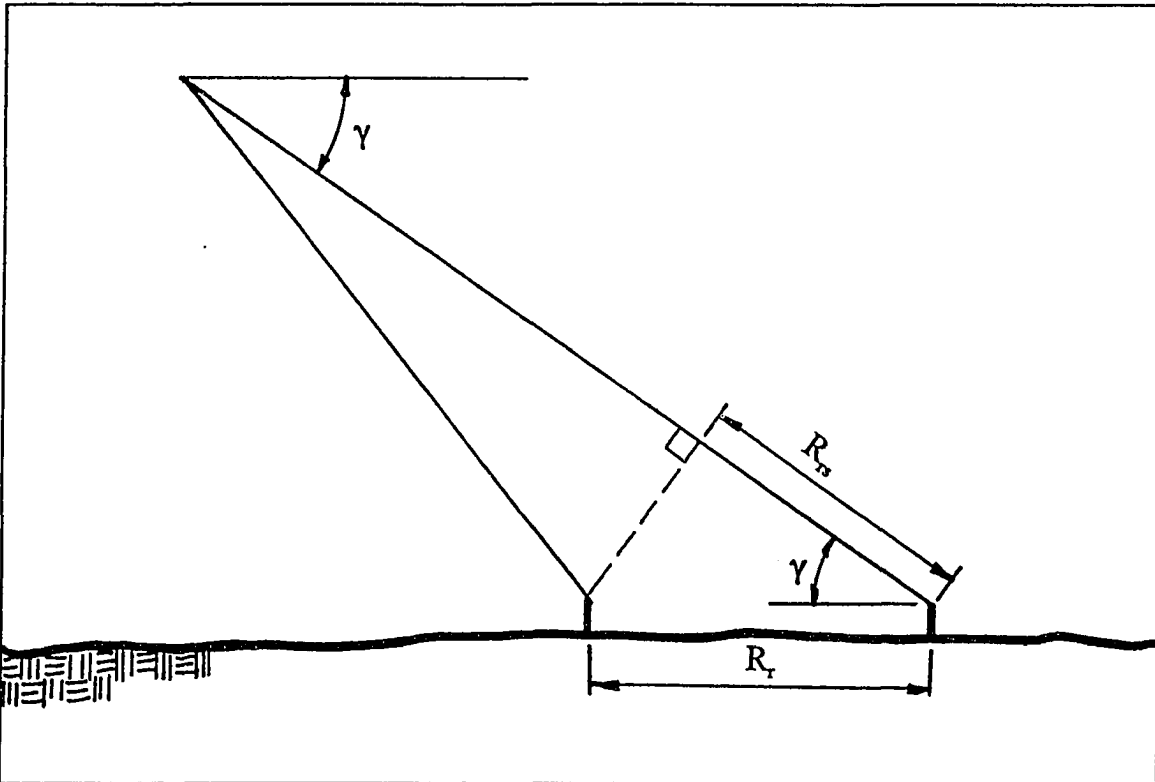
Figure 2.17. Ground range resolution, R_r, is computed by dividing the slant range resolution, R_{rs}, by the cosine of the depression angle, γ.

2.2.1c Azimuthal Resolution

Azimuthal resolution for a real aperture radar system is the minimum distance between separable points in the azimuthal direction and is equal to the width of the radar beam that illuminates the earth's surface. According to Sabins (1987) Equation 2.18 describes the azimuthal resolution.

$$R_a = \frac{0.7\lambda S}{D}$$

(2.18)

where R_a = azimuthal resolution [L]

λ= wavelength of the propagating pulse [L]

S = slant range or distance from the sensor [L]

D = antenna diameter [L]

The fact that the azimuthal resolution is proportional to the slant range distance indicates that the resolution within a given image will vary directly with the proximity of an object to the sensor. Equation 2.18 also illustrates that azimuthal resolution decreases as antenna diameter increases, thereby implying large antennas are desirable in terms of resolution. Although this is true, large antennas become cumbersome when mounted on aircraft and spacecraft. For this reason synthetic aperture radar (SAR) was developed (Sabins 1987).

2.2.2 Synthetic Aperture Radar

SAR is a side-looking microwave imaging system from which a radar beam is transmitted in the range direction, perpendicular to the flight direction of the carrying vehicle. SAR systems use relatively small antennas which produce wide beams, and depend on the spatially induced phase modulation of the returned signal to obtain high resolution. Because the beams are wide, a given object enters the field of view before the sensor comes abreast of it and remains in the view after the sensor has passed. This is illustrated in Figure 2.18.
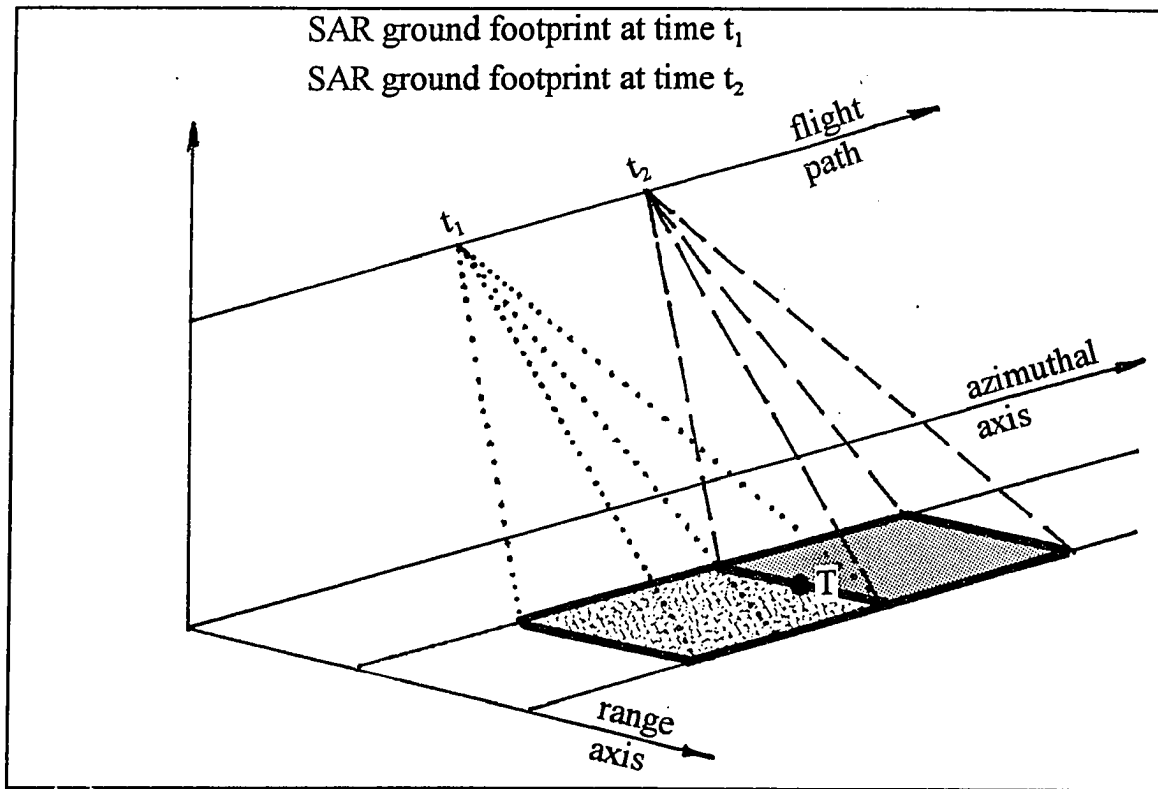
Figure 2.18. SAR sensor images a given target, T, at time t_1 before the sensor comes abreast of it, and continues to observe T until t_2, when the sensor passes beyond the target.

The coherent integration time is the length of time for which a given target remains in the field of view of the radar sensor. During the time a given object is in view, the sensor repeatedly measures the modulated phase of the returned signal from which the range distance to the object is inferred. When the object first comes into view, it has a relatively long range, however as the sensor approaches the object the range decreases. When the sensor is abreast of the object the range is at a minimum, and as the sensor recedes, the range again increases. These varying range values, if plotted, form a convex arc directed away from the sensor as illustrated in Figure 2.19. The values are then processed to reduce the arc to a single point, indicating the sensor

is abreast of the object. The azimuthal resolution of a SAR system is proportional to the antenna length. Therefore, unlike real aperture radar systems, smaller antennas on SAR systems increase resolution (PCI 1993).
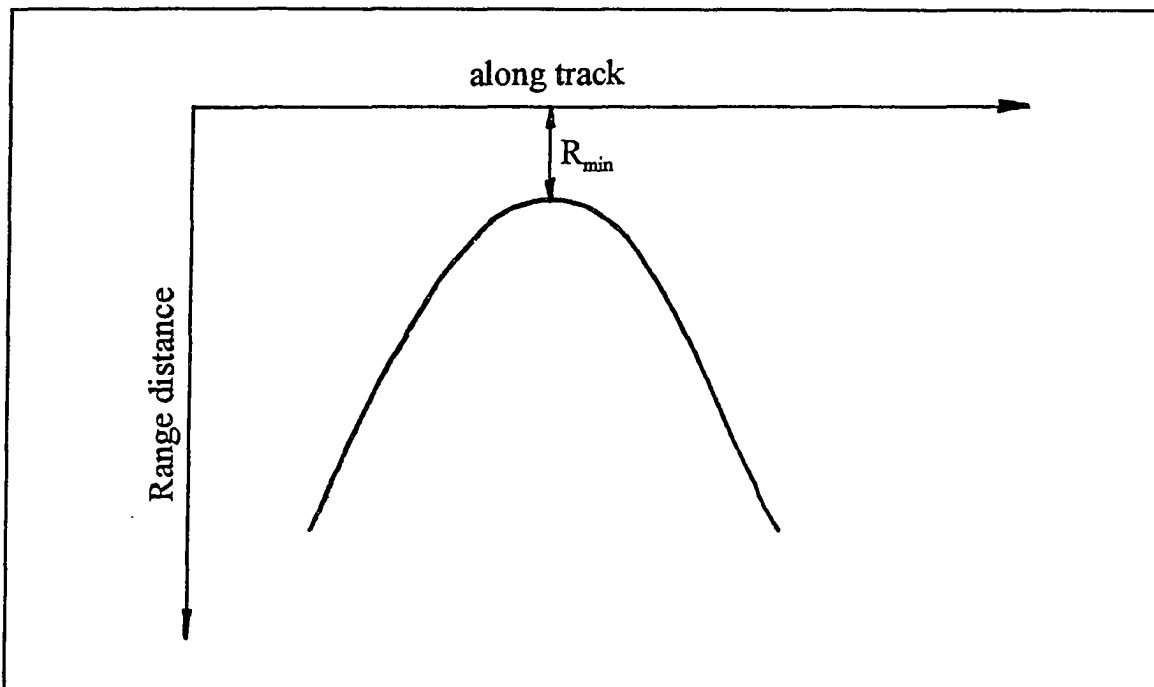
Figure 2.19. Plot of range distance as recorded along the satellite flight path. R_{min} is the minimum range distance from the sensor to the target.

2.2.2a Effect of Incidence Angle

The incidence angle, formed between the transmitted radar beam and a line perpendicular to the illuminated surface, as illustrated in Figure 2.20, greatly affects the brightness of the picture element, or pixel, on the resulting image.
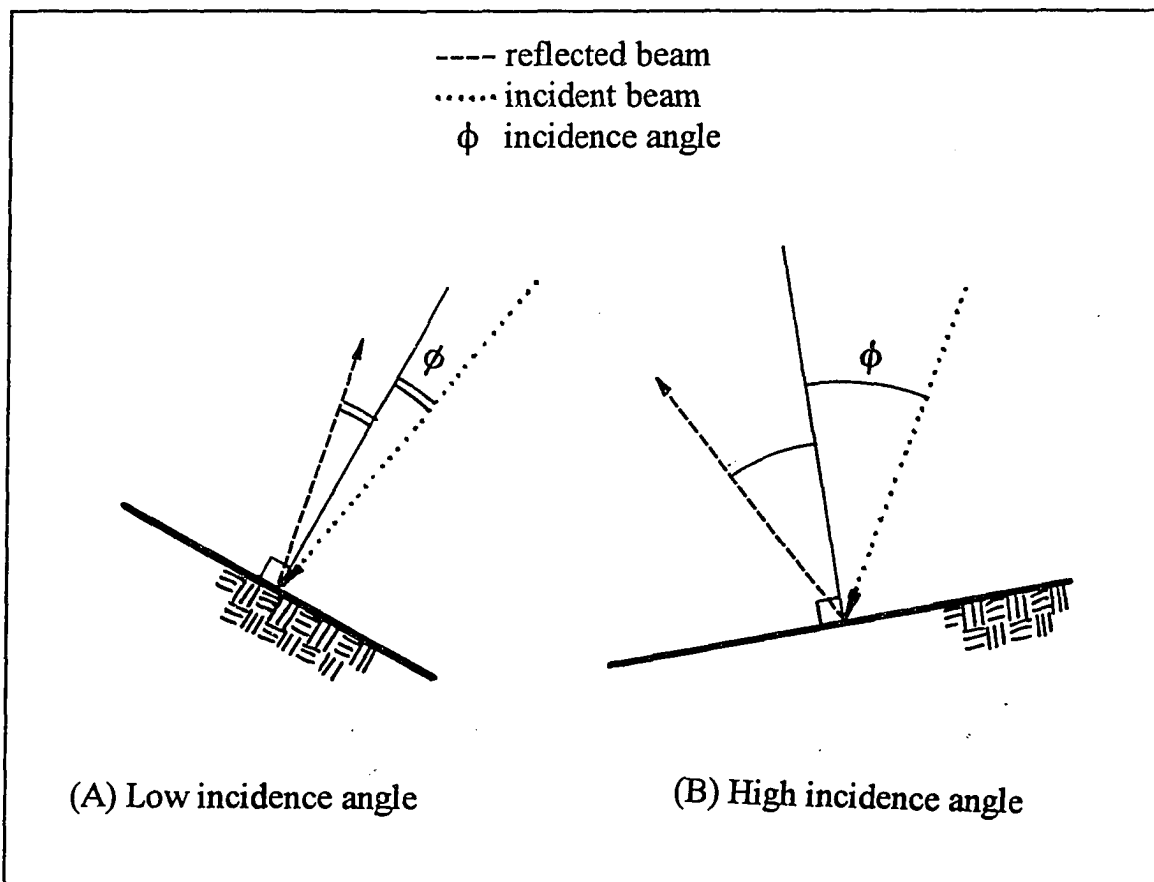
Figure 2.20. Effect of incidence angle on SAR signature. (A) If the incidence angle is small, much of the transmitted beam will be reflected back toward the sensor yielding a bright signature. (B) A large incidence angle will reflect the transmitted beam away from the sensor, creating a dark signature.

If the incidence angle is small, much of the transmitted radar beam will be reflected back to the sensor, resulting in a relatively bright signature, or marking on the image. On the other hand, if the incidence angle is large, the surface will direct the transmitted beam away from the sensor, and cause a dark pixel. This is useful in the detection of long waves which change the slope of the water surface as shown in Figure 2.21.

© European Space Agency 1993
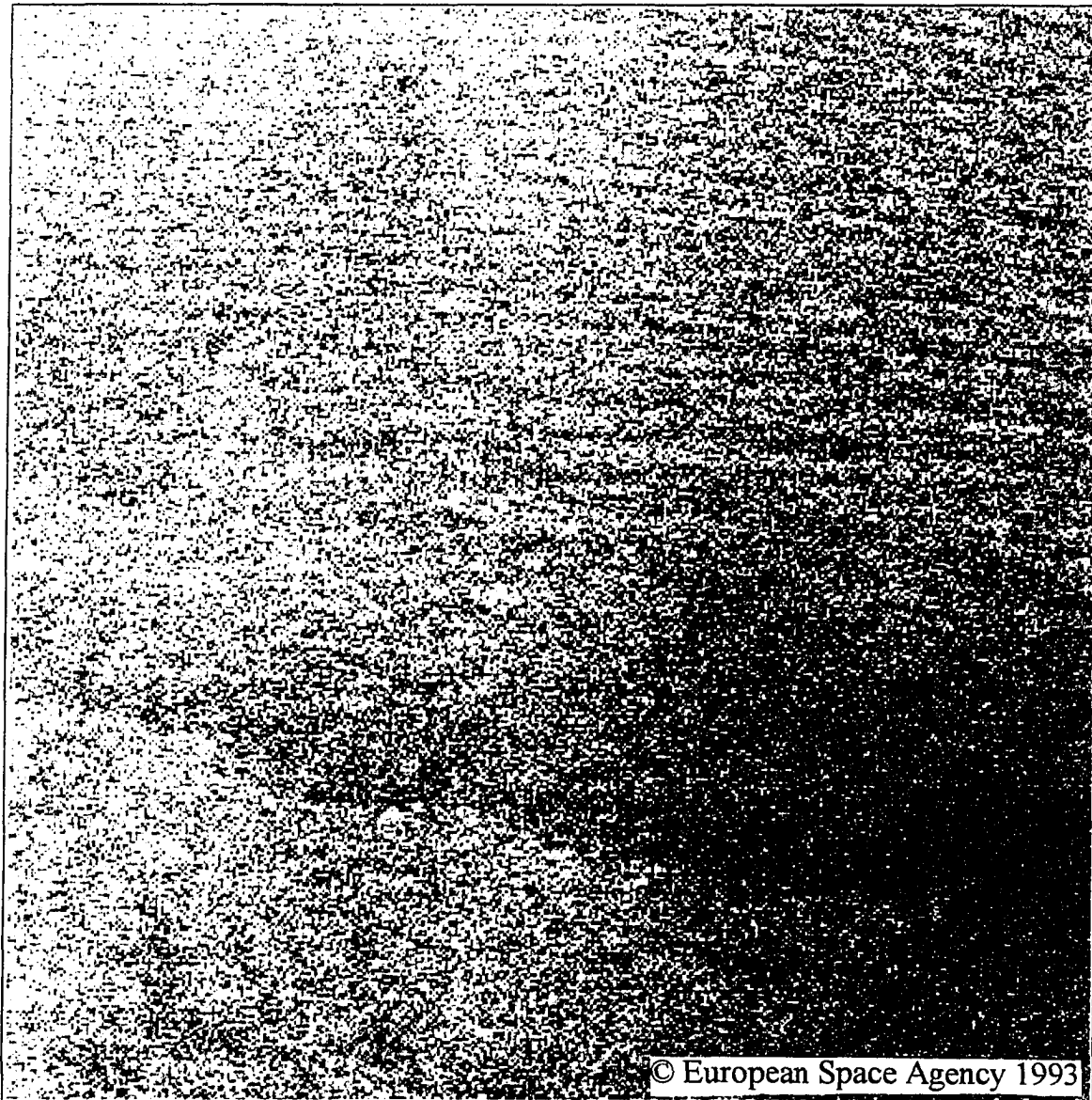
Figure 2.21. The variation of the water surface slope due to the passage of waves is evidenced on SAR imagery as alternating bright and dark bands.

2.2.2b Effect of Terrain Roughness

Roughness describes the surface of the terrain relative to the wavelength of the incoming radar signal. If a surface is smooth, such as a calm body of water, nearly all of the energy in the transmitted beam will be reflected from the surface as if it

were a mirror. This type of reflection is referred to as specular, and results in a dark signature because the energy is reflected away from the sensor. This is illustrated in Figure 2.22.

---reflected beam
····incident beam
ϕ incidence angle
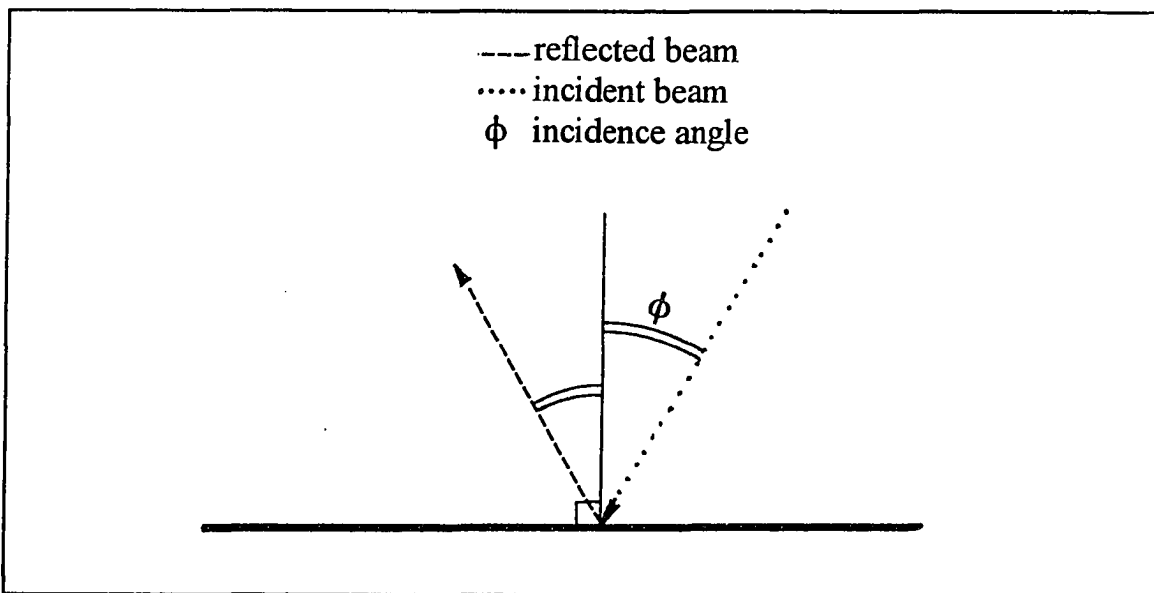
Figure 2.22. Radar signal reflected off a smooth or specular object resulting in a dark signature.

If a breeze occurs over the body of water described previously, small, or capillary, waves develop. The height of capillary waves is on the order of centimeters, the same order of magnitude as the wavelength of the transmitted radar beam. When the beam hits the surface, a portion of the beam will still be reflected; however, a significant portion will be scattered. As with a specular surface, the reflected portion of the wave will not return to the sensor, but a portion of the scattered energy will. This will cause a brighter signature than the flat, reflective surface and is illustrated in Figure 2.23 (PCI 1993). This type of interaction between the surface and the signal is termed Bragg scattering and merits particular attention when investigating ocean waves with SAR. During wind storms capillary waves are

superimposed on the large waves. The effect of Bragg scattering on these capillary waves results in a very bright signature which dominates the image and masks the large underlying waves (PCI 1993).
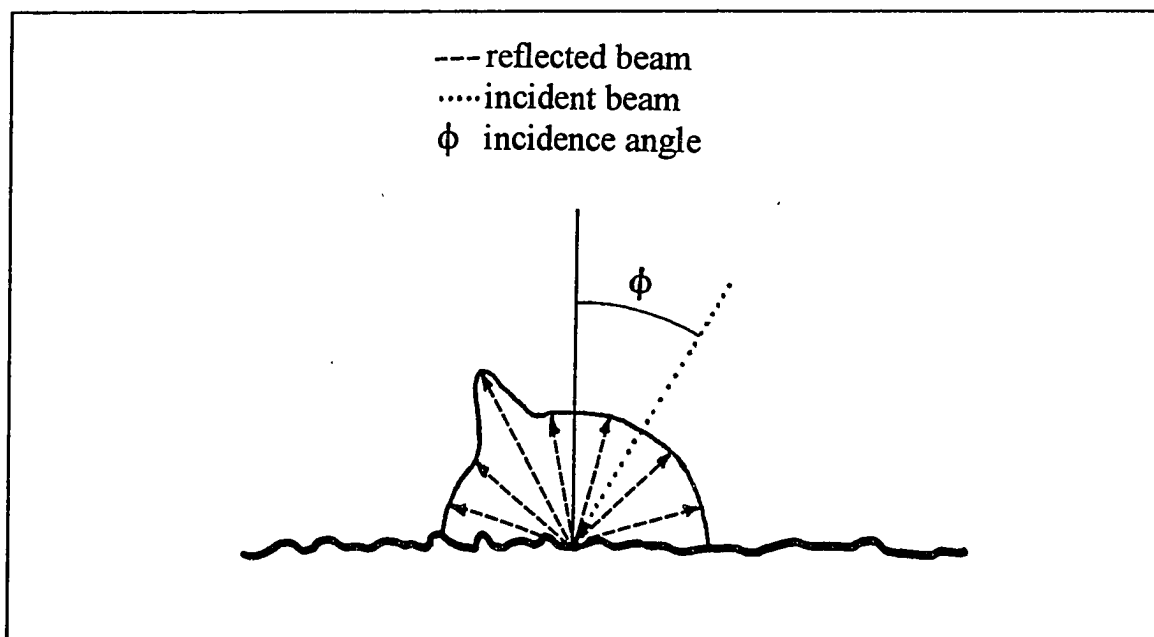
Figure 2.23. The radar signal is partially scattered and partially reflected off a relatively rough surface. The result is a relatively bright signature on the image.

Signal return to the sensor is maximized by a corner reflector which can return most of the transmitted radar energy to the sensor. This results in very bright pixels on the SAR image. Corner reflectors are usually man-made objects consisting of two or three mutually perpendicular planes which reorient the incident beam directly back to the sensor. A three plane corner reflector will return the signal from a larger number of incoming directions than will a two plane corner reflector. Therefore, three plane corner reflectors are typically constructed for the purpose of locating a ground point on the resulting image. However, two plane corner reflectors, built for

other purposes, are much more common; a typical example is the side of a building intersecting a sidewalk or road as illustrated in Figure 2.24 (Reeves et al. 1975).
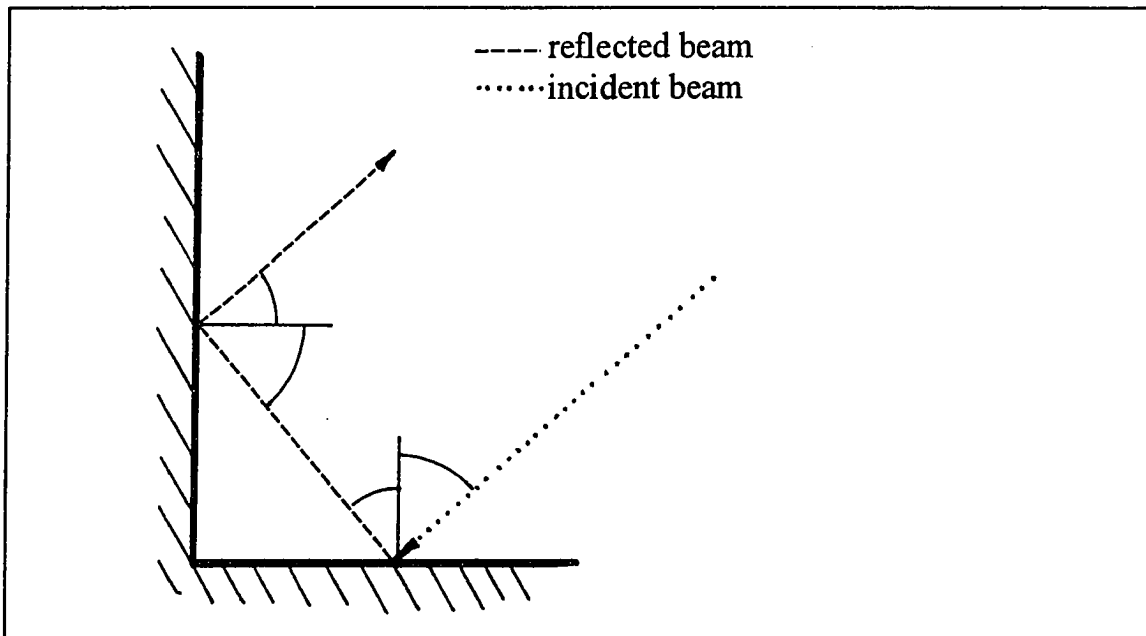
Figure 2.24. A two plane corner reflector returns nearly one hundred percent of the incident radar signal to the sensor, causing a very bright signature.

2.2.2c Effect of Complex Dielectric Properties

The complex dielectric property of an object is a function of its pure dielectric characteristics and its conductive properties. The capacitance of a capacitor is increased when a dielectric material is placed between its plates. The factor by which the capacitance is increased is the dielectric constant of the material. Water has an extremely high dielectric constant in comparison to other materials as shown in Table 2.1 (Serway 1990).

Material	Dielectric Constant
Air	1.00059
Neoprene rubber	6.7
Paper	3.7
Teflon	2.1
Vacuum	1.00000
Water	80.0

Table 2.1. Dielectric constant of water is much larger than that of other common materials (Serway 1990).

As the dielectric constant increases, radar return increases, thus resulting in a brighter signature. Because water has one of the highest dielectric constants in nature, moist soil or lush vegetation will appear brighter than dry soil or vegetation. Although water has a high dielectric coefficient which tends to elicit a bright signature, standing water has a specular surface which will cause the incident radar to be reflected rather than return to the sensor, thus causing the dark signature of standing water (Sabins 1987).

2.2.2d Layover

Image layover is the most obvious difference between radar and optical images. If a mountain were observed by an optical sensor, such as a camera, looking down at an angle, the top of the mountain would appear farther away from the base. A map, on the other hand, shows the true relative position of the mountain-- directly over its base. On a radar image the mountain top may appear closer than its base. This apparent "tipping over," or "layover", is illustrated in Figure 2.25.

© European Space Agency 1992
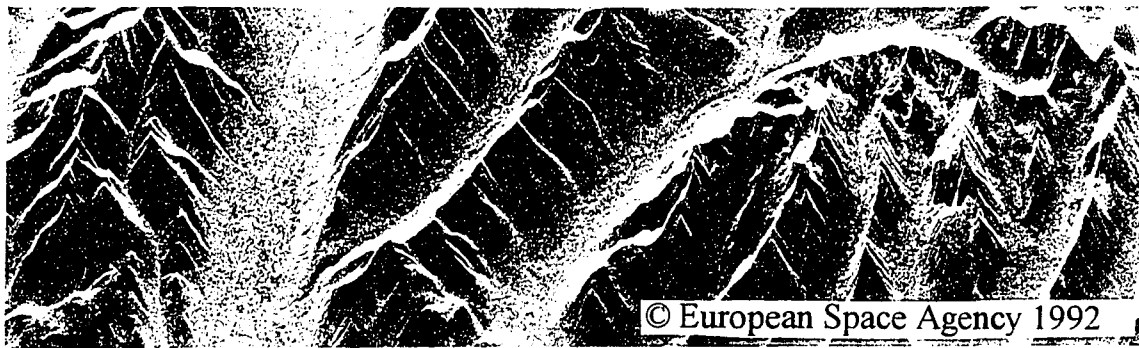
A. Radar image exemplifying layover, the appearance that mountain peaks are closer than the bases.

B. Landsat optical image illustrating mountain peaks that appear farther away than do the bases.
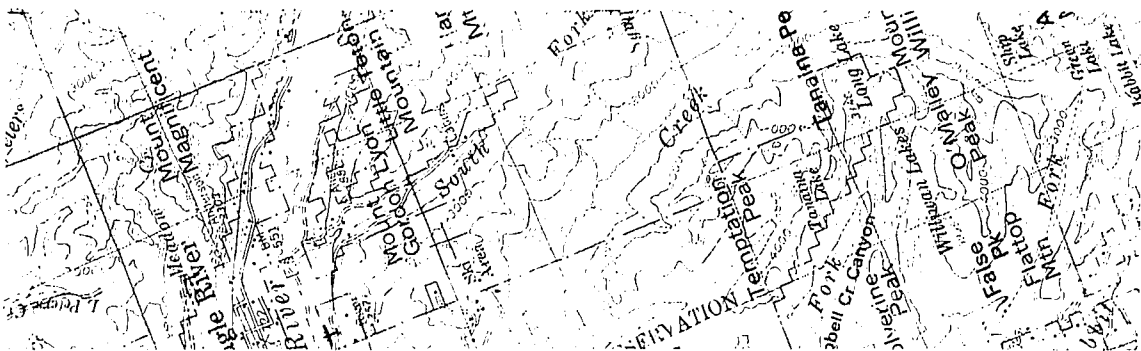
C. Contour map illustrating the true relationship of mountain peaks relative to their bases.

Figure 2.25. Comparison of radar image, optical image, and topographical map showing the effects of layover.

A radar system transmits pulses radially outward, and records the time required for the pulse to be transmitted and returned. Layover results when, due to the curvature of the transmitted radar pulse, the pulse reaches and returns from the mountain top before it does from the base. The resulting image shows the mountain top nearer the sensor than the mountain base. This is illustrated in Figure 2.26 with points A, B, and C. Since point A is closest to the sensor, the radar pulse striking it will return to the sensor first. The signal from point B will return next, and finally, the information from point C will register. Therefore, point C will appear farther from the center of the image than will point A. This is contrary to the image resulting from an optical sensor.
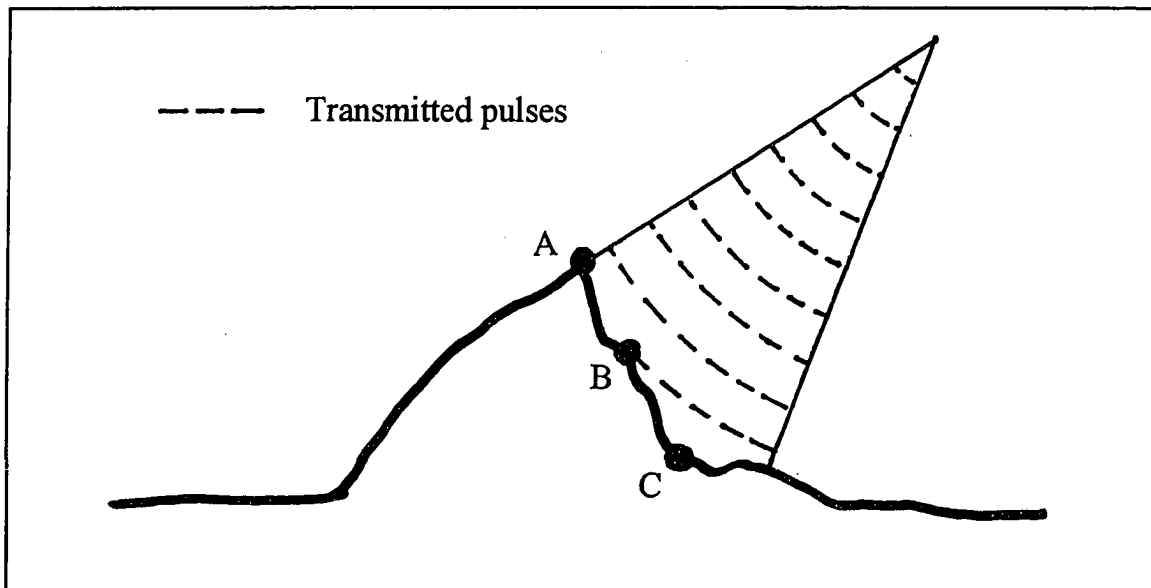
Figure 2.26. Layover results when point A is detected before point B, and point B prior to point C. The resulting imaged target appears to lean toward the sensor.

Layover depends on the height of the object, the slope of its surface, and the depression angle. The taller the object, the earlier its top will be detected, and more layover will occur. If the slope of the object is relatively flat, it is likely that a given

radar pulse will reach the base of the object prior to intercepting its top. This tends to reduce the amount of layover. As the depression angle of the radar sensor system is increased, layover becomes more prominent as illustrated in Figure 2.27. Although layover does not significantly affect observation of waves due to their relatively small height , this example illustrates one of the distortions resulting from SAR imaging of surfaces. When evaluating SAR images it is tempting to evaluate the image as if it were an optical photograph. It is vitally important to continually keep in mind the difference between SAR and optical images.
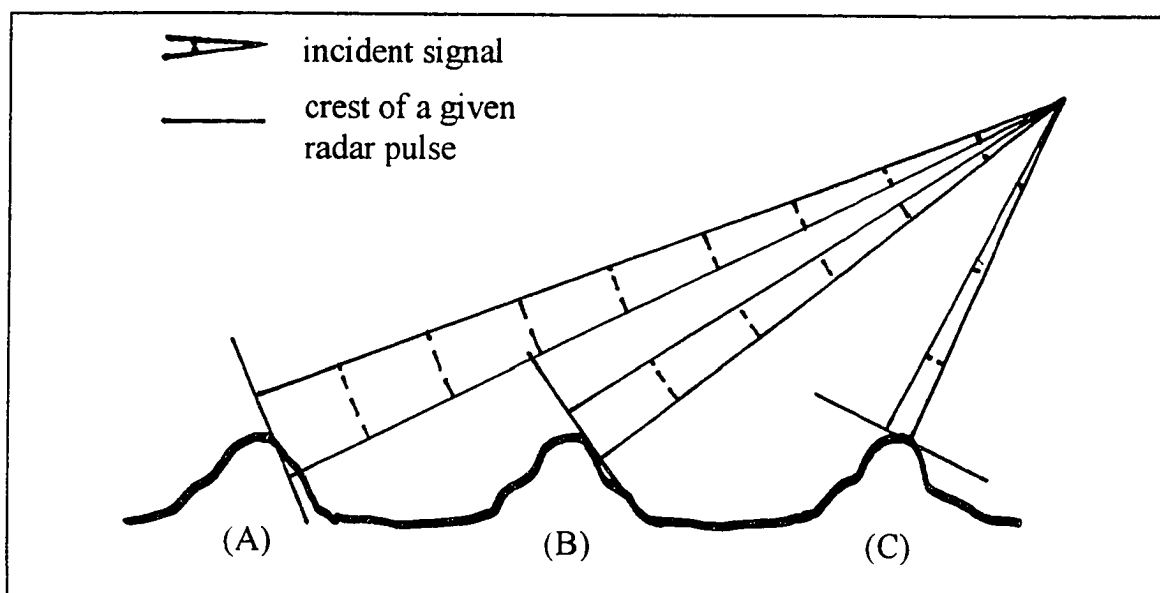
Figure 2.27. Layover increases as the depression angle increases. In (A) no layover will occur. The entire face of the mountain in (B) will appear to be equidistant from the radar sensor. The mountain in (C) will appear to layover.

2.2.2e Shadowing

Radar shadowing is similar to the familiar shadowing of the sun's illumination. Much like the sun, a radar sensor provides its own source of illumination. When it is noon and the sun is directly overhead, few shadows are present. Similarly, if the

depression angle of the radar sensor were 90°, there would seldom be radar shadows because all sides of all objects would be illuminated. As evening approaches, the sun drops lower in the sky and shadows form. Similarly, as the depression angle of a radar sensor decreases, radar shadows form. This is the result of objects in the foreground blocking illumination of objects in the background. As the sun drops lower and lower, the length of the shadows continues to increase. Likewise, as the depression angle of the radar sensor decreases, the length of the radar shadow increases. Because no illumination reaches the shadowed area, no information is collected from the region. This is illustrated in Figure 2.28. As the radar sensor depression angle decreases, radar shadowing increases while layover decreases. Therefore radar sensor designers must balance the effect of layover and shadowing when specifying the depression angle of a system (Sabins 1987).
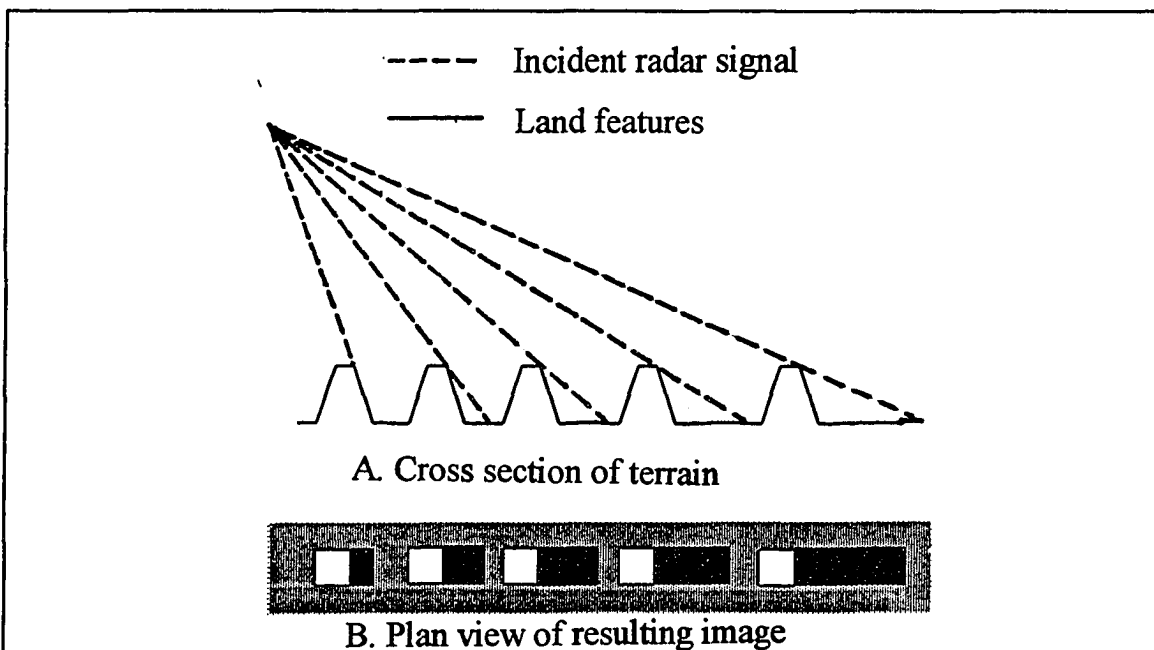
Figure 2.28. Because tall objects block regions from illumination, the image contains no data from the shadowed areas.

2.2.2f Speckle

The term speckle is used to describe the characteristic salt and pepper appearance of radar images. This random reflected energy, called noise, results from the variety of information contained in the ground cell, or surface area represented by a single pixel on the image. If reflectors are exactly the same distance from the sensor, they may return radar signals which positively reinforce each other just as water waves reinforce each other. This would result in a brighter signature for that particular ground cell. However, individual reflectors within a ground cell may also return signals which cause destructive interference. This would make the resulting pixel unusually dark. The combination of unusually bright and dark pixels in one image results in a mottled appearance, as illustrated in Figure 2.29. Averaging several pixel intensity values together tends to reduce speckle by smoothing. However, the averaging of pixels replaces the original pixels with larger pixels and thereby reduces resolution.

© European Space Agency 1993

Figure 2.29. SAR imagery tends to exhibit a characteristic salt and pepper look called speckle.

2.2.2g System Parameters of Spaceborne SAR Sensors

Three spaceborne SAR sensors are currently active: ERS-1, ERS-2, and JERS-1. ERS-1 and -2 are the First and Second Earth Resource Satellites launched in 1991 and 1995, respectively, by the European Space Agency (ESA). JERS-1, launched in 1992, is owned by the National Space Development Agency of Japan. The Canadian Center for Remote Sensing is planning to launch Radarsat in September, 1995. Basic parameters for each system, including swath width, wavelength, and polarization, are summarized in Table 2.2.

The swath width refers to the width of the ground illuminated by the system as the satellite orbits, and correlates to the width of the resulting image. Note that Radarsat is capable of imaging a variety of swath widths which results in different resolutions. Differences between the sensors' transmitted energy wavelengths influence which objects are detected by the system. The shorter wavelength sensors are typically used for the imaging of the ocean surface. The uses of various electromagnetic wavelengths is summarized in Table 2.3. Polarization describes the orientation of the oscillation of the transmitted and returned radar signals. V means vertically oscillating, and H means horizontally oscillating signals. The first letter refers to the orientation of the transmitted pulse, while the second letter describes the return signal. This is illustrated in Figure 2.30. Like the wavelength, the orientation of the signals affect the applications for which the sensor is useful. The dependence of polarization on backscatter from the water surface is difficult to quantify, however, it is estimated that surface roughness plays a greater role than polarization orientation in backscatter return (Reeves et al. 1975).

Parameter	Mission		
	ERS-1 & -2	**JERS-1**	**Radarsat**
Altitude (km)	785	568	798
Repeat cycle (days)	3, 35, 176	41	24
Orbit type	sun synchronous	sun synchronous	sun synchronous
Ground track velocity (km/s)	6.628	6.883	6.576
Frequency (GHz)	C-band (5.3)	L-band (1.275)	C-band (5.3)
Wavelength (cm)	5.66	23.5	5.66
Polarization	VV	HH	HH
Swath width (km)	100	75	50 - 500
Minimum pixel size (m)	12.5 x 12.5	7 x 7	10 x 10
Resolution (m) @ # of looks	30 @ 4	30 @ 4	30 @ 4
Depression angle	right 20.355°	right 35.21°	right 20°-50°
Incidence angle range, Mid-incidence angle	19.35°-26.50° 23°	36.14°-41.51° 38.91°	22.64°-59.56° 45.12°
Lifetime (years)	2-3+	2+	5
Footprint (km) (rng x azm)	80 x 4.8	70 x 14	50-150 x 4.3
Coherent integration time (s)	0.6	1.7	0.46

Table 2.2. System parameters of SAR sensors (Olmsted 1993).

Wavelength (cm)	Application
21.40	Surface soil moisture
6.97	Sea surface temperature
5.77	Sea surface temperature
4.55	Sea surface temperature
2.89	Sea surface temperature
2.80	Surface wind field
2.16	Surface roughness
1.55	Surface features
1.43	Atmospheric water content
1.35	Atmospheric water content
0.96	Surface imaging
0.86	Surface imaging
0.81	Surface ice, oil
0.33	Surface imaging
0.22	Surface imaging
0.17	Atmospheric water content

Table 2.3. Applications of various radar wavelengths.
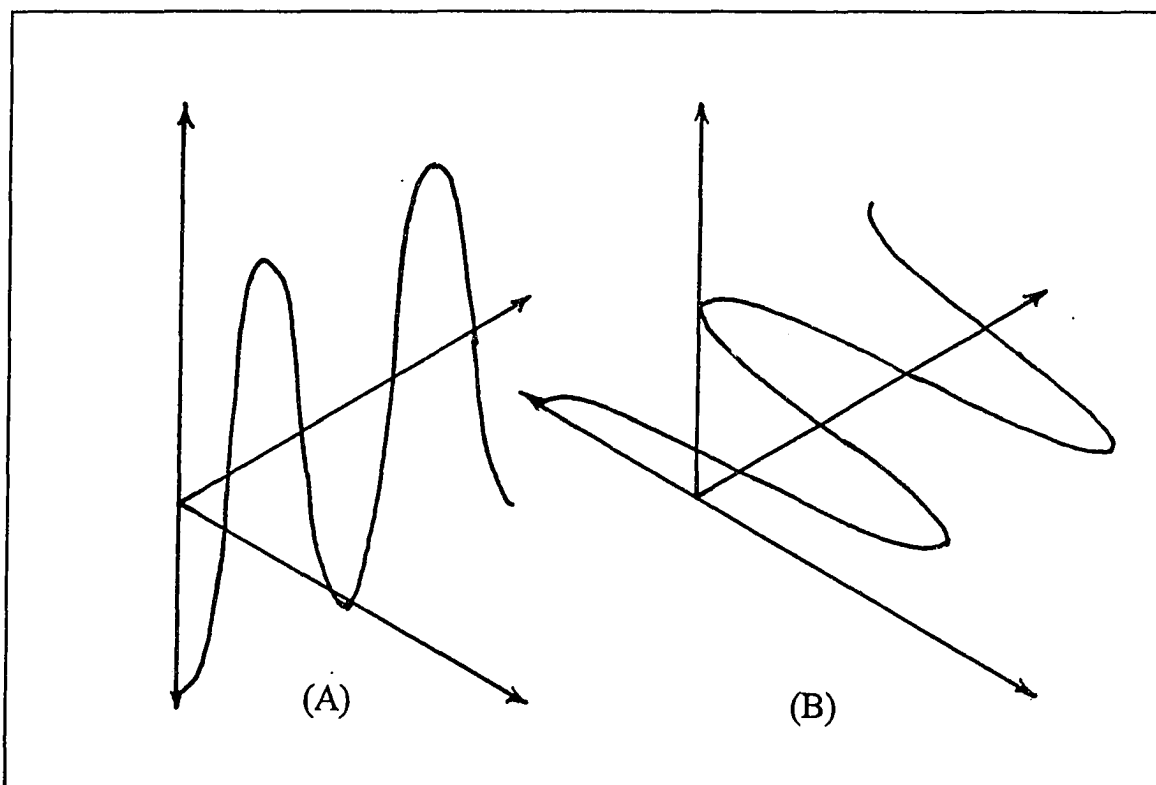
Figure 2.30. Oscillation planes of (A) vertically, and (B) horizontally polarized signals.

2.2.3 Radar Altimetry

Satellite altimetry systems combine radar altimetry with a precise orbit to determine the elevation of the imaged surface. Radar altimetry operates on the same principles as SAR, but is nadir-viewing rather than side-looking as illustrated in Figure 2.31. Short radar pulses are transmitted, reflected from the imaged surface, and returned to the sensor to determine the precise altitude of the satellite above the surface. Because the satellite's orbit around the center of the earth is maintained with high precision, the difference between the orbit altitude and the imaged surface is the elevation of the imaged surface relative to the center of the earth (TOPEX/POSEIDON Science Working Team 1991).
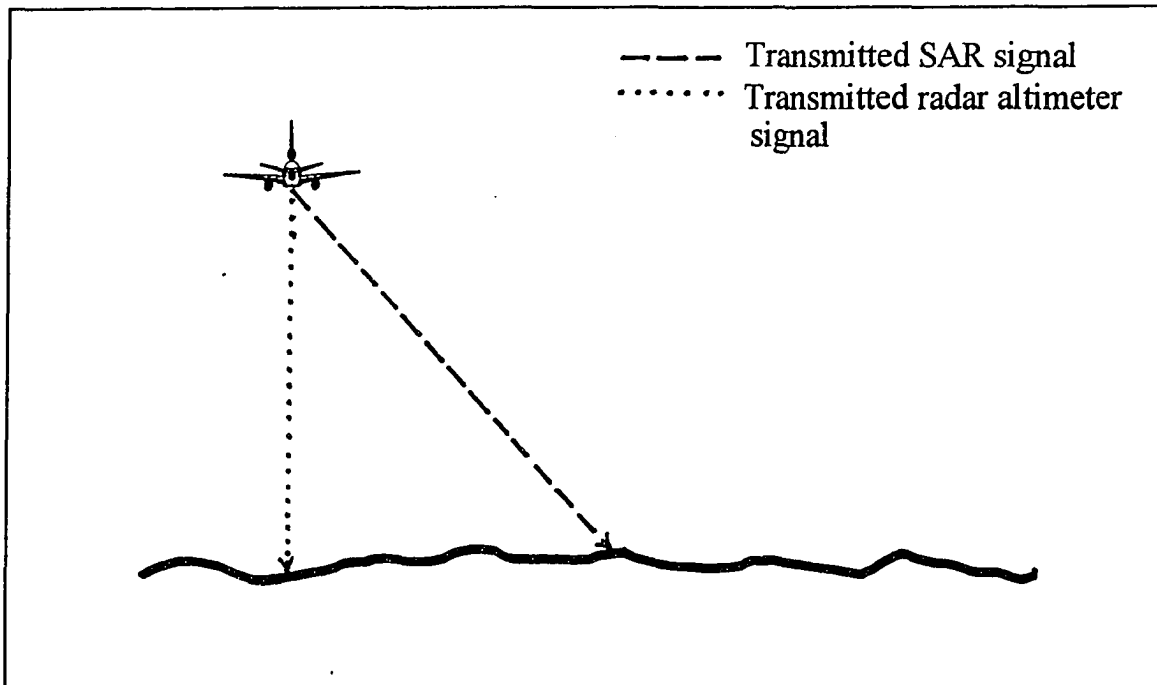
Figure 2.31. Radar altimeters are nadir-viewing as compared to side-looking SAR systems.

The primary advantage of SAR over radar altimetry is its coverage. SAR provides full coverage of the earth's surface, while radar altimeters cover only approximately one tenth of the surface. For example, TOPEX / POSEIDON, a satellite carrying a radar altimeter, images a grid with swaths 2 kilometer wide separated by approximately 200 kilometers as shown Figure 2.32 (TOPEX / POSEIDON). The gridded nature of altimeter data limits its usefulness as a basis for coastal engineering design because it is not available for all locations. On the other hand, the full coverage provided by SAR will enable its data to be used at any coastal engineering project site. Additionally, the current SAR sensors have 30 meter resolution while the resolution of radar altimeters is on the order of 1 kilometer. Radar altimeter systems average ocean wave heights over a 2 by 6 kilometer area (Fu 1993), and this further limits its usefulness for site specific wave parameters.
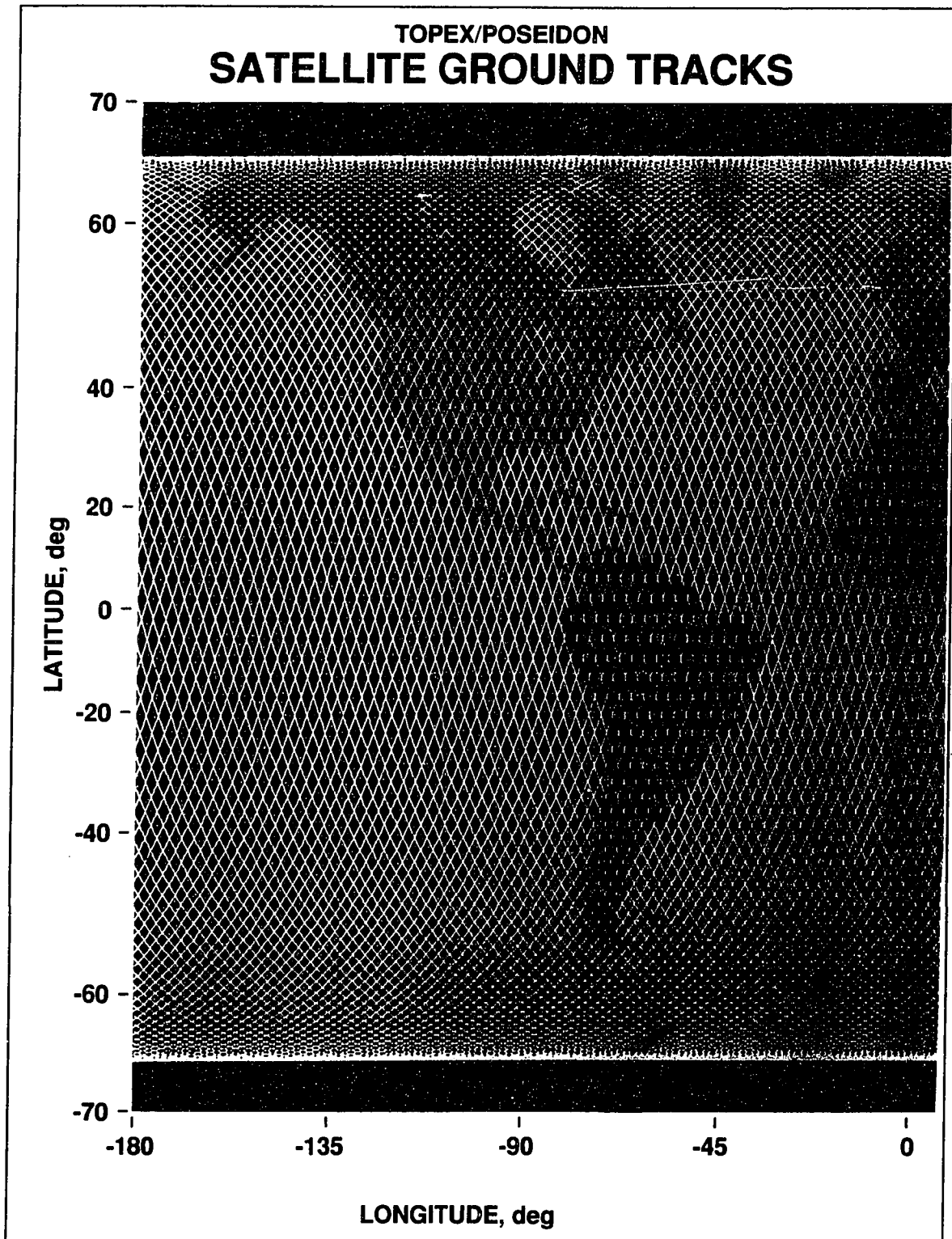
Figure 2.32. The nadir-viewing TOPEX/POSEIDON radar altimeter images along a grid with 2 kilometer wide swaths approximately 200 kilometers apart.

2.3 Use of SAR to Examine Waves

The qualitative evaluation of SAR's ability to image ocean waves began with the launching of the first SAR satellite, Seasat, in 1978. Since that time several SAR satellites have been launched, allowing more quantitative analyses. Some factors which limit the use of SAR in the detection of ocean waves have been determined, and methods to enhance the data collected from SAR for detection of ocean waves have been developed.

2.3.1 Seasat

The potential of SAR to record two dimensional wave fields was demonstrated during the short-lived, Seasat mission. The Seasat satellite carried, among other sensors, a SAR, and was operational for only 100 days. Despite its prematurely aborted mission, Seasat demonstrated the many uses of SAR for imaging the ocean surface. Possible oceanographic uses of SAR included detection of surface and internal waves. Although maximum radar penetration into water is only on the order of millimeters, bathymetric features could be detected through their manifestations on the ocean surface.

2.3.2 Limiting Factors

Since the Seasat mission, the theory of SAR imaging of ocean waves has been researched and an understanding of some of the fundamental mechanisms involved has been obtained. SAR detects wave forms primarily by three mechanisms: tilt, hydrodynamic interactions, and Doppler shifting. Tilt refers to the change in incidence angle as the water surface changes due to the passage of long waves. The hydrodynamic interactions of long waves and short waves alter the wave energy and wavelength of short waves. This alteration is detectable by SAR. Doppler shift is

a result of the motion of the waves relative to the satellite, and occurs primarily in the azimuthal direction. Because a SAR image provides a still picture of a moving surface, the axis along which the wave travels can be determined, however the direction on the axis is indeterminate by 180^0. Due to this uncertainty, routine extraction of ocean wave spectra from SAR data has not been feasible (Hasselmann and Hasselmann 1991).

Significant discrepancies exist between the SAR derived and the actual ocean wave spectra due to velocity bunching, acceleration smear, and layover (Hasselmann and Hasselmann 1991).

Velocity bunching causes the SAR intensity profile to deviate from the actual ocean surface amplitude profile. The concept of velocity bunching is illustrated in Figure 2.33 where three different wave forms on the ocean surface are represented by the top heavy line. The left wave form is relatively flat, while the right form represents the steepest wave. Uniformly sampled backscatter returns are shown as thin sloping lines. The angles between the lines and vertical represent the azimuthal displacement of the picture elements on the image planes A, B, and C as the sensor moves further from the target. It can be seen on image plane A that the representation of the wave forms are a linear distortion of the original ocean surface. As the distance to the sensor increases, the imaged forms are alternately bunched and dispersed, indicating a nonlinear relationship between the resulting image and the true ocean surface. This nonlinearity is intensified as wave steepness increases. The nonlinear relationship can become so extreme that the modulation of the ocean surface is undetected in the image plane C (Hasselmann et. al 1985).
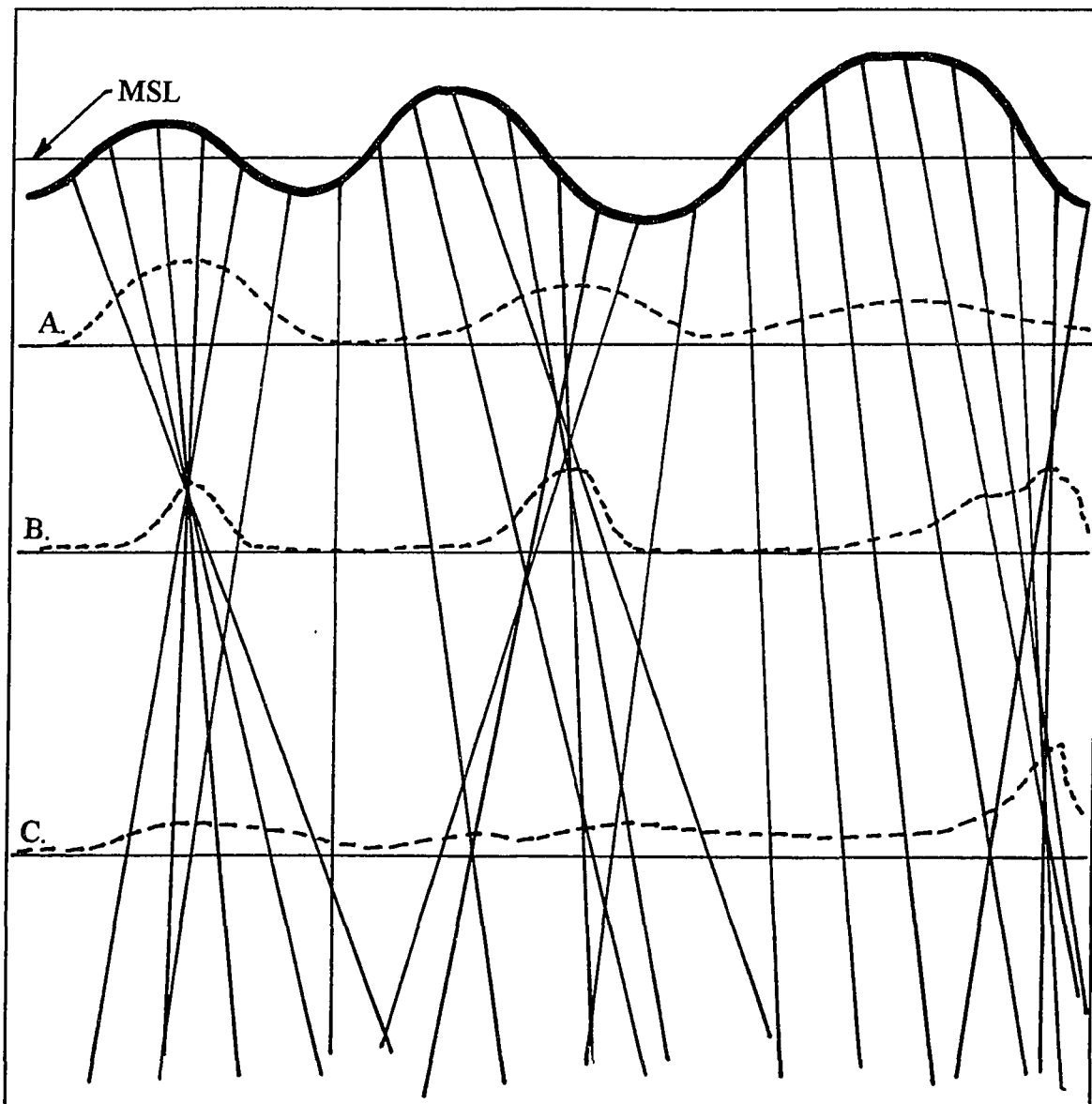
Figure 2.33. Geometry of the velocity bunching mechanism associated with SAR imaging of the ocean surface. The uppermost line represents the ocean surface, while the dashed lines A, B, and C represent image planes at increasing distances from the sensor (Hasselmann et. al 1985).

Acceleration smear is due to the motion of the ocean surface during the coherent integration time. Since the principle mechanism of SAR imaging is the use

of the Doppler shift to improve resolution for a relatively small antenna, the return from a given target is recorded a number of times while the relatively wide SAR beam sweeps by the target. During this time the passage of a wave causes the elevation of the ocean surface to change. Thus, as the sensor records the series of range locations of the target, the target itself moves. This results in an inaccurate range location of the target (Hasselmann and Hasselmann 1991). However, because the satellite velocity is extremely high and the coherent integration time is so small, the ocean surface typically appears stationary (Beal et al. 1983). The coherent integration time of ERS-1 is 0.6 seconds. Therefore, a 16 foot wave with a 10 second period will vary 1.9 feet in elevation during the coherent integration time. During the coherent integration time, the sensor is imaging a 5 km band of data along-track. Since the entire ocean surface is moving while the sensor is integrating range locations of the surface, all wave form locations will be equally modified, and there will be little relative error between consecutive wave crests.

Layover is a condition inherent to radar images which causes an apparent extension of surfaces tilted toward the signal transmitter, and a shortening of surfaces angled away from the transmitter. Gower concludes that layover is evident in the range direction, and, to be consistent with the term velocity bunching, refers to it as "range bunching." This layover tends to slightly distort the wave forms, but does not play a dominant role in the imaging of ocean waves (Gower 1983).

2.3.3 Hasselmann Method

Klaus and Susanne Hasselmann (1991) have developed a closed, nonlinear method of mapping an ocean wave spectrum into a SAR image spectrum, then inverting it to determine the wave spectrum. An initial first guess wave model must be established, and the information it provides used to create a noise free transformation of the SAR image spectrum. Hasselmanns use the Wave Modeling

Group's program (WAM) to determine these initial parameters. WAM has the flexibility to use any bathymetric conditions, any location relative to a coast, and any geographic location. After combining the WAM model with the SAR image spectrum, the modified SAR image spectrum is transformed back into a wave spectrum and assimilated into the original wave model. This process is iterated until the wave spectrum converges, which usually requires three or four iterations. A flow chart depicting this method is provided in Figure 2.34.
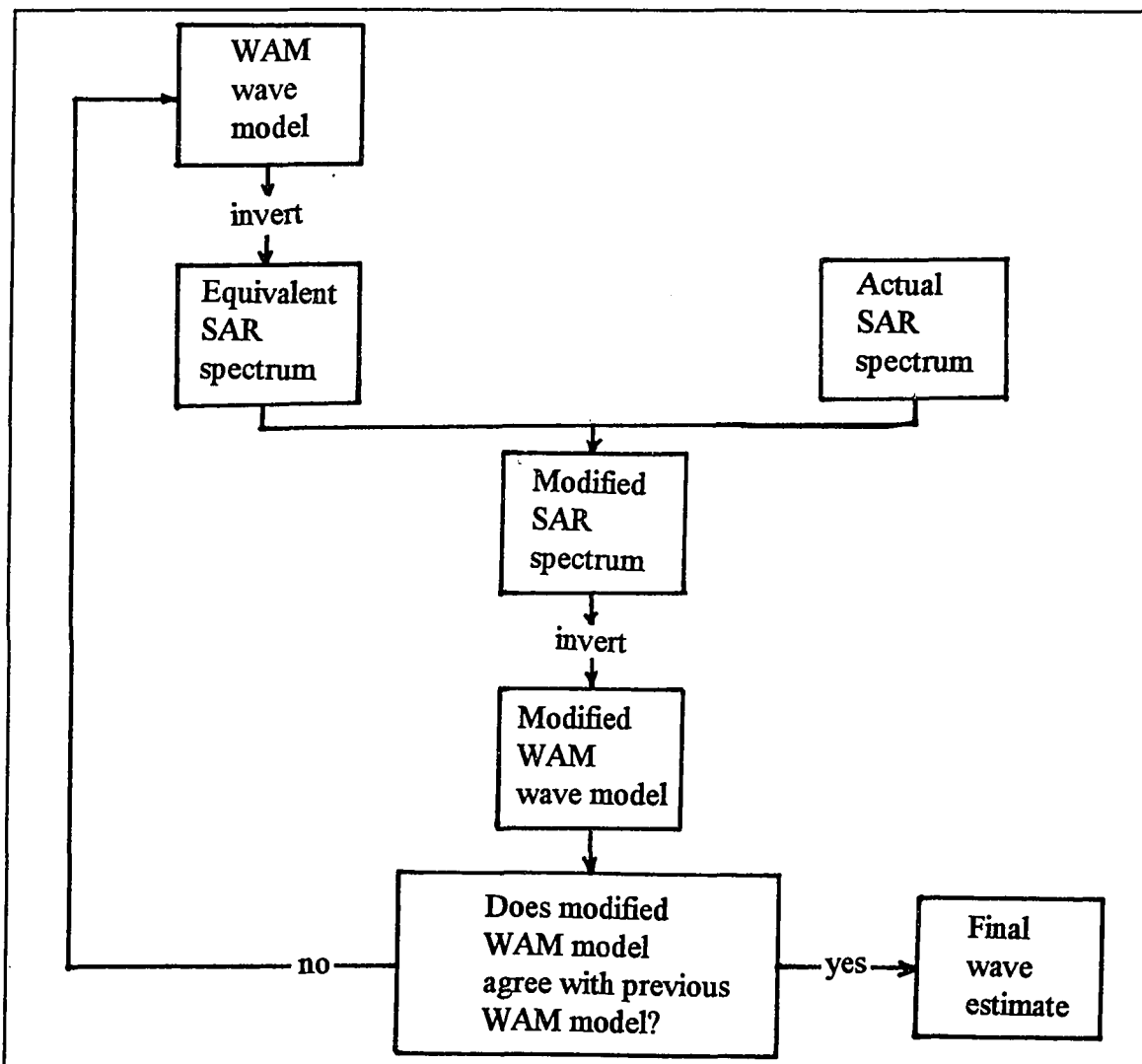
Figure 2.34. Flow chart representing the Hasselmann method.

Despite the closed form of the Hasselmann method, there are several limitations. The first limitation is the need for an initial wave model. Due to the lack of data at many Alaskan sites, an initial model may be difficult to construct. Additionally, information regarding waves traveling in the azimuthal direction relative to the satellite path is lost due to the Doppler shift, and the Hasselmann method cannot be formulated into a general inversion scheme due to the 180^0 ambiguity in direction discussed in Section 2.3.2. To improve their method, the Hasselmanns have suggested further research be conducted to develop an inversion scheme which would modify the wind field of the input model rather than modifying the wave field directly. The altered wind field would then modify the wave field, and thereby ensure dynamic consistency between the wind and wave fields. Currently the Wave Modeling (WAM) Group is studying this possibility (Hasselmann and Hasselmann 1991).

Formerly the Monte Carlo method had been used, but that method computed the SAR image spectrum pixel by pixel and was very time consuming. The Hasselmanns' closed method negates the need for this computation and does not include the sampling uncertainty associated with statistical evaluation. Although the Hasselmanns' method uses a highly nonlinear integral transformation, the Gaussian nature of the input wave field is not affected by that nonlinearity, and a closed solution can be found.

2.3.4 Alaska SAR Facility Wave Product

The Geophysical Processor System (GPS) of the Alaska SAR Facility (ASF) is capable of producing a wave product which contains the wave length directional spectra of the ocean surface. The wave product algorithm requires a full resolution SAR image for input and generates the directional wave spectra for a strip of subscenes, each 512 by 512 pixels, oriented parallel or perpendicular to the azimuthal

travel direction of the satellite. Example subscene locations are illustrated in Figure 2.35.
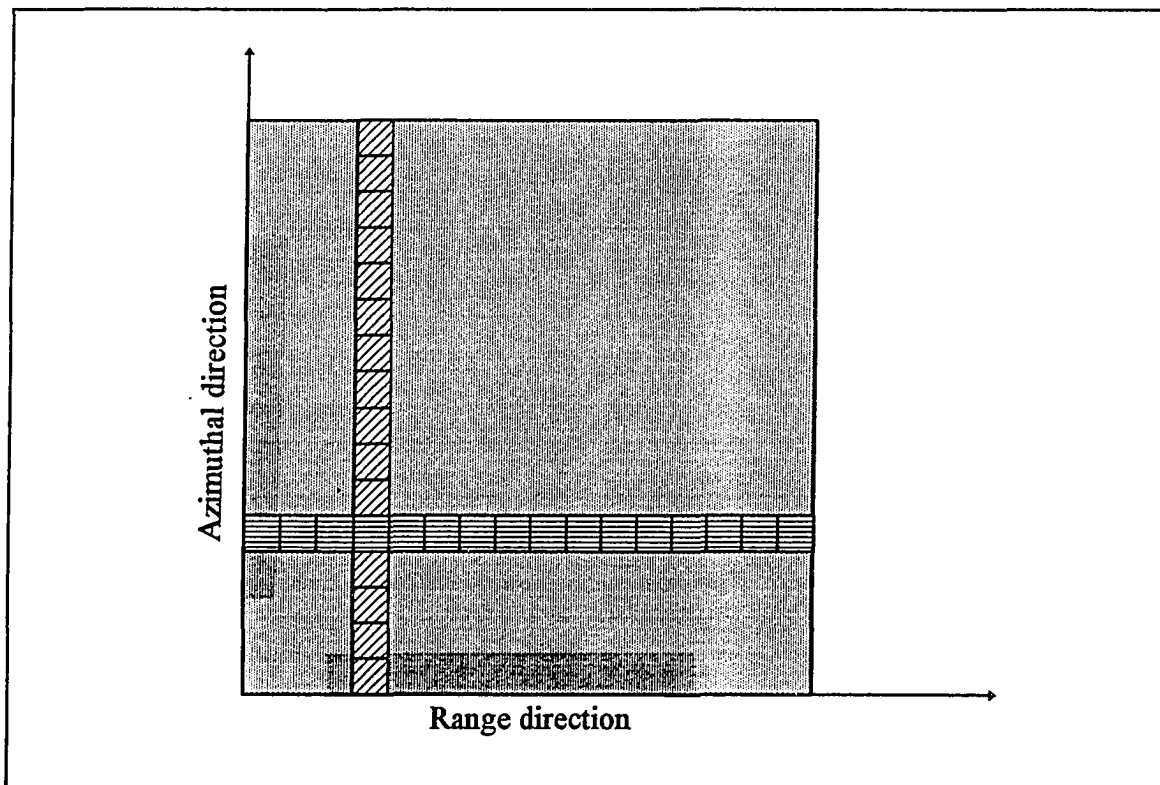
Figure 2.35. Possible locations of wave products where each box is 512 pixels by 512 pixels.

The wave product algorithm is composed of three basic operations: Fourier Transform of the water surface, smoothing of the transform, and detection of peaks in the resulting spectra. Table 2.4 lists the input and processing steps required for generation of the wave product.

Wave Spectra Analysis	
Input	Full-res SAR data
	Subscene location
Processing	Fourier analysis
	Smoothing with Gaussian filter
	Peak detection
Output	Directional wave length spectra text file
	Directional wave length spectra graphics postscript file

Table 2.4. Summary of steps for obtaining the wave product from the Geophysical Processor System.

Because SAR data are recorded as discrete two dimensional matrices rather than continuous data, the 2-D Discrete Fourier Transform is applied. For simplicity, discussion will begin with the one dimensional transform. Mathematically the data series, since samples are spaced uniformly, may be represented by the following.

$$D = \{f(0), f(1), f(2), ..., f(N-1)\} \qquad (2.19)$$

where D = set of numerical intensity values collected by SAR sensor

$f(x)$ = numerical intensity value collected by SAR sensor and assigned to a given pixel, x

N = number of samples

The Discrete Fourier Transform is then given in Equation 2.20.

$$\Im[f(x)] = F(u) = \frac{1}{N} \sum_{x=0}^{N-1} f(x) \exp\left(\frac{-i2\pi ux}{N}\right) \tag{2.20}$$

where $\Im[f(x)]$ = Discrete Fourier Transform of f(x) given by F(u)

$i = \sqrt{-1}$

u = 0, 1, 2,..., N - 1

The inverse DFT (IDFT) may be applied to return the FT to the original series. The IDFT is given below.

$$f(x) = \sum_{u=0}^{N-1} F(u) \exp\left(\frac{i2\pi ux}{N}\right) \tag{2.21}$$

where f(x) = original series

$i = \sqrt{-1}$

x = 0, 1, 2, ..., N - 1

If the one dimensional series is expanded into a two dimensional matrix, the 2-D DFT may be written as shown in Equation 2.22.

$$\Im[f(x,y)] = F(u,v) = \frac{1}{MN} \sum_{x=0}^{M-1} \sum_{y=0}^{N-1} f(x,y) \exp\left[-i2\pi\left(\frac{ux}{M}+\frac{vy}{N}\right)\right] \tag{2.22}$$

where $\Im[f(x,y)]$ =two dimensional dicrete Fourier Transform equal to F(u,v)

M = number of rows in matrix

N= number of columns in matrix

x= row of interest in the original matrix

y= column of interest in the original matrix

i= $\sqrt{-1}$

u= 0, 1, 2, ..., M - 1

v= 0, 1, 2, ..., N - 1

The 2-D IDFT is given by Equation 2.23.

$$f(x,y) = \sum_{u=0}^{M-1} \sum_{v=0}^{N-1} F(u,v) \exp\left[i2\pi\left(\frac{ux}{M} + \frac{vy}{N}\right)\right] \qquad (2.23)$$

where F(u,v) = 2-D DFT

M= number of rows in matrix

N= number of columns in matrix

u= row of interest in transformed matrix

v= column of interest in transformed matrix

i= $\sqrt{-1}$

x= 0, 1, 2, ..., M - 1

y= 0, 1, 2, ..., N - 1

In the past, Fourier Transforms were impractical due to the large number of complex multiplications required, which was proportional to N^2, where N was the number of samples. However the recent development of the FFT has reduced the calculations to a number proportional to $2 \log_2 N$. For example, computing the DFT on a 512 pixel by 512 pixel subscene would have required 262,144 complex multiplications and approximately 45 minutes on an IBM 7094. However, the FFT

reduced the number of complex multiplications to 4608 and now requires only 5 seconds on the same computer (Gonzalez and Wintz 1987).

$$n = 2^m \tag{2.24}$$

where n = number of rows and number of columns in the original matrix

m = any positive integer

After the original data have been transformed, the resulting matrix, equal in size to the original input matrix, is smoothed with a Gaussian filter. The filter assumes a Gaussian distribution of intensity values as the basis for noise removal, and since radar noise closely approximates this distribution, the filter is particularly useful for SAR images.

From the smoothed, transformed matrix, the spectral peaks are located. Peak detection is composed of several steps, the first of which is the overlay of a Cartesian coordinate system on the smoothed matrix with the origin at the center of the matrix. Due to the symmetrical nature of the matrix, the search for peaks is only conducted in the upper half of the matrix, from 0^0 to 180^0. Next, the mean, μ, and standard deviation, σ, of the entire transformed matrix are calculated. From the defined coordinate system, mean and standard deviation peaks are determined. The location of each value in the matrix is described by a point, $p_{x,y}$, where x and y are the row and column associated with the point under consideration. A peak is defined as any value, $p_{x,y}$, in the matrix such that the following criteria are met.

1) $p_{x,y} > \mu$ where μ is the mean of the entire array

2) $\sqrt{x^2 + y^2} > dist$ where *dist* is an input parameter defining the minimum distance from the origin for which peaks should be located. This is useful to exclude false peaks which may occur at or near the origin.

3) $p_{x,y} > p_{x+i, y+j}$ where i, j = -1,0,1; both i and j $\neq$ 0

4) $\dfrac{p_{x,y}}{p_{(x + N_i, y + N_j)}} > cratio$ where i and j are defined in 3) and N and *cratio* are input parameters

From these criteria the locations of a maximum of six peaks are determined and listed in order of decreasing magnitude. Contour plots are then generated depicting the peaks much like mountain peaks would be represented on a topographic map. The reciprocal of the radial distance from the center of the plot to the peak represents the wave length of the peak. Direction of wave propagation is 90^0 counter-clockwise or clockwise from the peak. The uncertainty of the direction is due to the 180^0 directional ambiguity discussed. An illustration of the resulting wave product is provided in Figure 2.36. Due to velocity bunching, the GPS provides a warning if the wave direction is within 30^0 of the azimuthal direction. Occasionally false peaks are detected; however in the majority of test images, the peak finding algorithm was consistent with actual wave peaks (Kwok 1993).

IMAGE ID,   157547100
PRODUCT ID,   20959310
CGM FILE ID,   20959320.dat

PEAK #	WAVE LEN (m)	DIR (deg wrt/N)	PEAK #	WAVE LEN (m)	DIR (deg wrt/N)
1	106.7	103.8, 283.8	4	70.5	153.2, 333.2
2	68.8	104.4, 284.4	5	70.7	173.7, 353.7
3	80.1	58.3, 238.3	6	63.0	32.7, 212.7
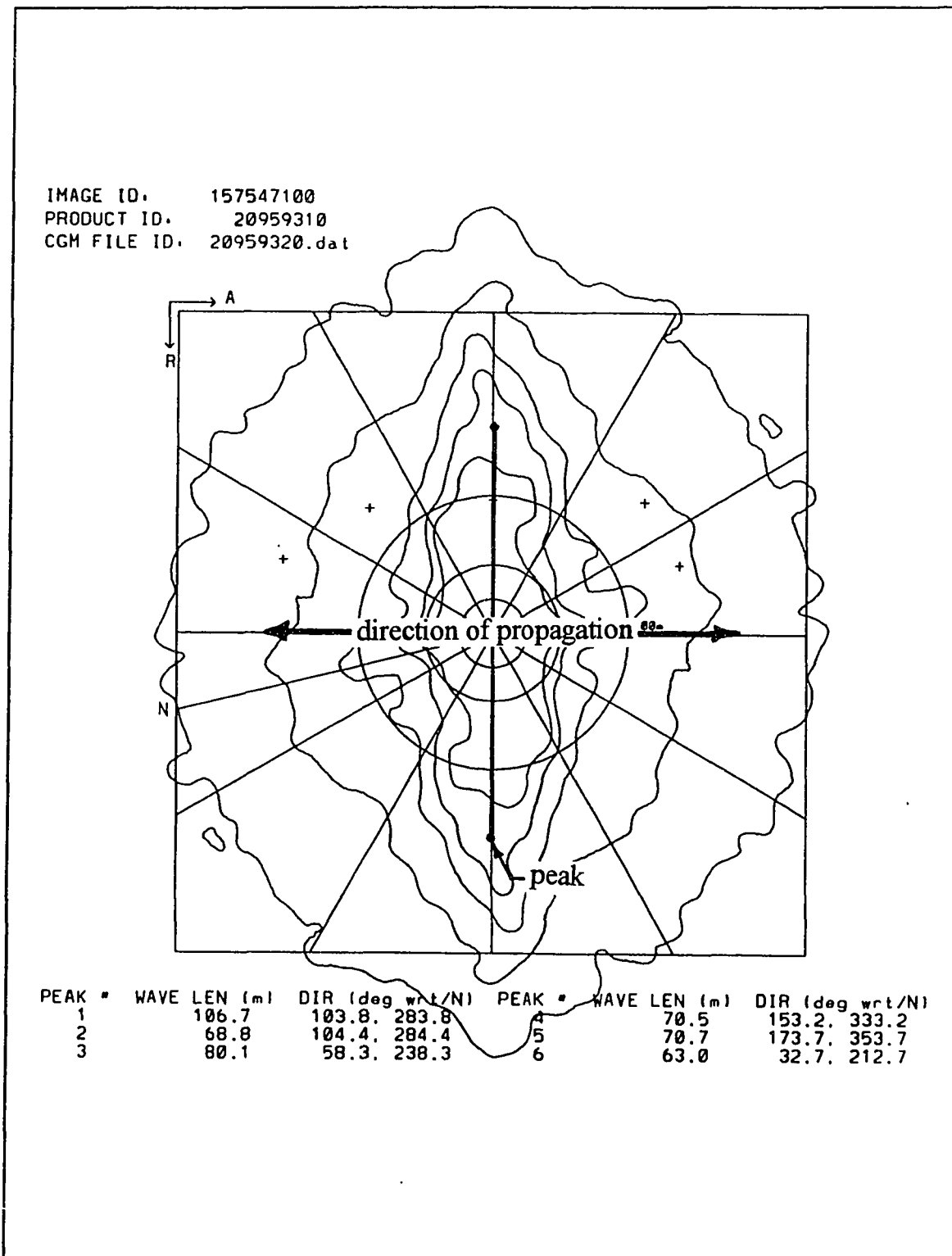
Figure 2.36. Wave product generated by the Geophysical Processor System at the Alaska SAR Facility.

The wave product output received by a SAR user consisted of a text file listing the information necessary to generate the contour plot on the graphics package developed by the National Center for Atmospheric Research (NCAR Graphics). However the graphic representation may be saved as a postscript file through the on-line ordering and archiving system available through the ASF. The postscript file may then be transferred to a directory which is accessible to the user. Although several wave products were obtained for the sites associated with this project, the ASF discontinued its GPS products as of December, 1994 due to lack of interest and funding. However, the ASF coordinators are optimistic that GPS products will be available in some form by June, 1996, provided funding can be obtained. In the future SAR users may be required to create their own wave products via an updated GPS algorithm interface installed on a workstation. Access to wave products would still be restricted to official SAR users. However, because the products are graphic derivatives of the original data, users may be given more leniency in the distribution of wave products.

Research Goal and Objectives

This project examined the use of SAR data to improve the estimating procedures of wave parameters needed for coastal engineering: wave length, wave direction, wave height, wave period, and duration. This goal was accomplished through the objectives listed below.

1) Estimate wave length. wave direction, wave spectra. wave height, wave period, and duration of storm attack from SAR data.

2) Provided these wave parameters may be determined from SAR data, compare these estimates to actual wave parameters measured by buoys or recorded from visual observation.

3) Based on this comparison, define the applications and limitations of SAR based wave parameter estimations.

4) If it is determined that SAR is an effective tool for estimation of wave parameters, investigate the possibility of developing a standardized technique to incorporate them into coastal engineering design practices.

Method of Analysis

The method of analysis followed directly from the Research Goal and Objectives outlined in Chapter 3. Wave parameters from SAR data were estimated, and these estimates compared to actual data. Criteria for application of SAR based parameters were determined, and finally, assimilation of SAR products into coastal engineering was evaluated.

4.1 Estimation of Wave Parameters

The wave parameters were examined in three groups: wave power spectrum and height; wave length and direction; and wave period and storm duration. To determine the SAR spectrum and height from SAR data, the raw image was filtered with the image analysis software, PCI, and the intensity patterns analyzed in a computational software package, Matlab (Matlab 1992). SAR wave length and direction could be obtained directly from the GPS until December of 1994 when the system was discontinued. At that point an algorithm was developed to duplicate the

data formerly provided by the GPS. Once the algorithm was validated, several more wave products were created from SAR data. The determined wave heights, wave lengths, wave directions, wave periods, and durations were then compared to actual wave parameters measured via wave buoys and visual observations.

4.1.1 Site Selection

Because ERS-1 has no on board storage and the other operational SAR sensors have limited storage, collection of SAR data by the ASF was limited to areas in close proximity of the facility. This limiting receiving range, called the station mask, is shown in Figure 4.1 and formed the primary factor in site selection.
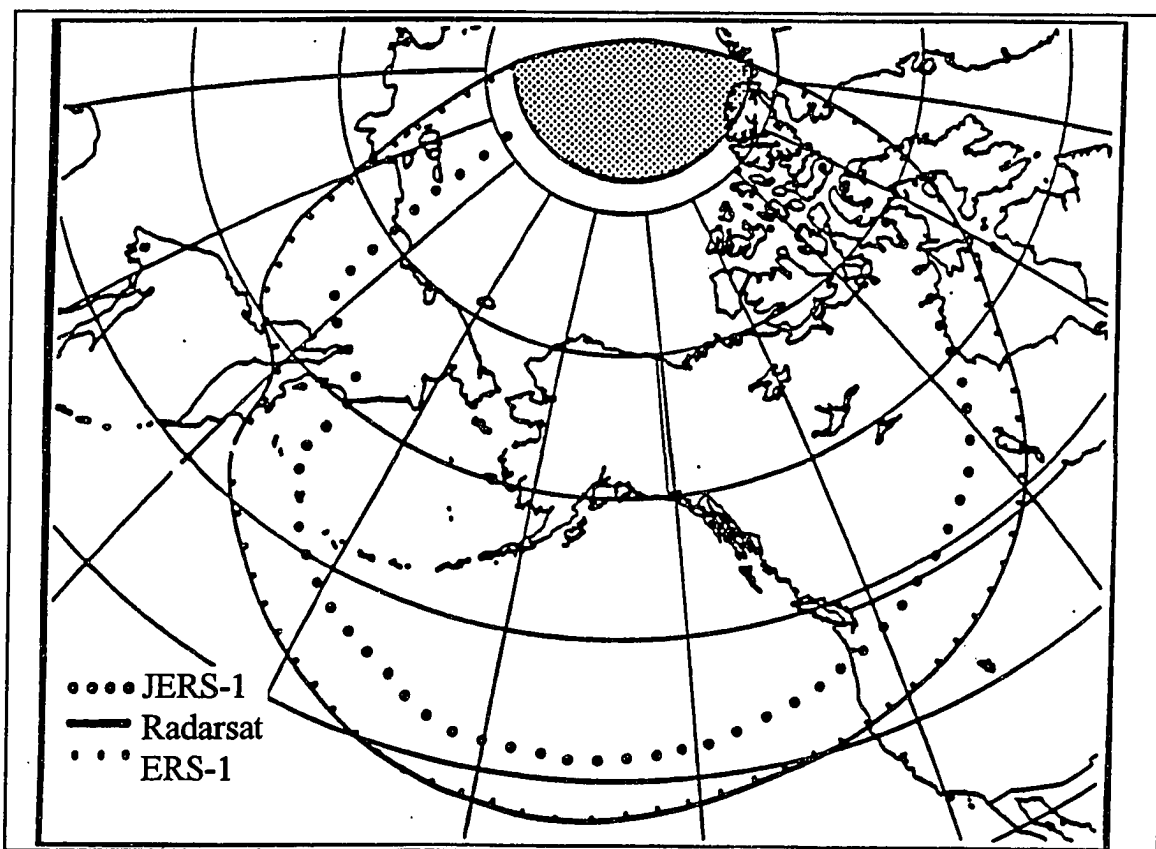
Figure 4.1. ASF station mask for ERS-1 and -2, JERS-1, and Radarsat (DeSoto et. al 1991).

Since wave data were sparse within the station mask and ERS-1 data had only been collected since 1991, potential sites were reduced to three possibilities: Resurrection Bay, near Seward, Alaska (USCOE and IMS 1994); Camden Bay off the Arctic Coast of Alaska in the Beaufort Sea (ARCO 1993); and Grays Harbor, Washington, approximately 45 miles north of the mouth of the Columbia River (Scripps Institute of Oceanography 1992). Locations of the sites and areas where actual parameters were measured are given in Figures 4.2 through 4.4.

NOAA Chart 16680
Scale: 1:200,000 at Lat. 60°00'
Soundings in Fathoms at MLLW
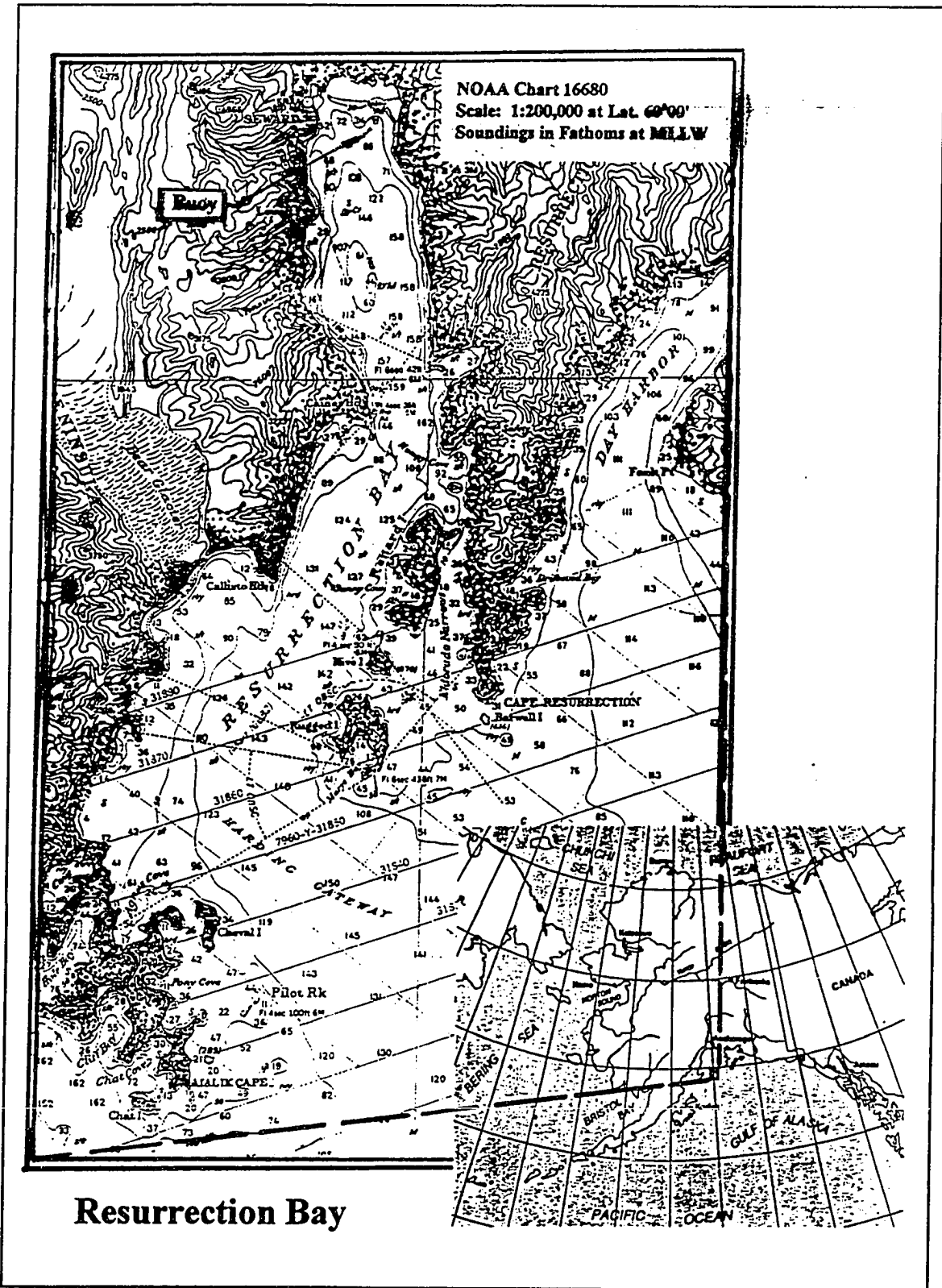
Resurrection Bay

Figure 4.2. Resurrection Bay, near Seward, Alaska.
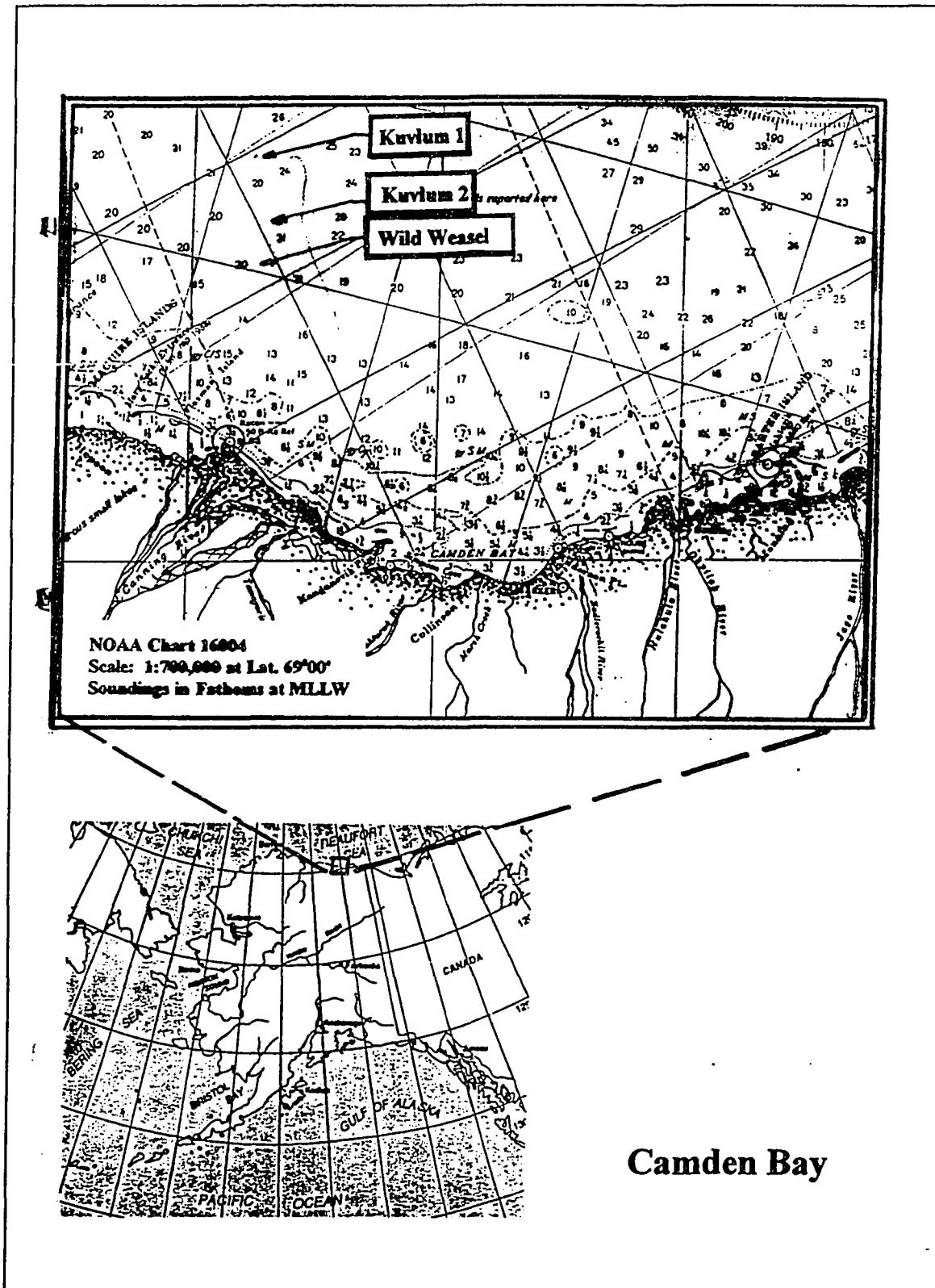
Figure 4.3. Camden Bay, off the Arctic Coast of Alaska.
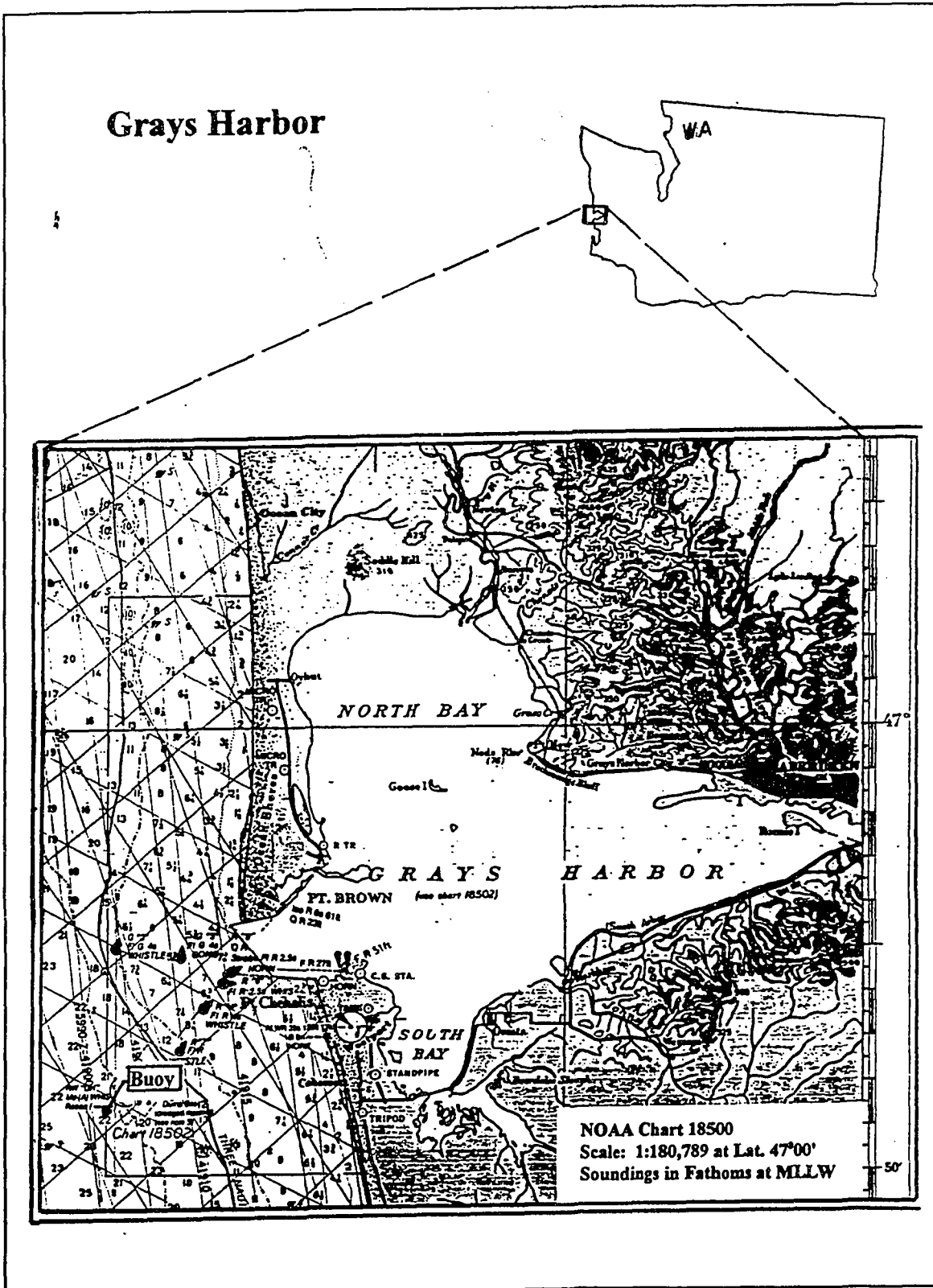
Figure 4.4. Grays Harbor, Washington.

4.1.2 Raw SAR Images

The basic SAR image formats from the ASF were full-resolution and lo-resolution. The full-resolution images had 12.5 meter pixel spacing, and typically waveforms were undetectable due to the speckled quality of the data. Therefore, despite the desirability of the higher resolution, full-resolution images were impractical for examination of the wave spectra and wave heights, and hence wave period and duration. However, as will be discussed in section 4.5, the full-resolution images are useful for determination of wave lengths and directions.

Lo-resolution images are 8-look products created by averaging 8 pixel by 8 pixel windows of the full-resolution image. The averaging, while increasing the pixel size from 12.5 meters to 100 meters, greatly reduces the speckle and improves detection of ocean waveforms. Therefore, lo-resolution images were used for determination of the wave spectra and wave heights. Examples of a full-resolution and a lo-resolution image are provided in Figure 4.5.

4.1.3 Image Analysis

The lo-resolution images were further analyzed in the space and spatial frequency domains, the second of which will simply be referred to as the frequency domain, using a software package called PCI. The images were enhanced in the space domain using several intrinsic filters described in Table 4.1. Raw images were manually filtered in the frequency domain after transformation from space domain via the 2-dimensional FFT. The 2-dimensional inverse FFT (IFFT) was applied to return the images filtered in frequency domain to the space domain.

© European Space Agency 1993

(A)

© European Space Agency 1993

(B)
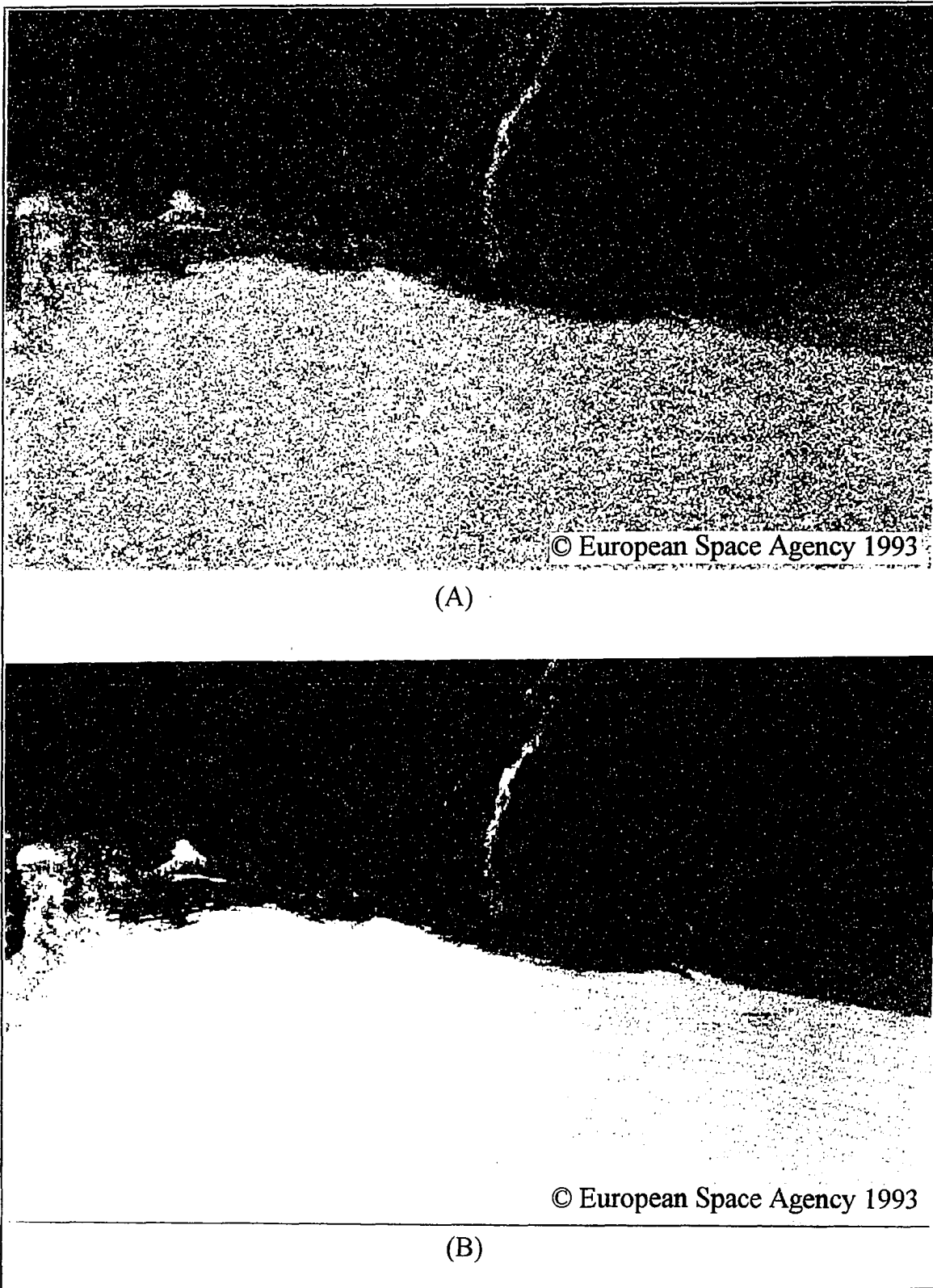
Figure 4.5. Example of (A) full-resolution image and (B) lo-resolution image.

Filter	Typical Use	Algorithm
FFROST	Commonly known as the Frost filter, removes speckle from SAR images while retaining edge features.	Uses an exponentially damped kernel that depends on the statistics of surrounding pixels to adapt itself.
FEFROST	An enhanced version of the Frost filter (FFROST), also used to remove speckle from SAR images while retaining edge features.	Divides image into three classes according to the amount of speckle in a subregion and varies itself to remove random noise accordingly.
FELEE	Commonly known as the enhanced Lee filter, removes speckle from SAR images while retaining edge features.	Allows for removal of additive and/or multiplicative noise using a kernel of odd dimension between 3x3 and 11x11 pixels.
FGAMMA	Removes speckle while retaining edge definition of SAR images.	Performs gamma map filtering on the image. Assumes the probability density function of the image intensity values follows the gamma distribution. Performs spatial filtering on individual pixels based on the intensity values of the surrounding pixels

Table 4.1. Summary of filters applied to SAR images to enhance wave features.

Filter	Typical Use	Algorithm
FKUAN	Removes speckle from SAR images while retaining definition of edges.	Transforms multiplicative noise to additive noise then applies a minimum mean square error criterion. The filter has the same form as the Lee Filter (FELEE), but has a different weighting function.
FAV	An averaging filter that smooths images to remove random noise, such as speckle.	Applies a weighted averaging kernel to each pixel.

Table 4.1. Continued

Frequency domain filtering was feasible through the use of the 2-dimensional FFT and 2-dimensional IFFT algorithms intrinsic to PCI. The algorithms performed the transforms described in Chapter 2 and offered output in real and imaginary form, or magnitude and phase form. The magnitude and phase option was specified because the intensity of the magnitude component indicated the relative significance of a given frequency in the original image. The resulting graphic representation of the transform displayed frequencies that increased radially outward from the origin which was located at the center of the plot. Due to the directional ambiguity associated with still imaging of a moving surface, output was symmetric about the origin as shown in Figure 4.6.
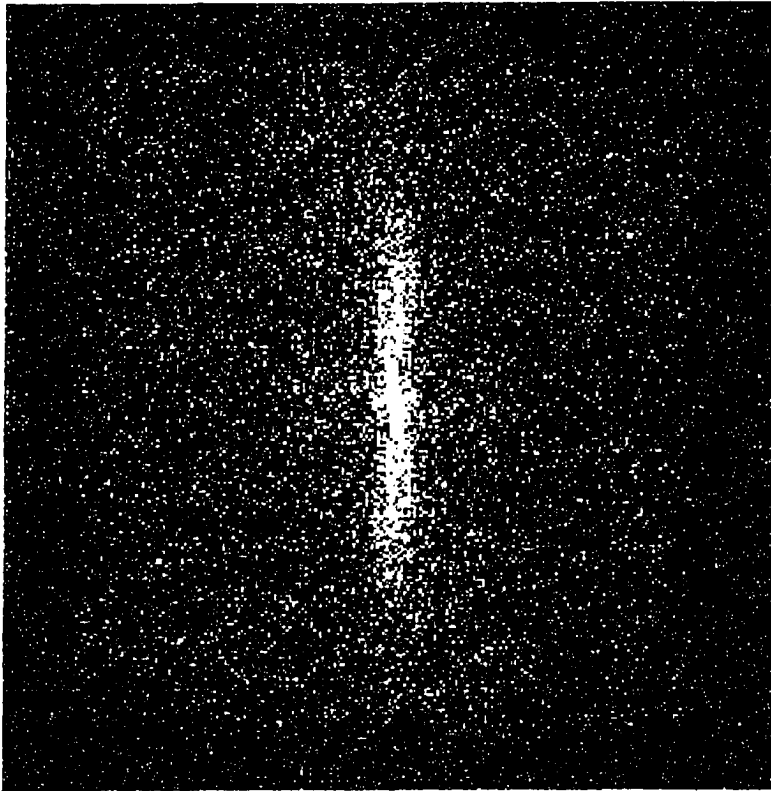
© European Space Agency 1993

Figure 4.6. Magnitude component of the Fourier Transform was symmetric about the origin located at the center of the image, where distance from the center represents 1/wave length. Direction of wave propagation can be determined from angular location, and gray level intensities represent power associated with any given wave length and direction.

While in the frequency domain the image was filtered by manually applying a mask to remove non-periodic brightness. The mask was designed to encompass the low frequency information and reject the high frequency information. An

example is illustrated in Figure 4.6. After the filter was designed for the magnitude component of the frequency transform, it was applied to the phase component. The two components were then returned to the space domain by applying the inverse Fourier Transform.
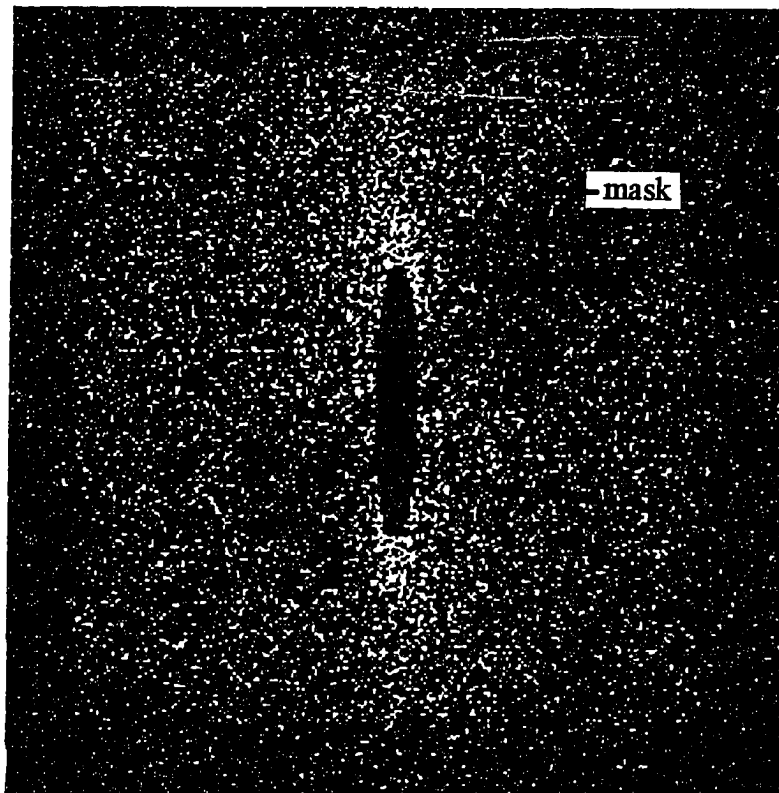
© European Space Agency 1993

Figure 4.7. Magnitude component of the Fourier Transform overlain by a manually created mask.

4.1.4 Wave Heights and SAR Based Power Spectra

Two methods were used to determine the power spectra. The first was based on a single wave ray, and the second determined by averaging the power spectra for several parallel wave rays. In both cases a single power spectrum was computed for each image and several power spectra were calculated for subscenes within a given image to evaluate variation of the spectra as the waves progressed shoreward. Provided the SAR power spectra agreed with the measured power spectra, the wave height could then be back calculated from the power.

4.1.4a Single Wave Ray Power Spectra

The graphic capabilities of PCI were used to create a visually interpolated, single wave ray on an image, and the intensity values under the ray saved as a text file. The text file was imported into Matlab where the power spectrum was computed along the entire ray. Additionally, the power spectra from several overlapping subscenes along the same ray were computed. The results were combined and displayed as a spectrogram, in which the vertical axis represented the reciprocal of wave length, the horizontal axis represented distance from shore, and the brightness of the interior gray levels indicated the relative power associated with a given wave length at a particular distance from shore. An example of a spectrogram is given in Figure 4.8.
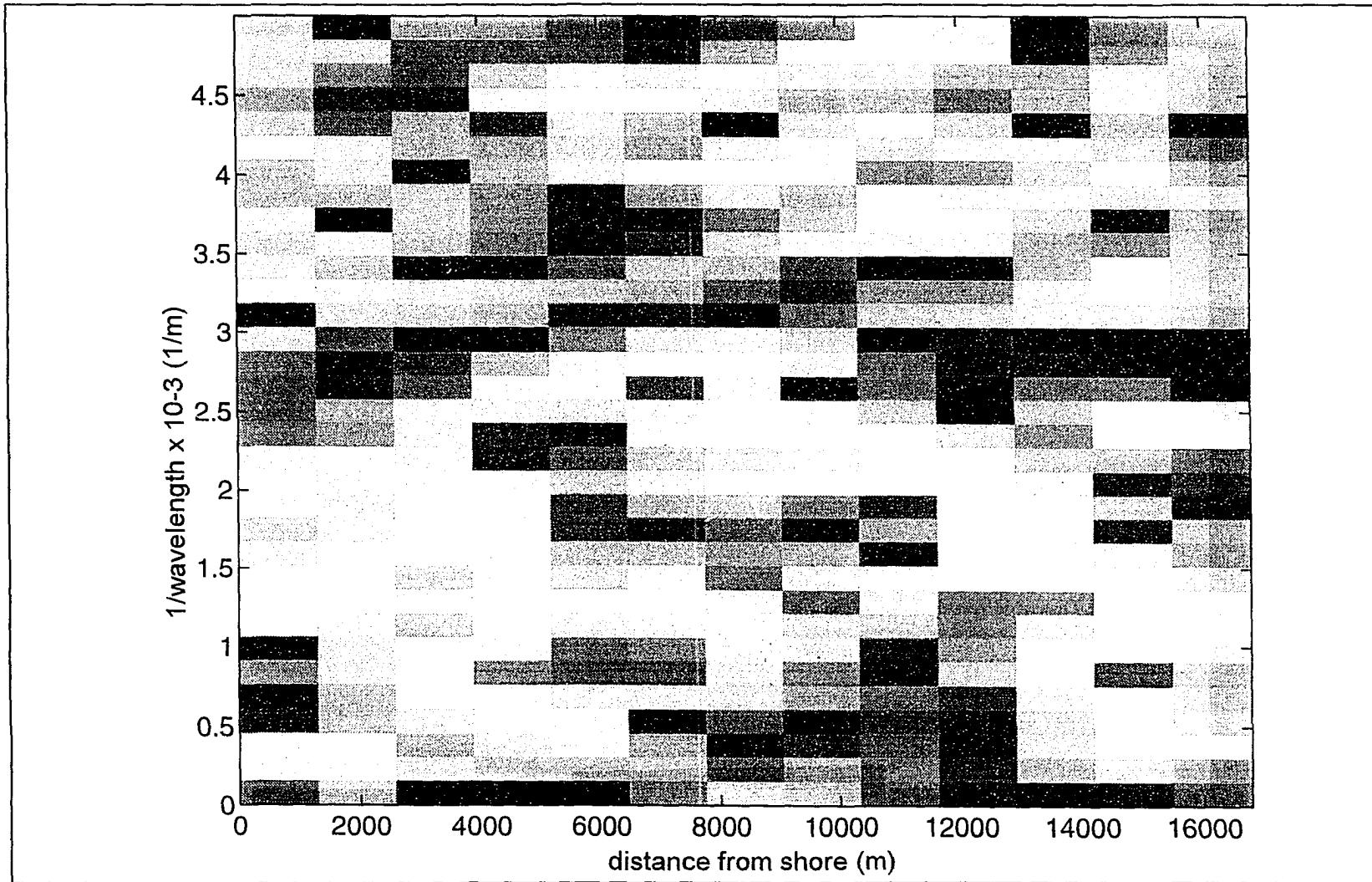
Figure 4.8. Spectrogram created in Matlab. The intensity of the gray values represents the power associated with any given wave length reciprocal and distance from shore.

4.1.4b Averaged Wave Ray Power Spectra

To reduce random noise associated with the raw SAR image, several parallel wave rays were constructed, the power spectrum of each ray was computed, and these spectra averaged together. Each SAR image is composed of an array of square pixels. Therefore, if a wave ray is drawn such that it follows neither the horizontal or vertical directions, a step-like, rather than smooth, ray results. The jagged ray results in irregularly spaced intensity values stored in the text file. Because the Fourier Transform assumes samples are evenly spaced, and furthermore, Matlab is a matrix based software package in which only rectangular arrays may be analyzed, the raw SAR images were rotated to align the wave crests in the vertical or horizontal directions. Additionally, the rotation of the image facilitated the construction of parallel rays because a rectangle could be masked over the region of parallel wave rays to be exported to a text file. Curved wave rays were divided into several straight ray approximations.

4.1.5 Wave Length and Direction

The dominant SAR based wave lengths were determined from the one dimensional power spectra described in Section 4.1.4, directly from the GPS wave product, and from the two dimensional power spectra calculated in Matlab. However, the dominant wave direction could only be determined from the latter two techniques.

The one dimensional power spectra computed as described in Section 4.1.4, yielded a graphic display. The vertical axis represented power while the horizontal axis represented the reciprocal of wave length. From these plots, an example of which is provided in Figure 4.9, the dominant wave lengths were determined.
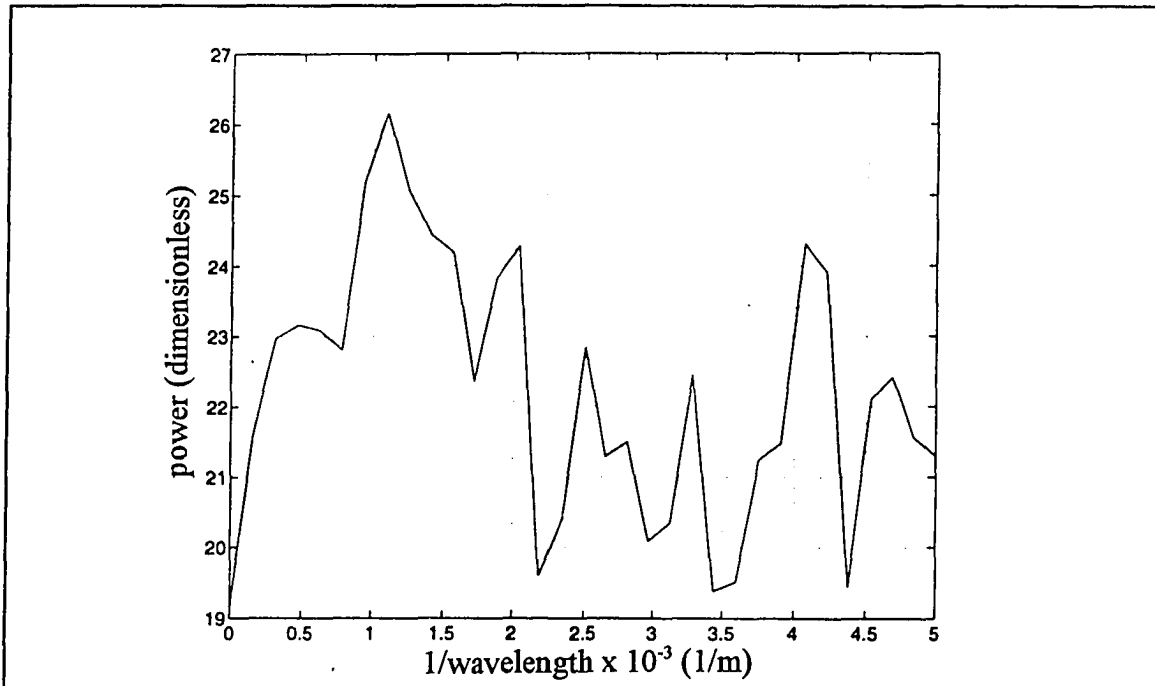
Figure 4.9. Typical plot of one dimensional power spectrum created in Matlab by the single or averaged wave ray techniques.

The GPS wave product and the algorithm used to produce it (Section 2.3.4) provided graphic output of the wave length power spectrum of a full-resolution SAR image. Wave length was represented by radial distance from the origin and direction was indicated by the angular location of the wave peak relative to north. An example of a wave product is provided in Figure 4.10.

The two-dimensional SAR spectra was created by masking a region of the original SAR image in PCI. The region was then exported to Matlab which allowed executable code to be written as a text file for manipulation of matrices. The code used to compute the two dimensional power spectra from the values contained in the matrices is included in Appendix A. The result of the two dimensional power spectrum was compared to the GPS wave product. The Matlab program was used to create wave products for Resurrection Bay because the GPS

was discontinued before the WaveRider Buoy was installed at this site. Additional wave products were also created for Grays Harbor.


```
IMAGE  ID.      159550100
PRODUCT ID.     20965310
CGM FILE ID.   20965320.dat
```

PEAK #	WAVE LEN (m)	DIR (deg wrt/N)	PEAK #	WAVE LEN (m)	DIR (deg wrt/N)
1	104.0	96.3, 276.3	4	75.2	37.3, 217.3
2	82.3	111.9, 291.9	5	71.7	4.1, 184.1
3	91.3	179.7, 359.7	6	73.2	49.4, 229.4
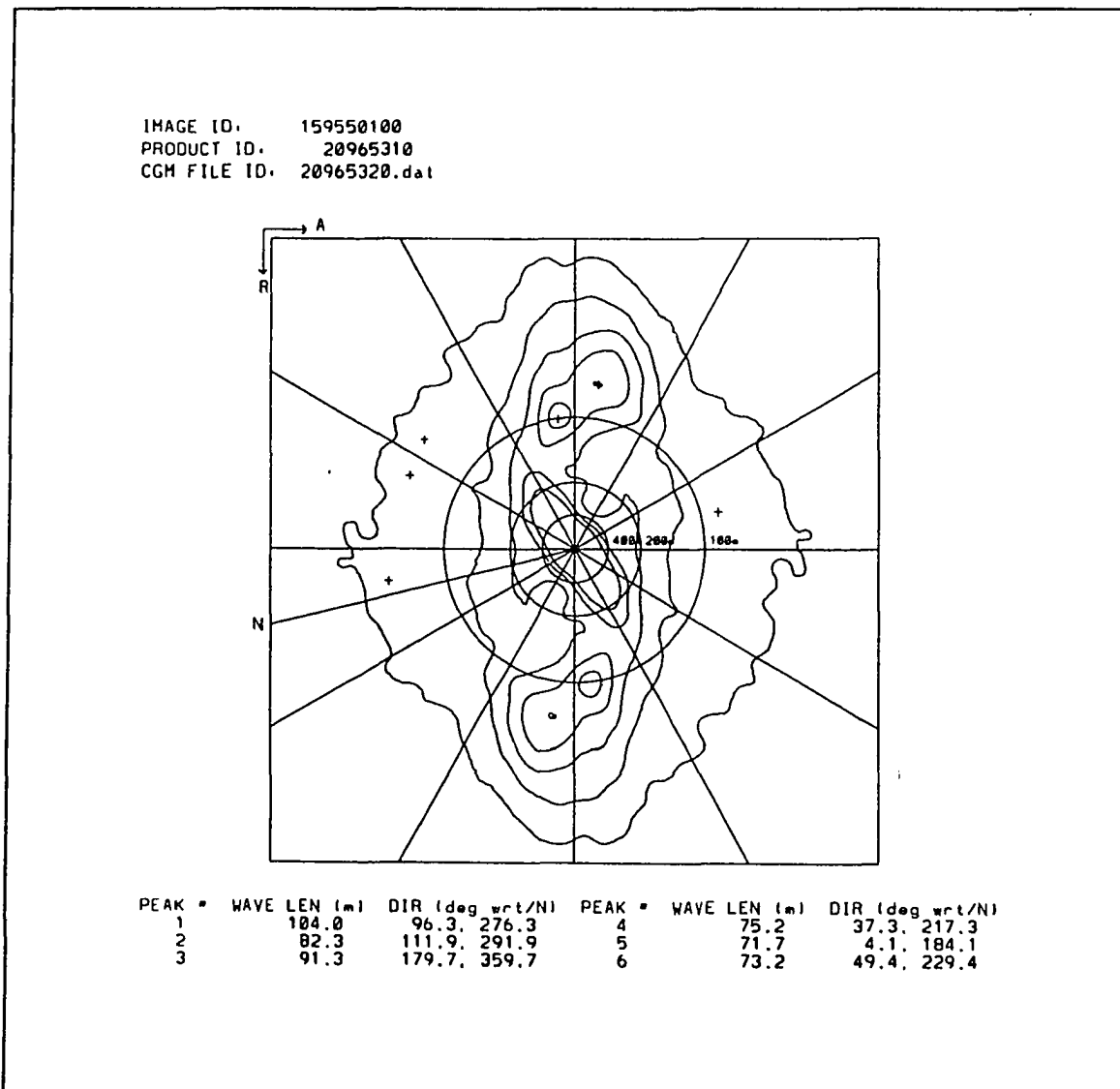
Figure 4.10. GPS wave product. Wave length is measured radially outward from the center and wave direction is represented by the angle between the wave peaks and north.

Wave direction could be extracted directly from the GPS wave product and the two-dimensional SAR spectra generated in Matlab. As described in Section

2.3.4, wave directions were represented by addition or subtraction of 90^0 from the location of the dominant wave peaks on the plots. The 180^0 discrepancy results from imaging a moving surface at an instant in time.

4.1.6 Wave Period and Storm Duration

The determinations of wave period and duration were contingent on determination of a reasonable SAR wave length spectra. In particular, wave period could only be found through comparison of the SAR based wave length spectra with a measured wave frequency spectra. Provided the spectra were similar in shape, the dominant peaks of could be assumed to correspond to the same waves. Therefore, the wave frequency of the peak SAR based waves would be equal to the frequency of the measured peaks, and the frequency inverted to determine wave period. Although period could be determined for this project, provided a reasonably accurate spectra was estimated, extraction of wave period from a single SAR without actual measured spectra was not feasible. Because SAR images a large spatial area at an instant in time no temporal data could be obtained. However, in the future, use of tandem SAR sensors may enable stereo viewing of SAR images which would enable period to be determined based on the distance a given waveform traveled between the imaging of the stereo pair.

Provided accurate wave parameters were determined from SAR images, the duration for which a given region was under storm attack could be determined from consecutive SAR images examined in series. Depending on the latitude of the region of interest, the imaging modes of the SAR sensors, and the number of operational SAR sensors, time between images for a given location would vary between hours and several days. The presence of waves in consecutive images would indicate the duration of the storm event.

4.2 Comparison of SAR Parameters with Measured Parameters

After the SAR wave parameters were calculated as described in Section 4.1, they were compared to actual measured wave parameters to verify their accuracy. The measured data were collected from several sources and in a variety of forms. Some of the data were used directly to evaluate the accuracy of SAR based wave parameters, while some were manipulated with the dispersion equation, a common tool used in coastal engineering, to allow direct comparison of like parameters.

4.2.1 Measured Data

Measured wave data were acquired in formats specific to each site. A summary of the sources and the data collected at each site is provided in Table 4.2. Additional wave data were provided by Fairweather Environmental Services, Inc. for the Chukchi and Beaufort Seas, however the sites were too far offshore to be considered coastal and therefore the data were not used.

Location	Source	Data Recorded
Camden Bay Lat; Long 70° 05';145° 05'	ARCO 1993	Shipboard visually observed significant wave period, and significant wave height
Grays Harbor Lat; Long 46° 51'; 124° 15'	Scripps Institute of Oceanography 1992	Buoy measured significant wave period, significant wave height, and wave energy spectra
Resurrection Bay Lat; Long 60° 06'; 149° 23'	U.S. Army Corps of Engineers and IMS 1994	Buoy measured significant wave period, significant wave height, and wave energy spectra

Table 4.2. Summary of measured wave data sources and formats.

4.2.2 Methods of Comparison

SAR based parameters were compared directly to the recorded data when possible; however, for some sites the data had to be mathematically manipulated prior to comparison. Measured wave spectra were compared directly to SAR based spectra. Since wave height squared was proportional to the power represented in the spectrum, wave heights were also compared. Wave direction was not recorded for any sites, and therefore the SAR estimated wave directions were verified only by comparison with theoretical directions of wave propagation. Because no wave lengths were measured, the dispersion equation (Section 2.6) was used to determine the theoretical wave length associated with recorded wave period at the estimated water depth. Water depth was estimated from NOAA bathymetric charts.

4.3 Criteria for Application of SAR Based Estimates

Through the comparison of SAR based wave parameters with actual measured wave data, the limitations of SAR estimations were established. Alaskan coastal engineers indicated SAR estimated wave parameters would be beneficial if the parameters met the criteria listed below.

Wave Parameter	Acceptable Error
length	±20%
height	±20%
spectra	±1 standard deviation
direction	±15°
period	±20%
duration	±20%

Table 4.3. Acceptable error associated with estimated wave parameters.

4.4 Incorporation into Standard Coastal Design

Provided the accuracy of SAR based wave parameters met the guidelines in Section 4.3, a standardized method for their extraction was developed. The method would address extracting, archiving, and access of the SAR based parameters. To be incorporated into coastal engineering design, the wave climate information derived from SAR data must meet the criteria listed below.

- Be archived in a central location.
- Be readily accessible to all engineers.
- Be reasonably priced.
- Be obtained in a timely manner.

The feasibility of SAR based estimations meeting these four criteria were evaluated based on information provided by the Alaska SAR Facility staff.

Results

The results followed directly from the first two research objectives outlined in Chapter 3: estimate and compare SAR wave parameters with measured wave data. One SAR wave parameter estimation technique included image enhancement prior to the extraction of wave parameters, and the second evaluated the raw SAR images for wave period and duration information. Estimations and comparisons of SAR parameters to measured parameters were made for five SAR images.

5.1 Image Analysis

Full-resolution and lo-resolution images were analyzed in both the space and frequency domains. In the space domain, the Frost, enhanced Frost, enhanced Lee, gamma, Kuan, and averaging filters were individually applied to both the full- and lo-resolution images with approximately the same result. The filters had minimal effect on the lo-resolution images because the images had been enhanced from full-resolution images during their processing at the Alaska SAR Facility

89

(ASF). As might be expected, application of these filters to the full-resolution images gave the images a lo-resolution appearance. Therefore, rather than manually creating a lo-resolution image from the full-resolution image, the lo-resolution product created by the ASF was used. A comparison of an unfiltered and filtered lo-resolution image is provided in Figure 5.1, and a comparison of a filtered and unfiltered full-resolution image is shown in Figure 5.2.

(A)

© European Space Agency 1993

(B)

© European Space Agency 1993
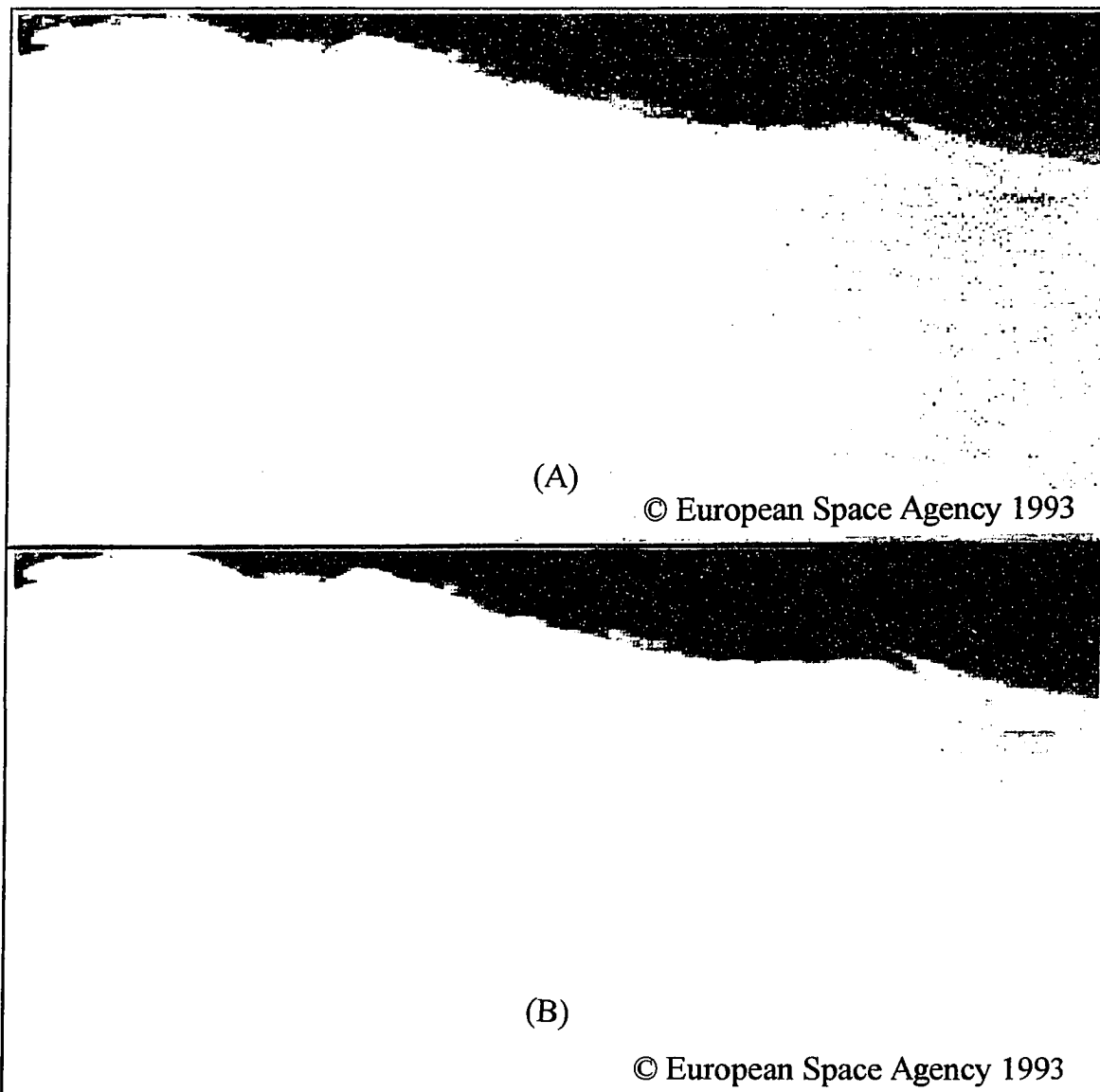
Figure 5.1. Comparison of (A) unfiltered and (B) spatially filtered lo-resolution images.

(A)

© European Space Agency 1993

(B)

© European Space Agency 1993
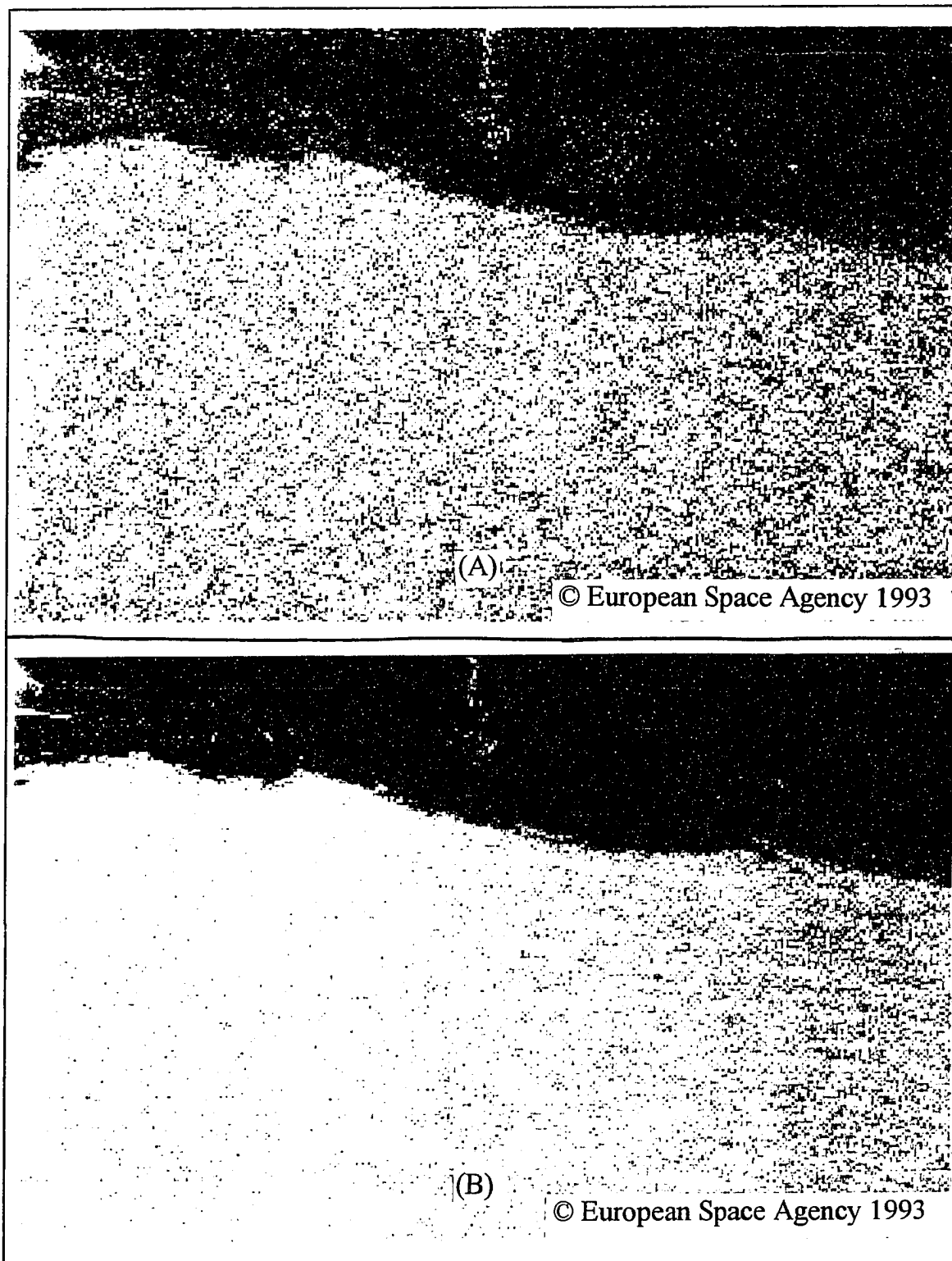
Figure 5.2. Comparison of (A) unfiltered and (B) spatially filtered full-resolution images.

As with the space domain, both full- and lo- resolution images were enhanced in the frequency domain using the filtering technique discussed in Section 4.1.3. The random noise contained in the full-resolution image made it difficult to detect periodic patterns, and resulted in an approximately circular transform which did not lend itself to filtering. An example of a full-resolution image transformed into the frequency domain is provided in Figure 5.3.

© European Space Agency 1993

Figure 5.3. Full-resolution image transformed into frequency domain, where distance from the center represents 1/wave length and direction of wave propagation can be determined from angular location. Gray level intensities represent power associated with any given wave length and direction.

Transformation of the lo-resolution image into frequency domain proved to be more effective than the transformation of the full-resolution image because the

full-resolution image contained significant random noise. The lo-resolution transformed image was dominated by a centered elliptical pattern which clearly indicated propagation direction of the waveforms. The central ellipse was masked by the manually designed filter and transformed back to space domain. The resulting image contained visually well defined wave patterns. The frequency transform of a lo-resolution image is provided in Figure 5.4 and a comparison between the raw lo-resolution image to the filtered inverse transformed image is given in Figure 5.5. In the frequency domain, as in the spatial domain, lo-resolution images were superior to full-resolution images.
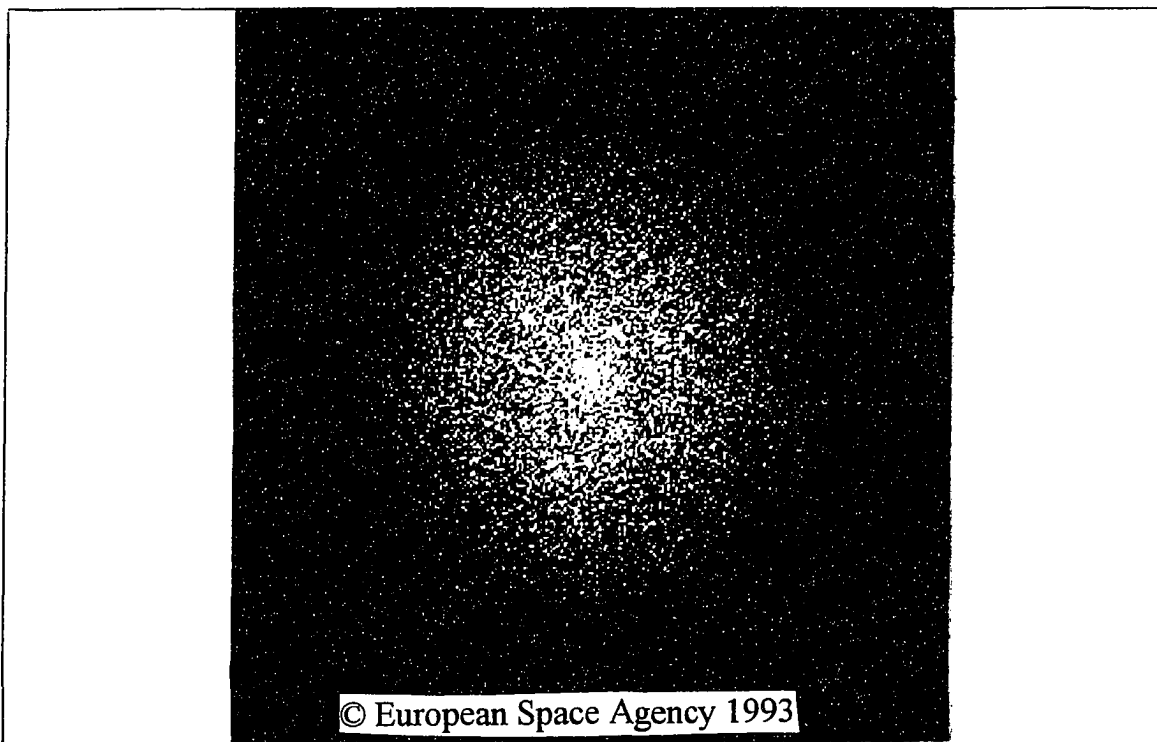

© European Space Agency 1993
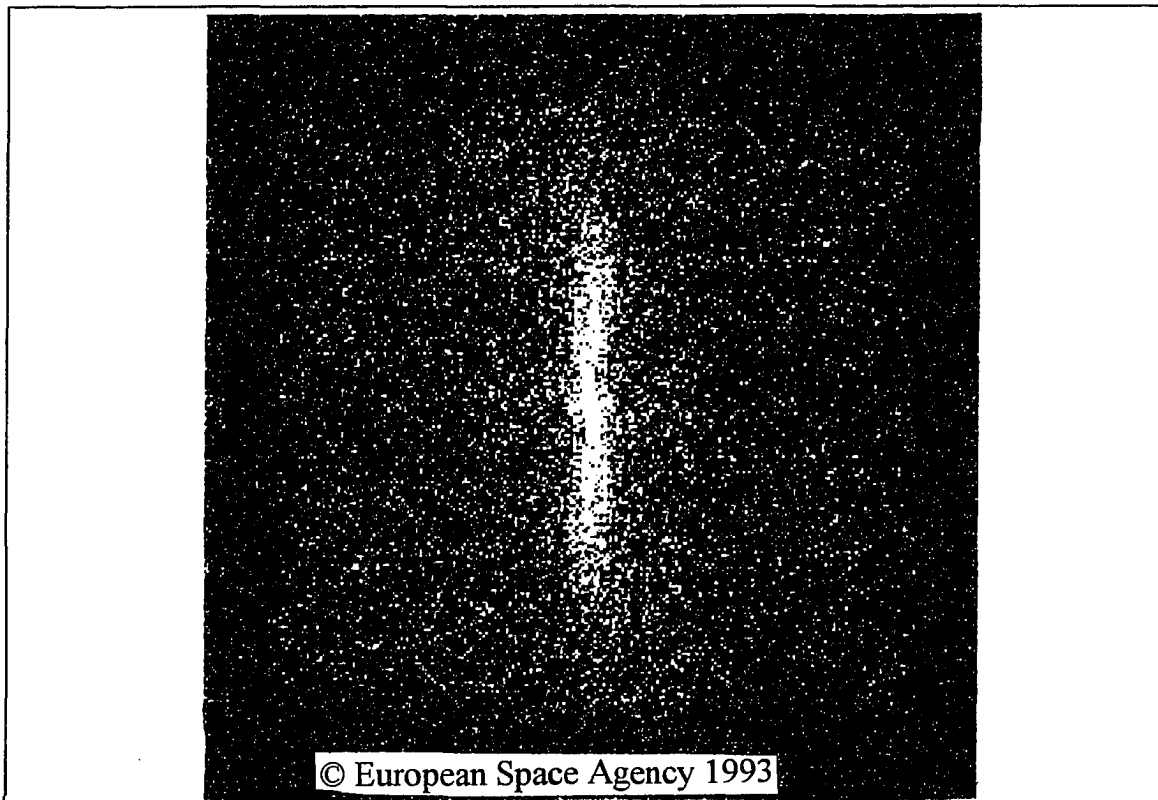
Figure 5.4. Lo-resolution image transformed into frequency domain, where distance from the center represents 1/wave length and direction of wave propagation can be determined from angular location. Gray level intensities represent power associated with any given wave length and direction.

© European Space Agency 1993
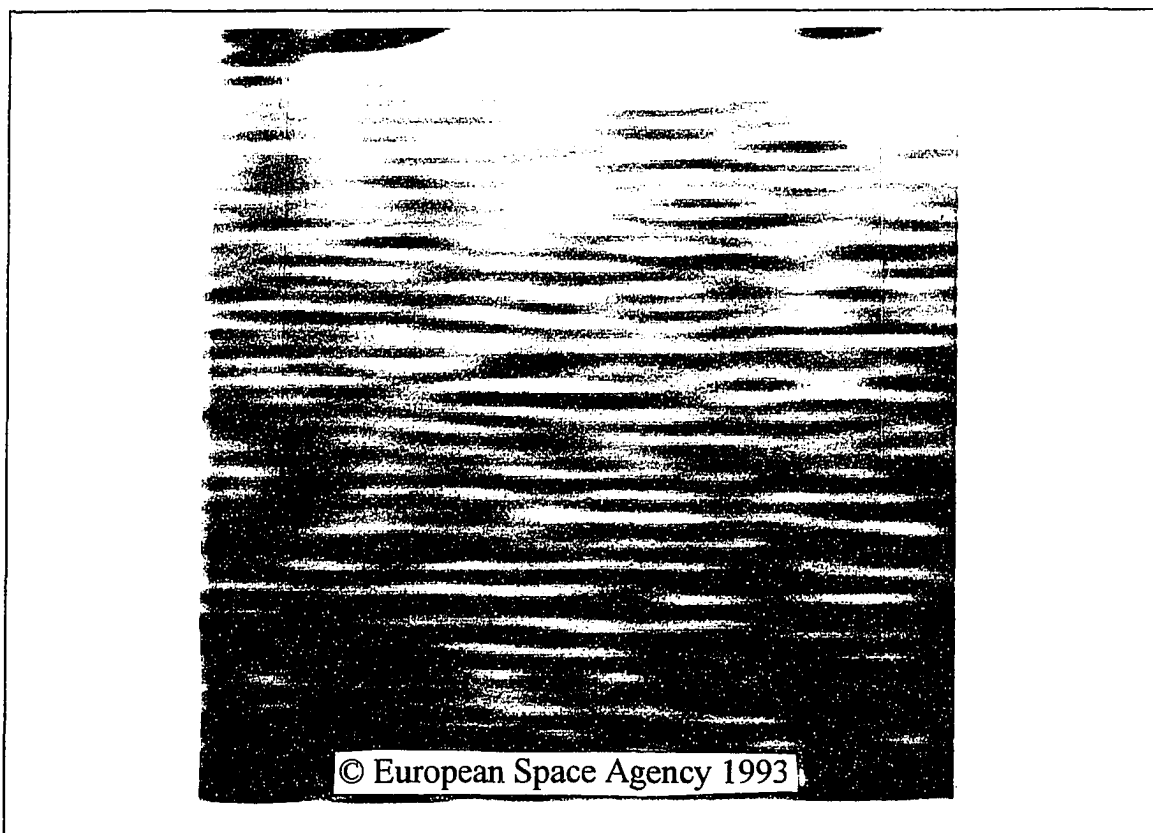
Figure 5.5. Inverse transform of frequency filtered lo-resolution image. The striations indicate the presence of wave crests.

5.2 Power Spectra

The one dimensional power spectrum was computed from a single wave ray on a lo-resolution images that had been filtered in the frequency domain, and also from several averaged power spectra computed from parallel wave rays on the raw lo-resolution images.

5.2.1 Single Wave Ray

A single wave ray was drawn on the inverse Fourier transformed data and the intensity values under the ray were written to a text file. The text file was imported into Matlab, and the power spectrum determined for the entire wave ray.

Additionally, the spectra were computed for several subscenes along the ray and displayed as a spectrogram. For nearly all wave rays, both the single power spectrum and multi-subscene spectra were dominated by long waves as indicated in Figures 5.6 and 5.7. Because of this long wave domination, no shifts in power spectra as the waves propagated shoreward could be detected. Therefore no conclusions could be drawn from their comparison to the theoretical shift of the power spectra. The measured spectra for the same site, shown in Figure 5.8, had no indication of significant power associated with extremely long waves. Although the horizontal axes for the measured and SAR based spectra have different scales, if they agreed, the general shapes of the spectra would be similar. It is likely that random noise in the SAR image, despite efforts to reduce it, caused the spectral peak to shift toward the lower wave frequencies.
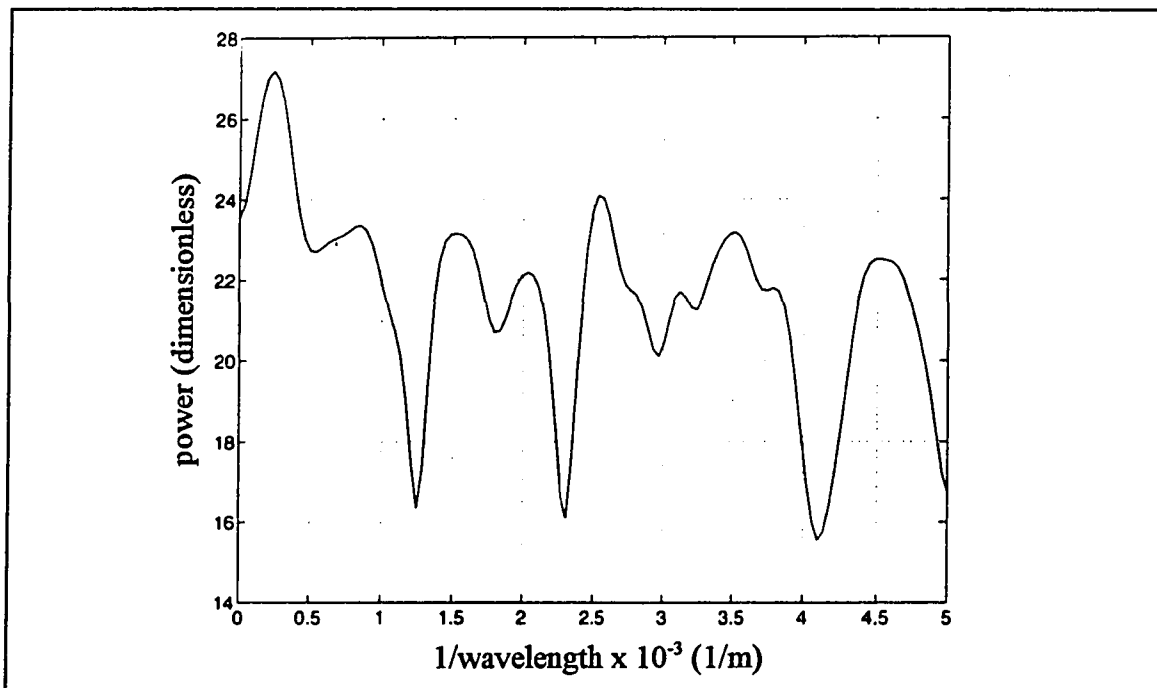
Figure 5.6. SAR based power spectrum computed for a single wave ray at Grays Harbor.
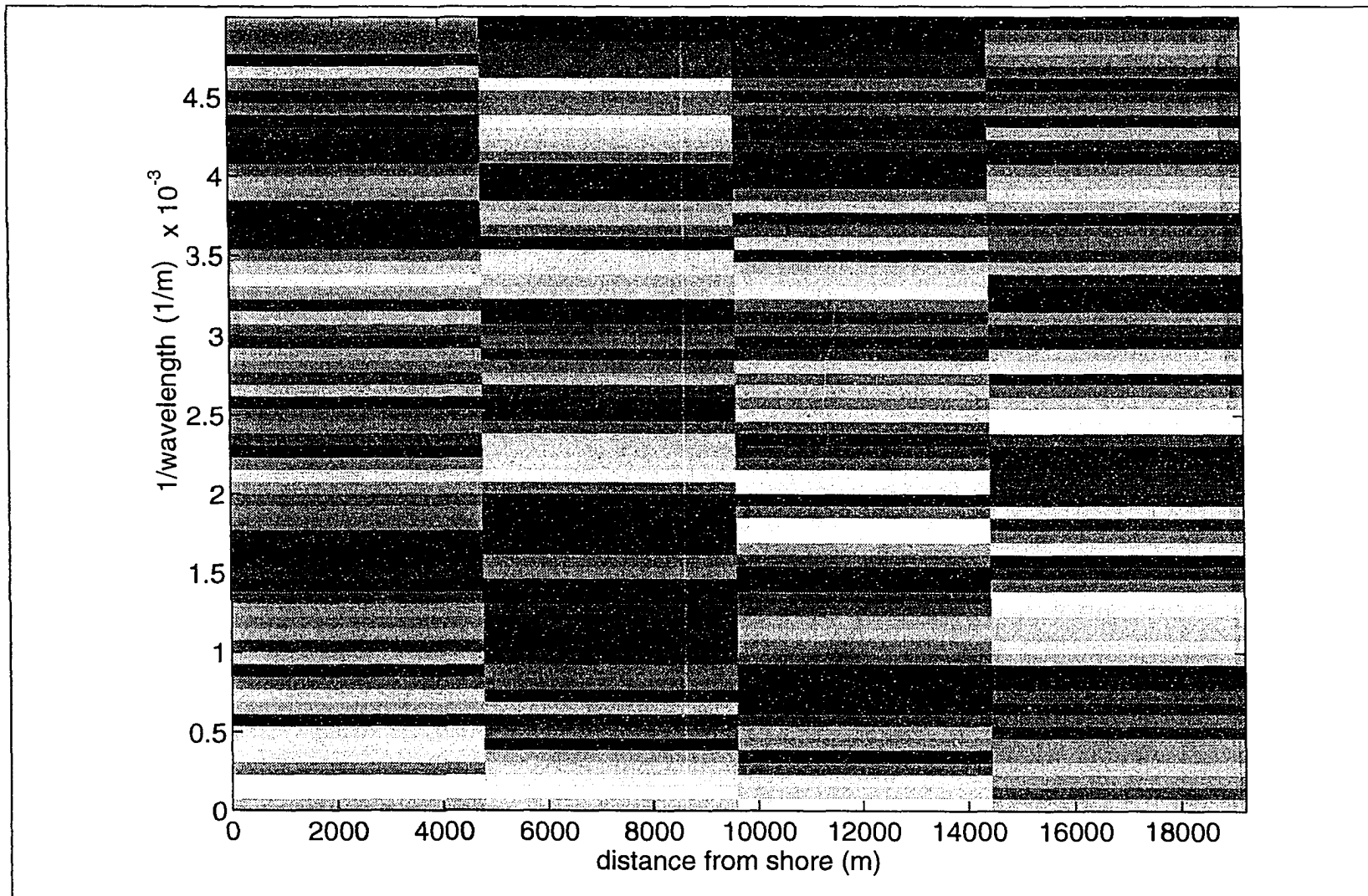
Figure 5.7. SAR based spectrogram summarizing the shift of the power spectra along a wave ray at Grays Harbor.

Intensity of the gray values represents power associated with any given wave length reciprocal and distance from shore.

**Energy Spectrum
Grays Harbor 160158
102/1992**
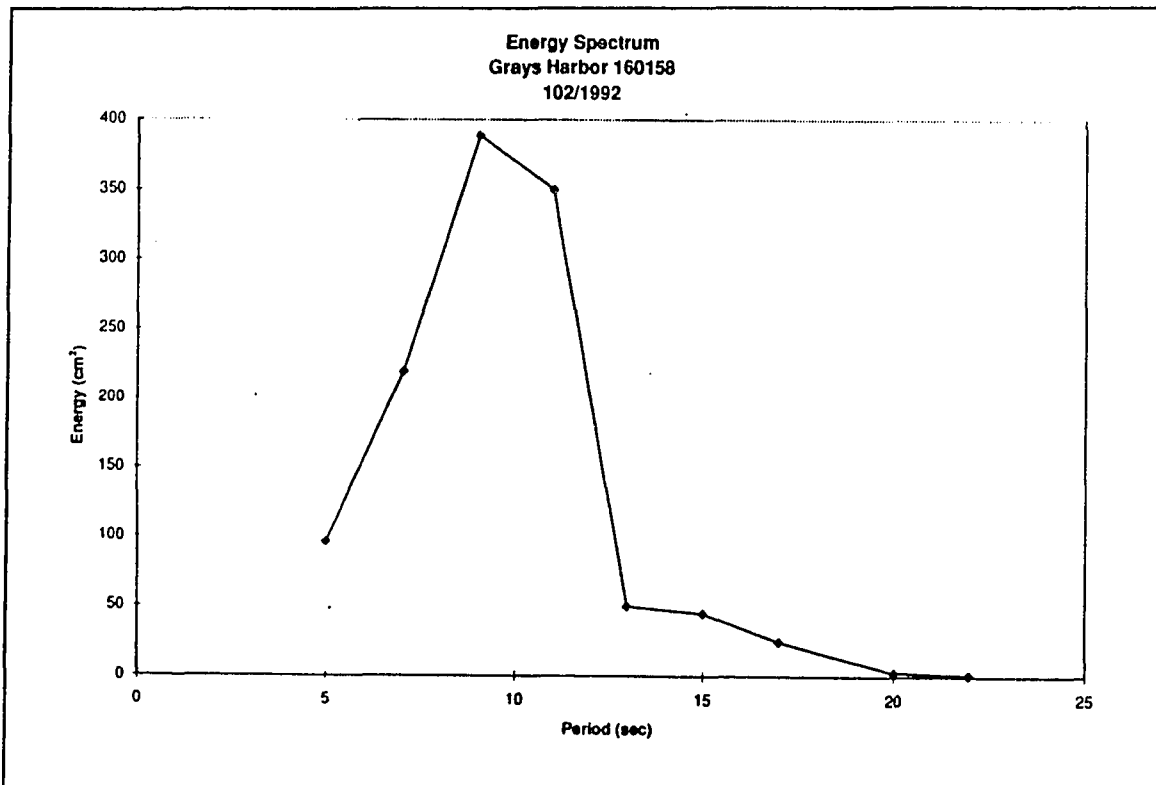
Figure 5.8. Power spectrum computed from actual measured data at Grays Harbor (Scripps Institute of Oceanography 1992).

The power spectra and spectrogram for Camden Bay appear to be more reasonable than those determined for Grays Harbor and Resurrection Bay. It is likely that because wave forms were easily detected on the raw data, the long wave domination was not present on the spectra. Unfortunately, measured data for this site were only observed visually, and the relatively long wave lengths indicated by the SAR spectrum were undetectable by the Camden Bay shipboard observers. Therefore spectra for the Camden Bay site could not be confirmed. The power spectrum and spectrogram for an image taken over Camden Bay, which contained well defined waveforms, is shown in Figures 5.9 and 5.10.
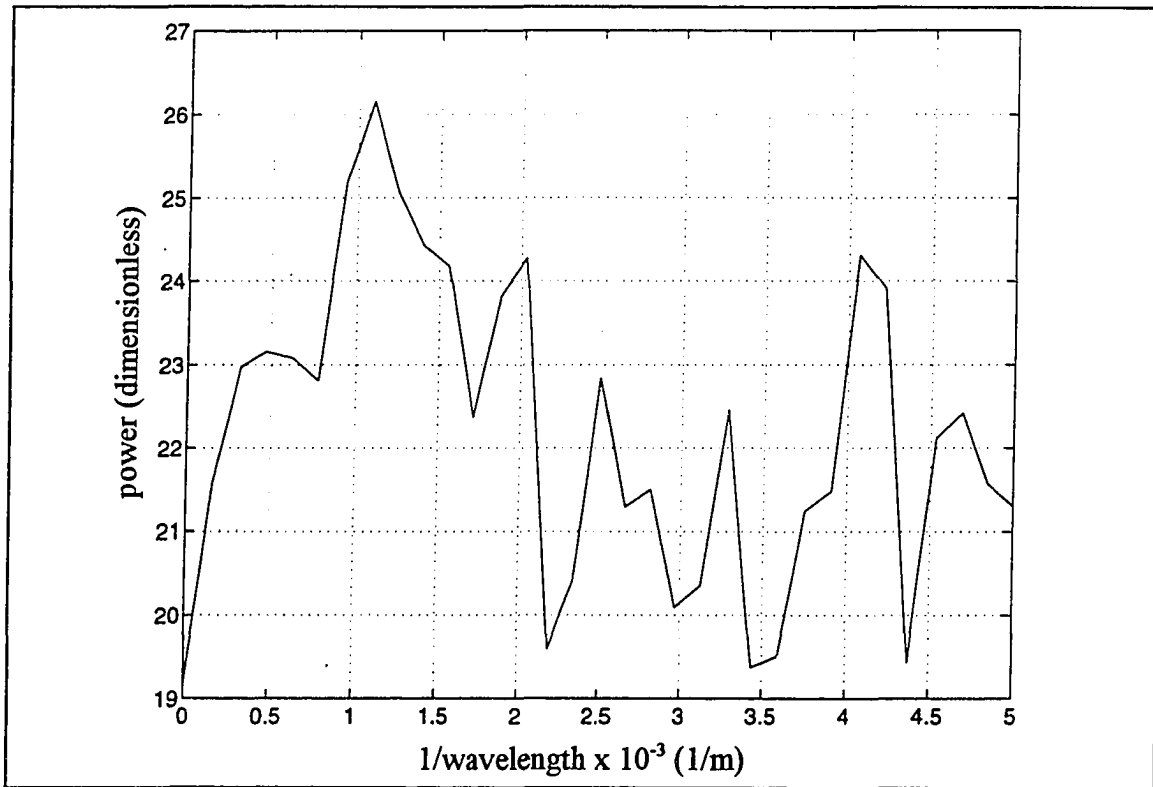
Figure 5.9. SAR based power spectra for Camden Bay do not exhibit the long wave length domination as do spectra computed for other sites.
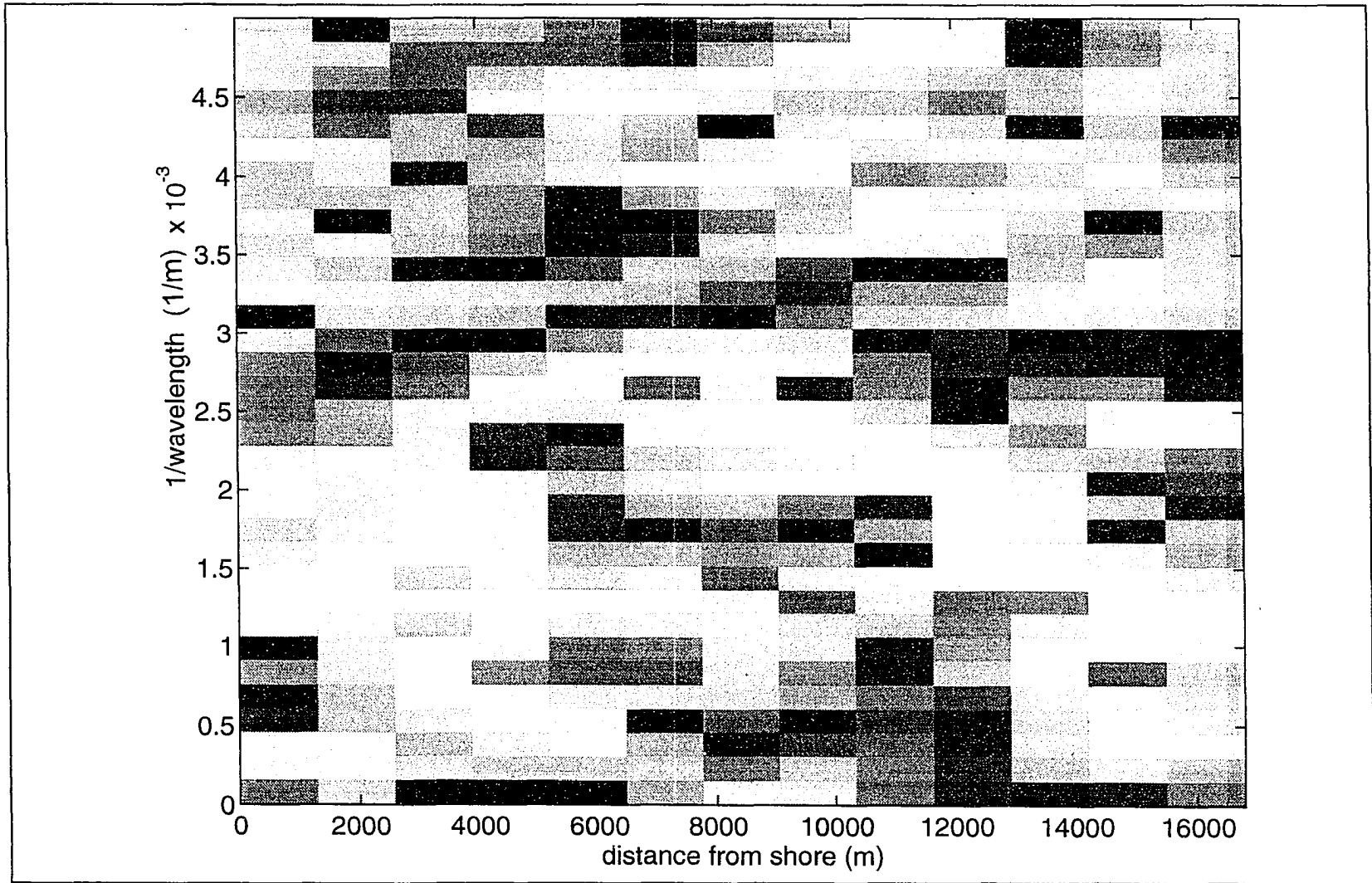
Figure 5.10. SAR based spectrogram for Camden Bay. Intensity of the gray values represents power associated with any given wave length reciprocal and distance from shore.

5.2.2 Averaged Wave Rays

Several parallel wave rays were constructed on the rotated SAR image and written to a text file. The text file was imported into Matlab where the power spectra were computed for each wave ray. The power spectra were then averaged together to reduce the effects of speckle in the raw image. The averaged power spectra, although somewhat more defined than the power spectra computed from the single wave ray, were dominated by the same long wavelength power as the single wave ray power spectra. This indicated that the averaging of several wave rays did not significantly improve results or reduce the random noise associated with SAR images. An example of the averaged wave spectra for the same sites as the single wave ray spectra, Grays Harbor and Camden Bay, are provided in Figures 5.11 and 5.12.
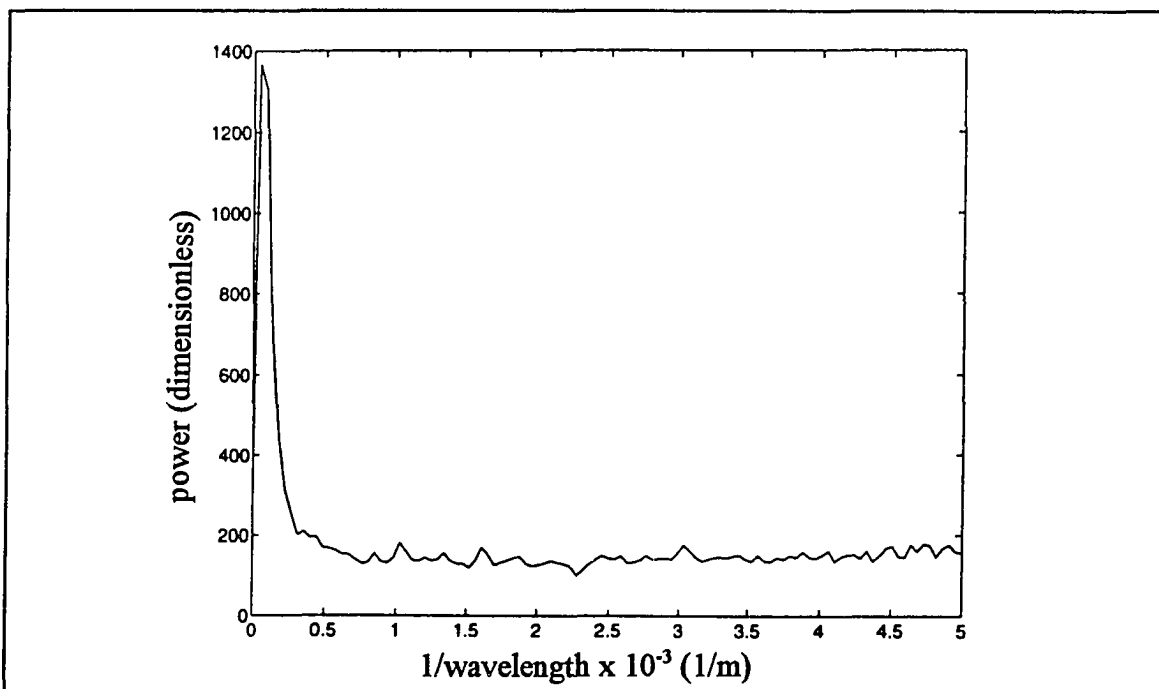
Figure 5.11. Averaged SAR based spectrum computed from several parallel wave rays at Grays Harbor.
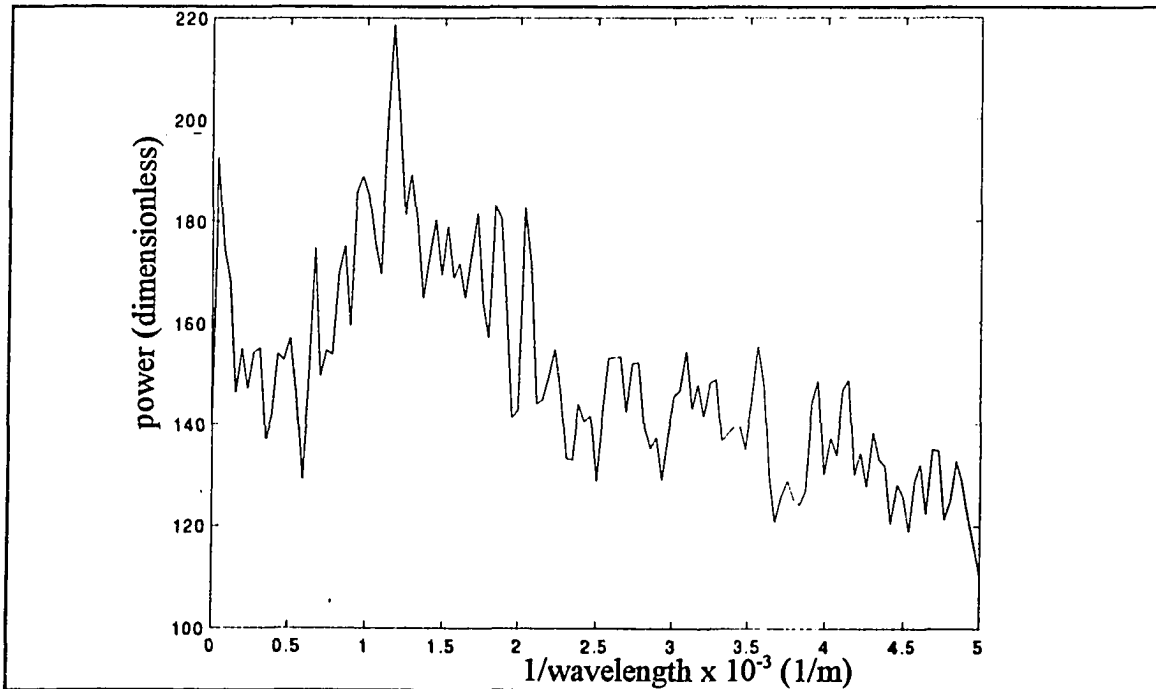
Figure 5.12. Average SAR based spectrum computed from several parallel wave rays at Camden Bay.

5.3 Wave Length and Wave Direction

Wave length was determined from the one-dimensional power spectra, the GPS wave product, and computations in Matlab, while wave direction was determined only from the wave product and Matlab. Because measured data from the Camden Bay site were visually observed by a shipboard journeyman, only relatively short waves were recorded. Therefore, the longer wave lengths estimated with SAR could not be compared to wave lengths measured at Camden Bay. However, SAR based wave lengths could be compared to measured wave lengths for Grays Harbor and Resurrection Bay.

5.3.1 One-Dimensional Power Spectra

Comparison of the SAR estimated one-dimensional power spectra with the measured wave spectra showed little similarity, and since the reciprocal of wave length comprises the horizontal scale of the SAR spectrum, correlation between SAR based wave lengths and measured wave lengths with this technique was poor. One explanation for the lack of similarity is that the one-dimensional spectrum constituted only a slice of data through the original image. If the slice were oriented such that it did not pass through the wave peaks measured by the buoy, discrepancies could exist. This is illustrated in Figure 5.13.

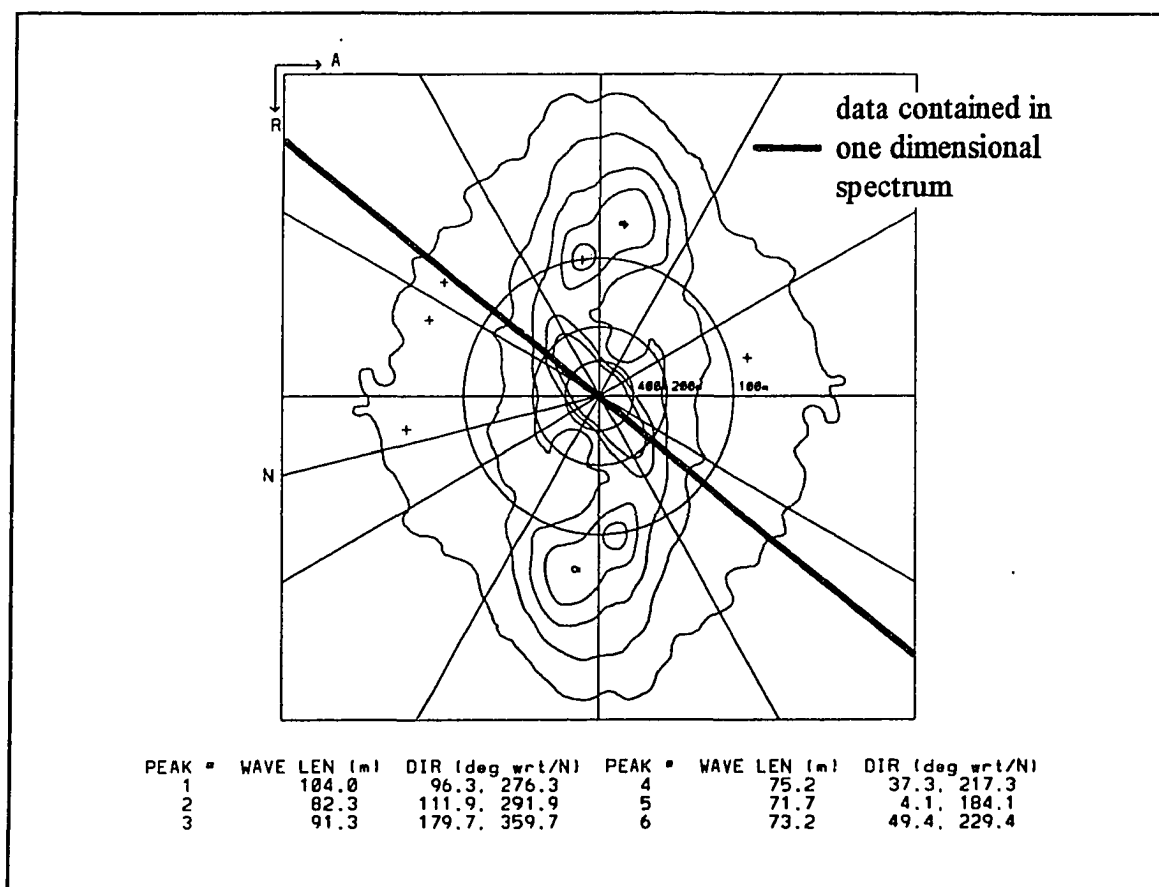| PEAK #	WAVE LEN (m)	DIR (deg wrt/N)	PEAK #	WAVE LEN (m)	DIR (deg wrt/N)
1	104.0	96.3, 276.3	4	75.2	37.3, 217.3
2	82.3	111.9, 291.9	5	71.7	4.1, 184.1
3	91.3	179.7, 359.7	6	73.2	49.4, 229.4

Figure 5.13. A one-dimensional power spectrum comprises only a slice of the two-dimensional spectrum.

5.3.2 GPS Generated Wave Spectra

The wave lengths obtained from the GPS wave products varied considerably when compared to the measured wave lengths, with the percent error of the SAR based wave lengths ranging from 12.5% to 47% in the Grays Harbor region, and errors exceeding this for Resurrection Bay. The wave products for which coincident wave buoy measurements could be obtained are included as Appendix B, and Appendix C contains the measured spectra. Although the 12.5% error would be practical for use in coastal engineering design, the 47% error exceeds the acceptable range. Several possible sources of error are listed below.

1) Averaging of the wave lengths over a large region

2) Use of the dispersion equation

3) Environmental factors

The GPS wave product provided an average wave length spectra over a 6.4 kilometer by 6.4 kilometer subscene of the original image. Because the sites were nearshore, wave parameters changed rapidly in this region. Therefore the average wave length over this region would be a poor representation of the actual wave length at a specific location within the subscene.

Assumptions inherent to the dispersion equation include straight, parallel bathymetric contours, linear waves, and the absence of a forcing function. Because the Grays Harbor site is only 45 miles north of the mouth of Columbia River, bathymetry of the area is complex. The presence of a mobile offshore bar near the entrance to the harbor increases errors involved with conversion of wave period to wave length via the dispersion equation in two ways: lack of straight and parallel bathymetric contours, and difficulty in determining water depth at the

buoy.

For use of the dispersion equation at Grays Harbor and Resurrection Bay, the water depth at the location of the buoy was found from NOAA charts 18502, and 16682 respectively. The depths indicated on the charts may not have coincided with the depths at the time the wave data were recorded. Since Resurrection Bay is a glacial fjord, water depths change rapidly with which reduces the accuracy of the dispersion equation. Unfortunately, without using the equation, SAR based parameters could not be compared to measured wave parameters.

The dispersion equation assumes the wave forcing, in this case the wind, no longer acted on the water surface. Because the wind was acting on the water surface when the SAR based estimations were made via the dispersion equation, some additional error may have been introduced.

Environmental factors which may have influenced the detection of ocean waves by SAR included the sediment content of the water, direction of wave propagation relative to the satellite path, and wind speed and direction. However, the effects of these factors were not considered.

5.3.3 Matlab Generated Wave Spectra

The SAR based wave lengths generated in Matlab resulted in error ranging from 34% to well over 100% for both Grays Harbor and Resurrection Bay. The wave products generated in Matlab are provided in Appendix D and the coincident measured spectra are provided in Appendix E. All the error sources identified in the GPS wave length determinations also apply to Matlab generated wave lengths except for a variation in the first: averaging wave lengths. For Matlab generated wave products, wave lengths were averaged over regions varying in size between

3.3 km x 3.3 km and 2.3 km x 2.4 km, rather than the 6.5 km x 6.5 km regions used by the GPS. Although the variable size of the Matlab generated products allowed averaging to be conducted over a smaller region centered over the buoys and enabled land to be excluded from the wave product computation, the detection of periodic features by the Fourier Transform was reduced due to the limited sample size. Some additional error was introduced into the Matlab generated wave lengths because the plots were not logarithmically scaled. This slightly inhibited accurate manual measurements of peak wave lengths, however the scale induced error was insignificant when compared to errors generated by other sources.

Wave direction was determined from wave products generated by both GPS and Matlab. Because wave direction was not measured at any of the sites, it was compared to the theoretically expected direction of wave propagation. At Grays Harbor waves should have traveled inshore and followed the bathymetric contours. The SAR estimated directions confirmed the expected travel direction as illustrated in Figure 5.14. In Resurrection Bay, the SAR estimated waves traveled up the fjord as anticipated by theory.

5.4 Wave Period and Duration of Storm Events

Because SAR based wave spectra were inaccurate, wave period and duration of storm events could not be determined.
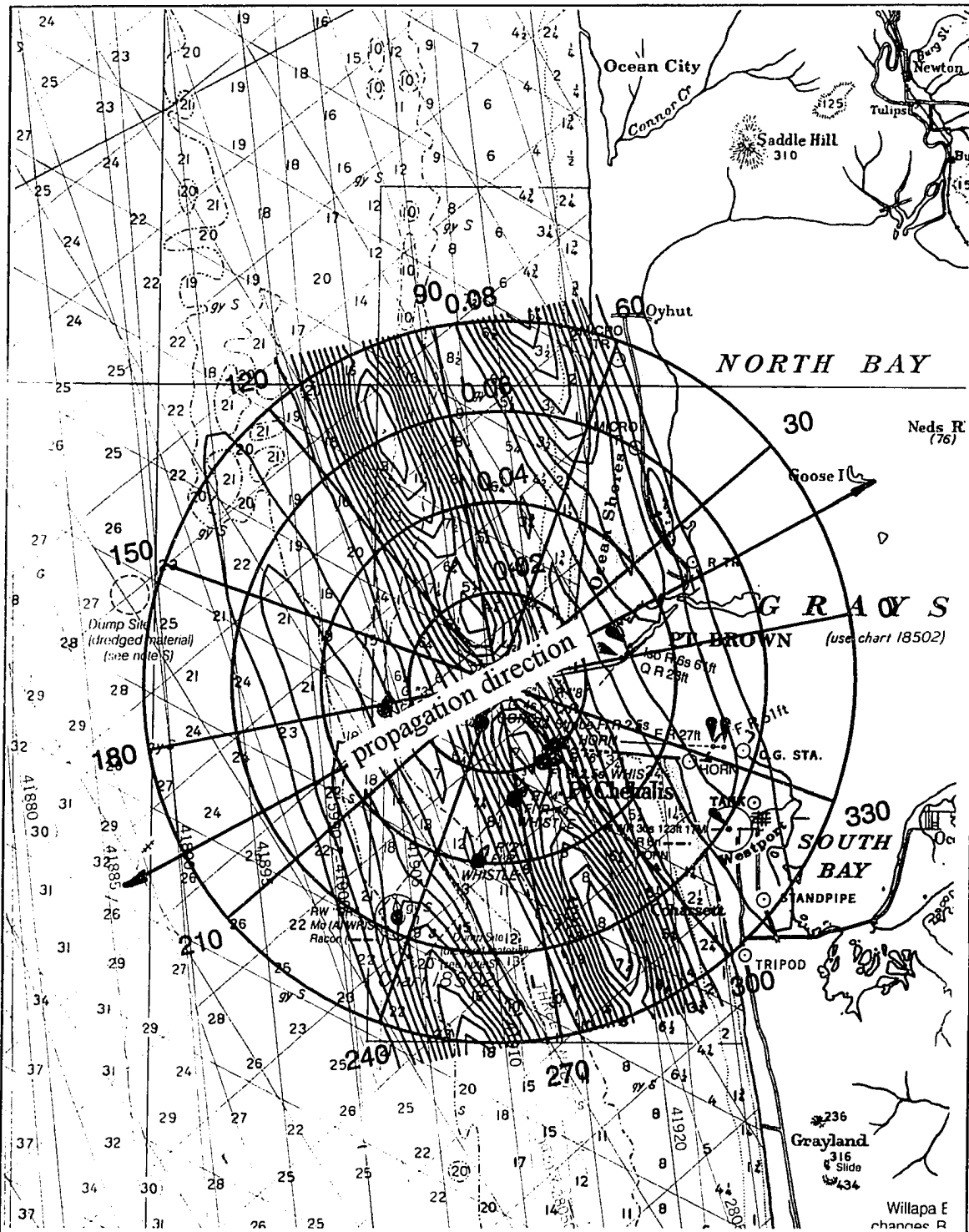
Figure 5.14. Bathymetric chart of Grays Harbor overlain by the Matlab generated

wave product, indicating SAR estimated wave propagation compares favorably with

theoretical directions of propagation.

Conclusions and

Future Research

The use of SAR to examine nearshore ocean waves proved to be of limited use to the coastal engineering field at this time. However, with continued research, it has the potential to improve the nearshore wave climate information available to coastal engineers. Although substantial error was discovered when SAR estimated wave lengths were compared to wave lengths calculated from measured wave data, the fact that wave lengths, although inaccurate, could actually be determined from SAR is promising. SAR based wave spectra were inaccurate, and therefore wave height, period, and duration of storm attack could not be determined from SAR images with the researched techniques. Wave directions extracted from SAR images do, however, appear to be reasonably accurate, and affirm the capacity of SAR data for estimation of some wave parameters. Due to the current errors associated with SAR based wave parameters, a SAR estimated wave climate cannot be incorporated into coastal design practice at this time.

107

Recommended future research involving SAR data for the determination of ocean wave parameters is listed below.

1) Compare offshore, rather than nearshore, measured wave data to SAR based wave spectra.

2) Evaluate SAR based wave climate during calm periods with little wind.

3) Evaluate the effect that environmental factors have on SAR detection of ocean waves.

4) Compare SAR based wave lengths to measured wave lengths or wave lengths computed via the dispersion for a deep water site at which the bathymetric characteristics meet the restrictions required by the dispersion equation.

5) Develop a tandem SAR platform which has temporal resolution on the order of seconds.

The first recommendation was made because of the complexity encountered in the evaluation of nearshore waves due to environmental conditions. Varied bathymetric conditions, and the presence of rivers affecting nearshore currents, sediment content, and wave propagation, all made it difficult to isolate wave parameters over a given region. By comparing SAR based wave spectra in an offshore region to wave spectra measured at that site, much of the complexity associated with the nearshore environment would be avoided. Possible sites for

this study include the National Oceanic and Atmospheric Administration (NOAA) buoys located in Prince William Sound and the Bering Sea. Although use of SAR in the nearshore environment is desirable for coastal engineering, the process of extracting wave spectra from SAR images must be more thoroughly understood offshore before the technology can be adapted for coastal waves.

The second recommendation, evaluation of SAR based wave parameters during calm periods, is made because all SAR images used in this study were conducted during storm events. By evaluating SAR based wave climate during calm periods, baseline SAR images could be obtained. From these baseline images, the environmental factors of bathymetry, currents, and sediment content could be more throughly understood. Then, by combining the baseline images with storm event images, the environmental effects could be removed and pure wave spectra obtained.

The third recommendation, which suggests evaluation of the mechanisms which SAR uses in the detection of ocean waves, ties closely to the second recommendation. Factors which may affect the way SAR images the ocean surface are wind speed and the capillary waves which it generates, direction of wave travel relative to the satellite path, sediment content of the water, and the presence of ice floes.

The fourth recommendation addresses the error involved in comparing wave length computed from measured wave period to SAR based wave lengths. One of two methods is suggested to reduce this error: conduct a detailed bathymetric survey to ensure the bathymetry of the study area complies with the assumptions of the dispersion equation and compare the SAR based wave length to the measured wave period via the dispersion equation, or actually measure wave lengths for direct comparison to the SAR based wave lengths. The first option is

most practical because a single wave buoy could be deployed to measure period, however the second technique would be more ideal because a direct comparison could be made. Wave length could be indirectly determined via a wave buoy array from which wave celerity and period could be directly measured. Wave length could then be computed with the wave equation which relates wave celerity to period and length. Although is method does not directly measure wave length, the wave equation would allow an accurate computation of wave length.

The fifth recommendation requires the development of a reconfigured SAR platform on which two SAR sensors would be mounted allowing temporal resolution on the order of seconds. By viewing the consecutive images acquired in this manner, wave period could be evaluated, and wave height could be interferometrically estimated.

References

ARCO. 1993. Visually observed wave data for West Camden Bay, Alaska.

Beal, R.C., D.G. Tilley, and F.M. Monaldo. 1983. Large- and small-scale spatial evolution of digitally processed ocean wave spectra from SEASAT Synthetic aperture radar. Journal of Geophysical Research 88:1761-1778.

Britch, Robert. Regional Program Manager, ENSR Consulting and Engineering. Interview with author in Anchorage, Alaska, 13 April 1994.

CERC (Coastal Engineering Research Center). 1984. Shore protection manual. Department of the Army. Waterways Experiment Station, Corps of Engineers. Washington, D.C.: U.S. Government Printing Office.

Dean, Robert G., and Robert A. Dalrymple. 1991. Water wave mechanics for engineers and scientists. Englewood Cliffs, New Jersey: Prentice-Hall.

DeSoto, Y., H. Tippens, T. Kotlarek, I. Hsu. 1991. Alaska SAR Facility archive and catalog subsystem user's guide. Pasadena, California: Jet Propulsion Laboratory. JPL D-5496.

Fu, Lee-Lueng, Project Scientist, Jet Propulsion Laboratory, Pasadena California. Phone interview with author, 17 August 1993.

Gonzalez, Rafael C., and Paul Wintz. 1987. Digital image processing. Reading, Massachusetts: Addison-Wesley Publishing Company.

Gower, J.F.R. 1983. 'Layover' in satellite radar images of ocean waves. Journal of Geophysical Research 88:7719-7720.

Hasselmann, Klaus, and Susanne Hasselmann. 1991. On the nonlinear mapping of an ocean wave spectrum into a synthetic aperture radar image spectrum and its inversion. Journal of Geophysical Research 96:10,713-10,729.

Hasselmann, K., R.K. Raney, W.J. Plant, W. Alpers, R.A. Shuchman, D.R. Lyzenga, C.L. Rufenach, and M.J. Tucker. 1985. Theory of synthetic aperture radar ocean imaging: A MARSEN view. Journal of Geophysical Research 90:4,659-4,686.

Kampion, Drew. 1989. The book of waves. Santa Barbara, California: Arpel Graphics, Inc. and Surfer Publications.

Khandekar, M.L. 1989. Operational analysis and prediction of ocean wind waves. Germany: Springer-Verlag.

Kwok, R., G. Cunningham. 1993. Alaska SAR Facility Geophysical Processor System data user's handbook: Ice motion product, ice type product, wave spectra product. Version 1.1. Pasadena, California: National Aeronautics and Space Administration, Jet Propulsion Laboratory. JPL D-9526.

Matlab. 1992. High-Performance numeric computation and visualization software. Natick, Massachusetts.

McDonald, Giles N. 1988. Riprap and armor stone. In Arctic coastal processes and slope protection design, ed. Chen and Leidersdorf, 190-207. New York: American Society of Civil Engineers.

Nottingham, Dennis, President, Peratrovich, Nottingham & Drage, Inc. Interview with author in Anchorage, Alaska, 15 April 1994.

Olmsted, Coert. 1993. Alaska SAR Facility scientific SAR user's guide. Fairbanks, Alaska: Geophysical Institute. ASF-SD-003.

PCI. 1993. Using PCI software, vols. 1 & 2, version 5.2 EASI/PACE. Ontario, Canada: PCI incorporated.

Reeves, Robert G., Anson Abraham, and David Landen, ed. 1975. Manual of remote sensing. Falls Church, Virginia: American Society of Photogrammetry.

Sabins, Flyod F. Jr. 1987. Remote sensing: Principles and interpretation, 2nd ed. New York: W.H. Freeman and Company.

Scripps Institute of Oceanography. 1992. Reduced buoy recorded wave data for Grays Harbor, Washington.

Serway, Raymond A. 1990. Physics for scientists & engineers with modern physics. Saunders Golden Sunburst Series. Philadelphia: Saunders College Publishing.

Smith, Harvey, State Coastal Engineer, Alaska Department of Transportation and Public Facilities. Interview with author in Anchorage, Alaska, 15 April 1994.

Smith, Orson, Coastal Engineer, Corps of Engineers. Interview with author in Anchorage, Alaska, 19 May 1993.

Smith, Orson, Coastal Engineer, Corps of Engineers. Interview with author in Anchorage, Alaska, 15 April 1994.

TOPEX/POSEIDON. Oceanography from space: The oceans and climate. Mission to planet Earth. National Aeronautics and Space Administration.

TOPEX/POSEIDON Science Working Team. 1991. TOPEX/POSEIDON Science Investigations Plan. Pasadena, California: Jet Propulsion Laboratory.

USCOE and IMS (United States Corps of Engineers and Institute of Marine Science). 1994. Reduced buoy recorded wave data for Grays Harbor, Washington.

Matlab Generated Wave

Product Algorithm

psdw2d: Algorithm to compute two dimensional power spectrum

```
function x=psdw2d(y1,nx,pol,string)

[a,b]=size(y1);

if (nargin<4)

    w=ones(nx,nx);

else

    if (string=='hanning')

        w=hann2(nx);

    else

        error('fourth argument must specify window type')

    end

end

u=(sum(sum(w.*w)));

z=zeros((2*nx)-1,(2*nx)-1);
```

```
nxn=((pol/100)*nx);

z1=zeros((nx/2),(2*nx)-1);

z2=zeros(nx,(nx/2));

z3=z2;

z4=z1;

if (rem(nx,2)==0)

    z3=z3(:,1:(nx/2)-1);

    z4=z4(1:(nx/2)-1,:);

end

i1=1;

j1=i1;

count=0;

while (i1+nx<=a)

    i2=i1+(nx-1);

    j1=1;

    while (j1+nx<=b)

        j2=j1+(nx-1);

        y3=w.*(y1(i1:i2,j1:j2)-mean(mean(y1(i1:i2,j1:j2))));

        y3=[z1:z2,y3,z3;z4];

        r1=fftshift(fft2(y3));

        z=z+(r1.*conj(r1));

        count=count+1;

        j1=j2-(nxn-1);

    end

    i1=i2-(nxn-1);

end

x=(1/(count*u))*(z);
```

HANN2(n): Algorithm to create a Hanning window for use in psdw2d

% Returns circularly symetric n by n 2-D Hanning window

%[CY - 6/92]

```
function w = hann2(n)

n1=([0:n-1]-(((n-1)/2)*ones(1,n)))/(n-1);

n2=n1';

n1=ones(size(n2))*n1;

n2=n1';

R=sqrt(n1.^2+n2.^2);

for i=1:n
    for j=1:n
        if (R(i,j)>.5)
            R(i,j)=.5;
        end
    end
end

w=0.5*(1+cos(2*pi*R));
```

GPS Generated Wave Products
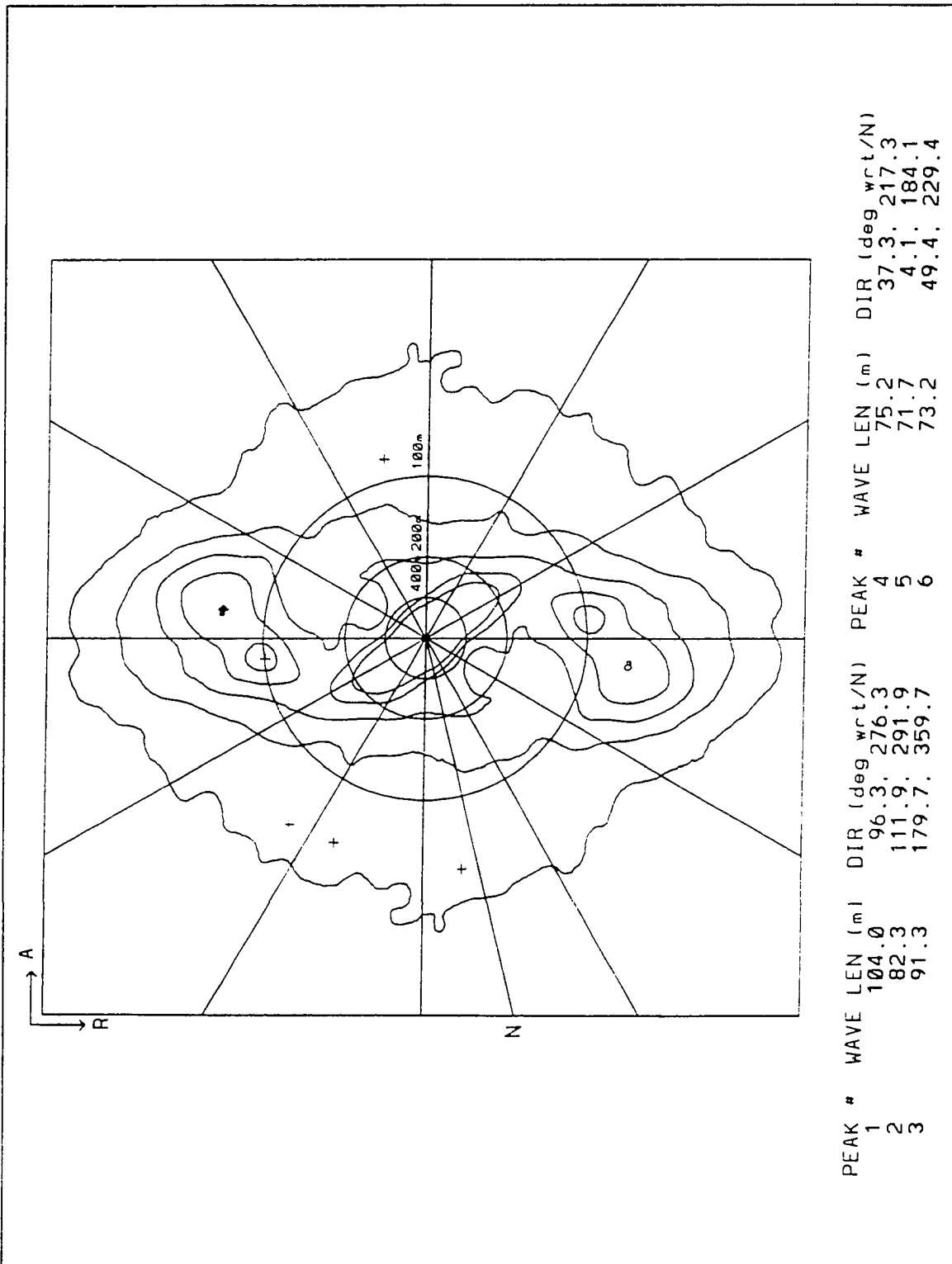
Figure Appendix:B-1. Grays Harbor, Image ID: 159550100 (39946100) Product
ID: 20965310 #8.
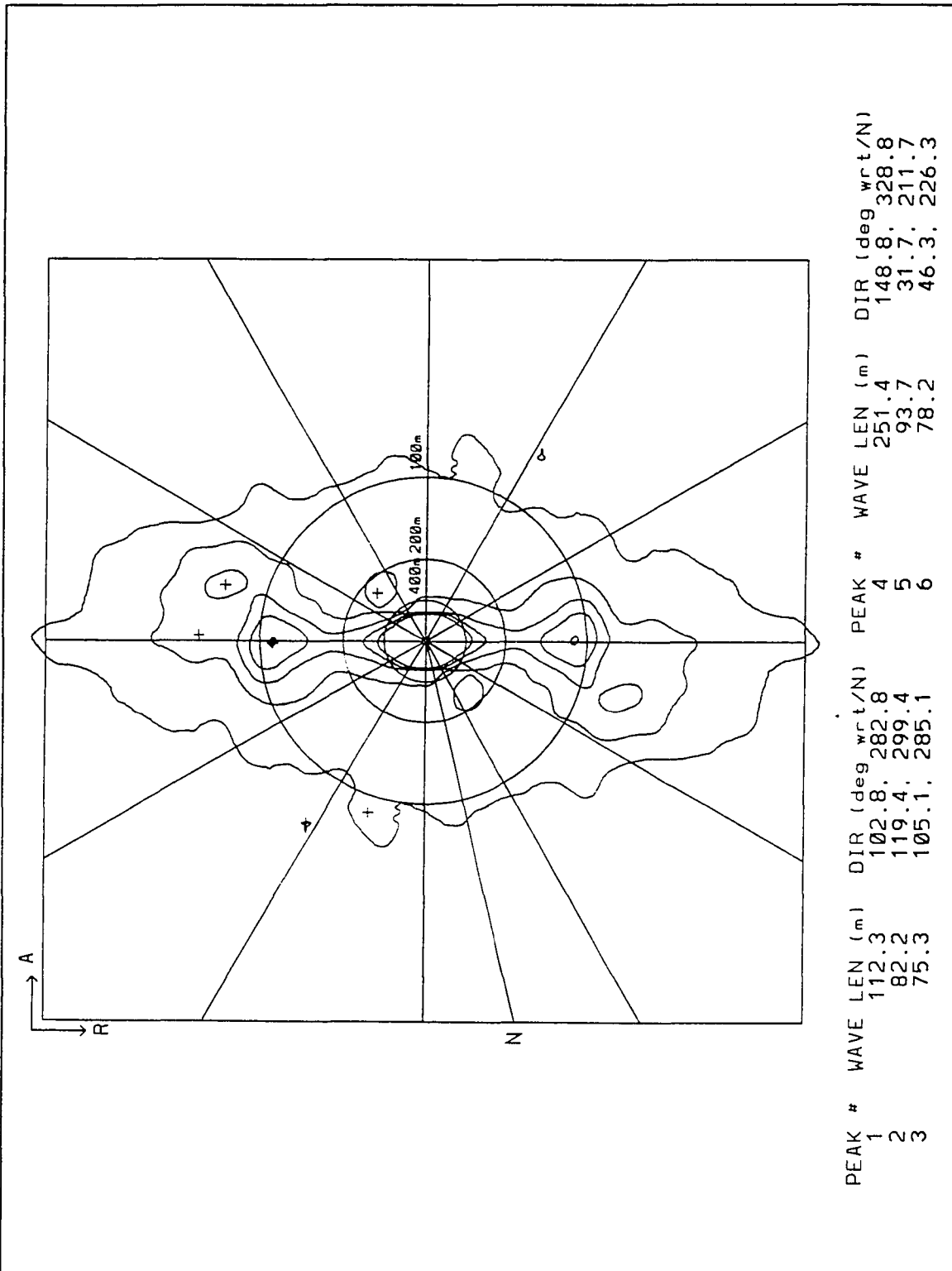
Figure Appendix:B-2. Grays Harbor. Image ID: 159548100 (39899100) Product ID: 20970310 #2.
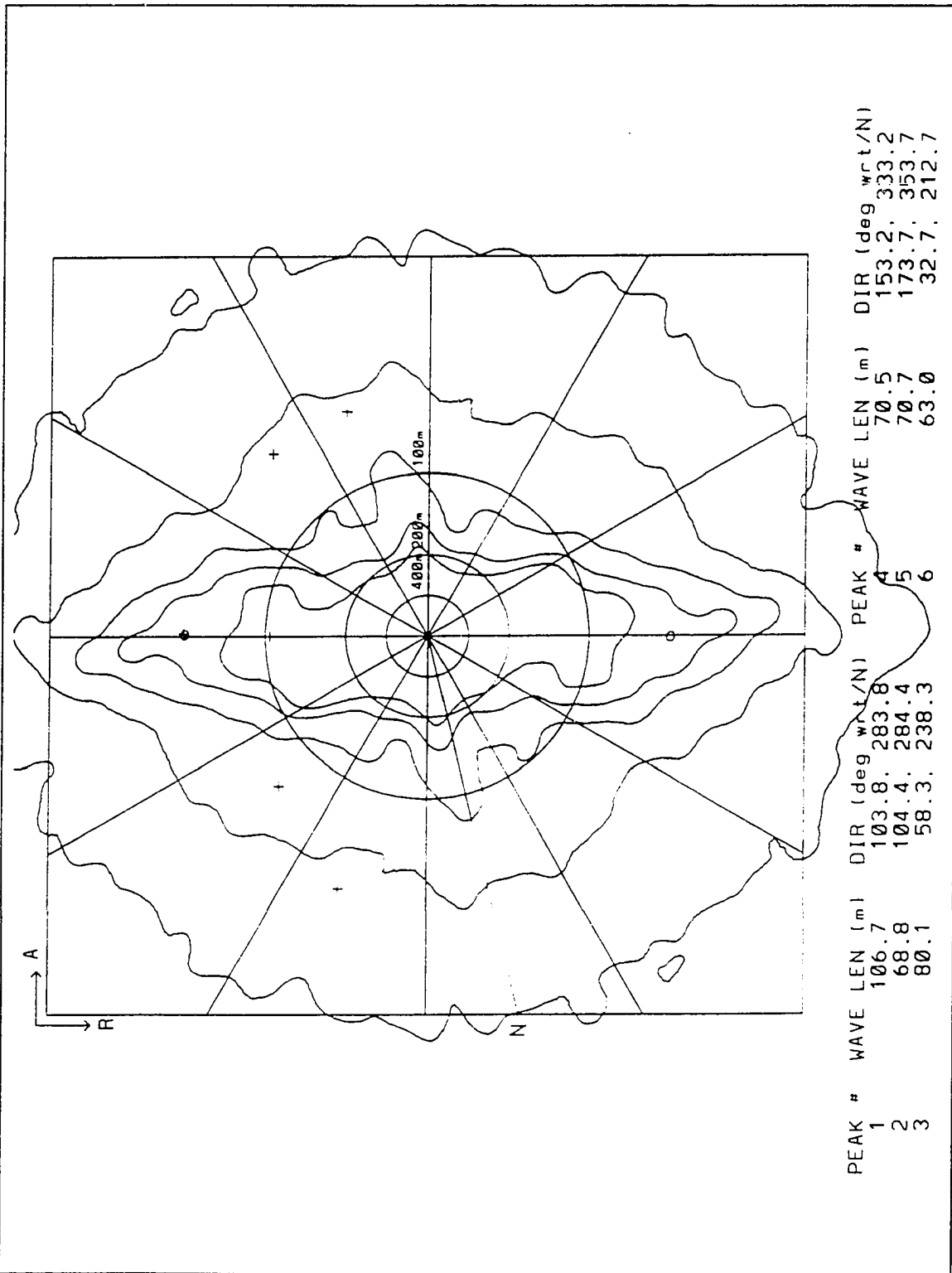
Figure Appendix:B-3. Grays Harbor. Image ID: 157547100 (68918100) Product ID: 20959310 #2.

Measured Wave Spectra Corresponding
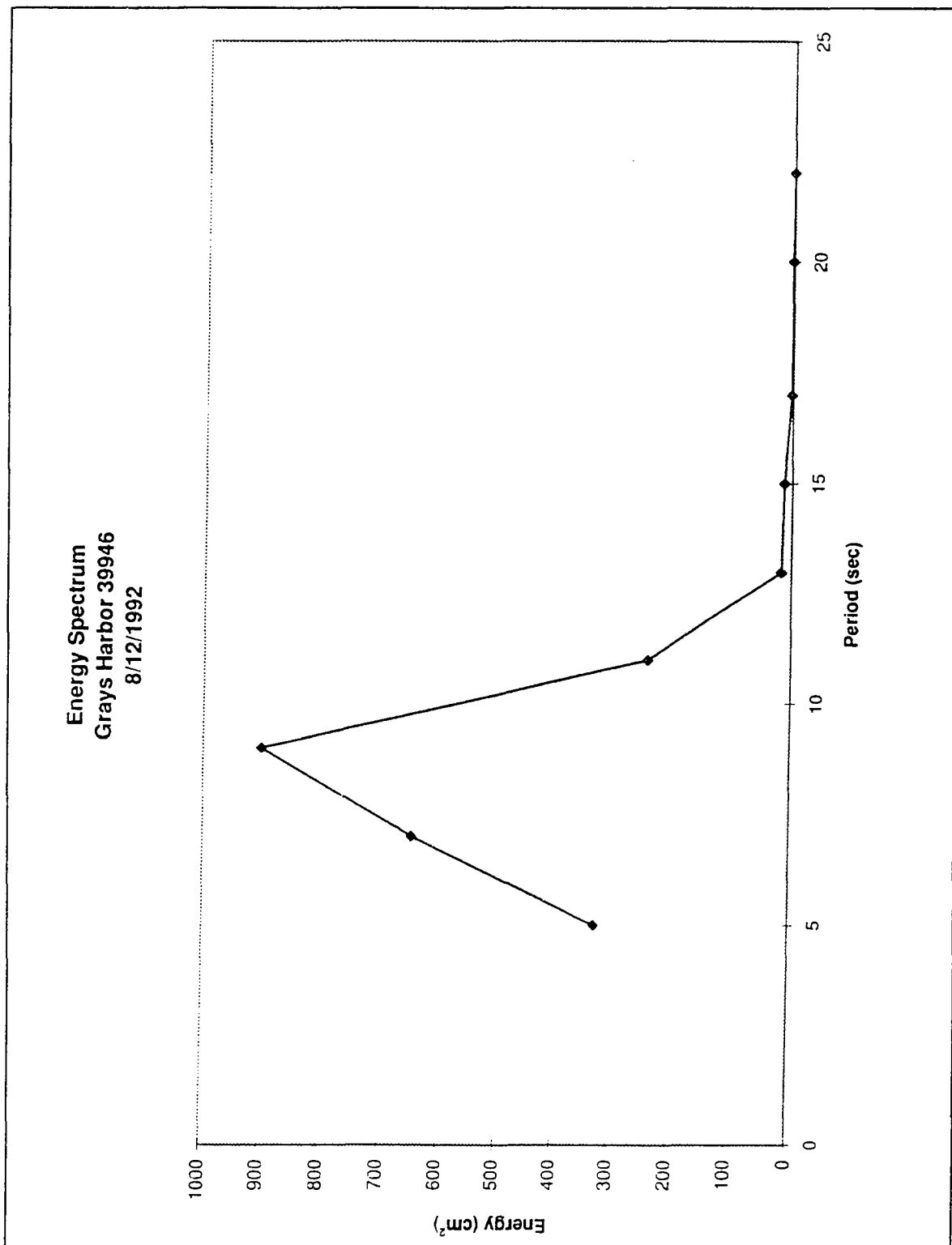
to GPS Generated Wave Products

Figure Appendix:C-1. Corresponds to Grays Harbor Image ID: 159550100 (39946100) (Scripps Institute of Oceanography 1992).
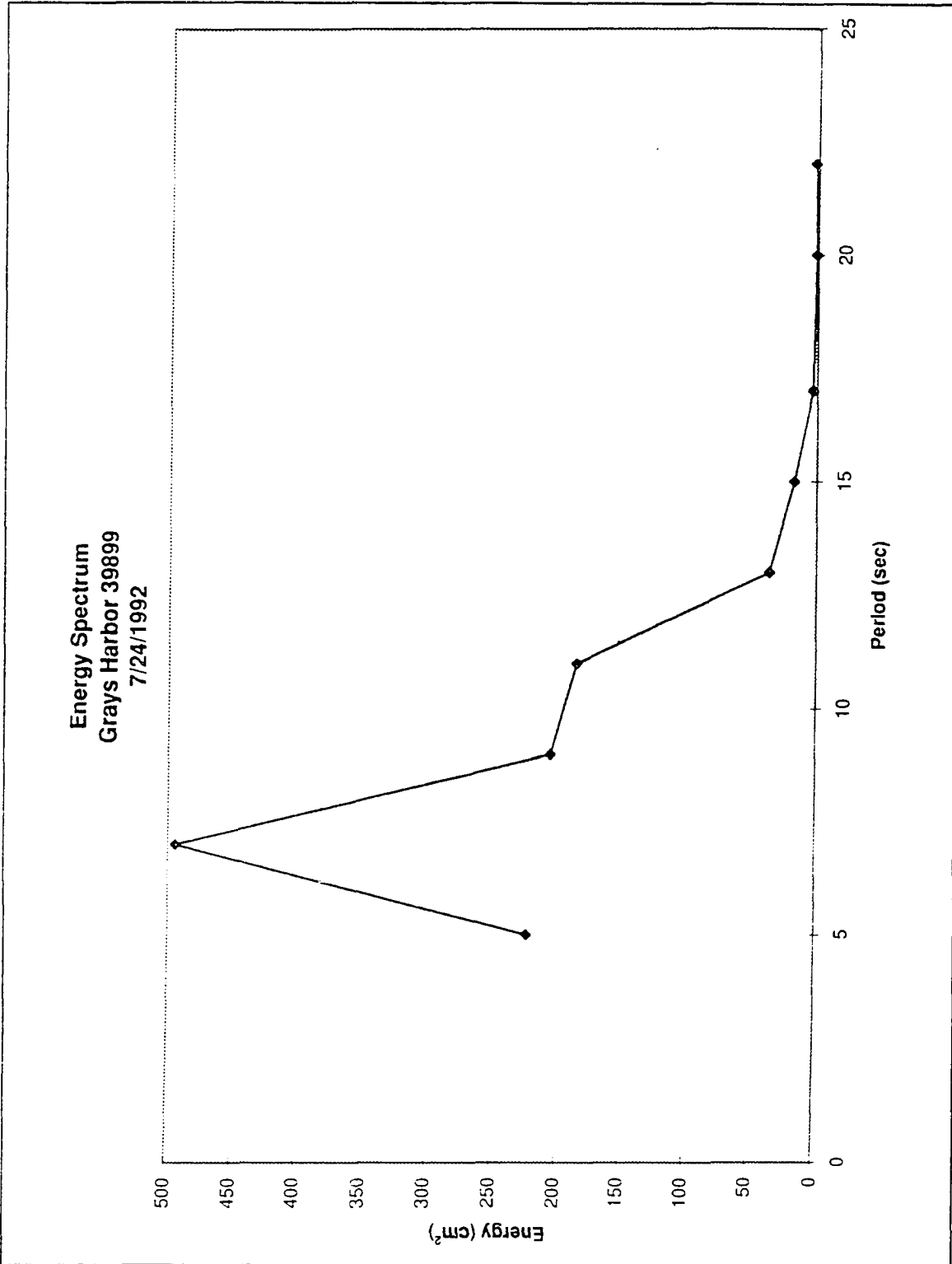
Figure Appendix:C-2. Corresponds to Grays Harbor Image ID: 159548100 (39899100) (Scripps Institute of Oceanography 1992).
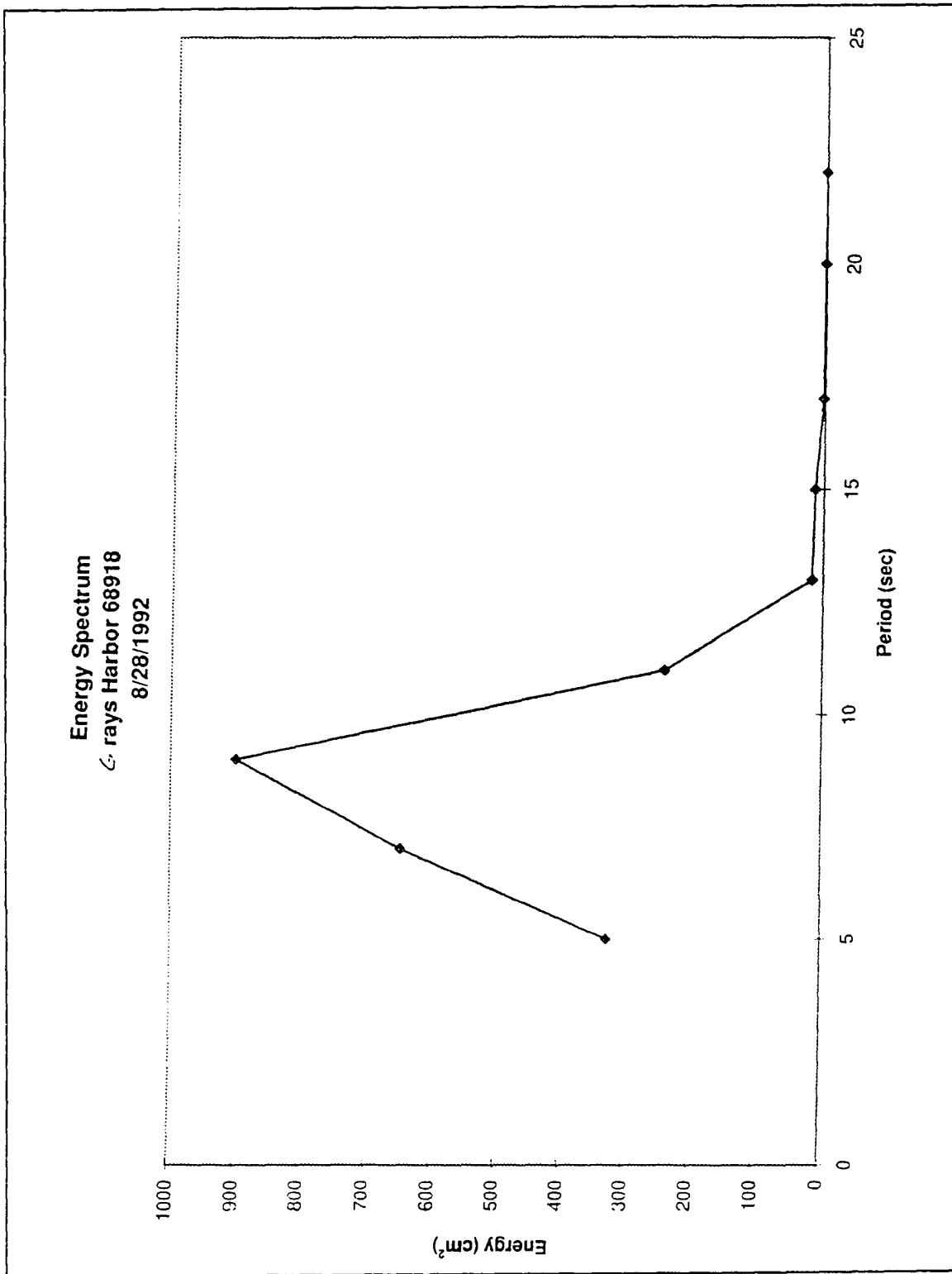
Figure Appendix:C-3. Corresponds to Grays Harbor Image ID: 157547100 (68918100) (Scripps Institute of Oceanography 1992).
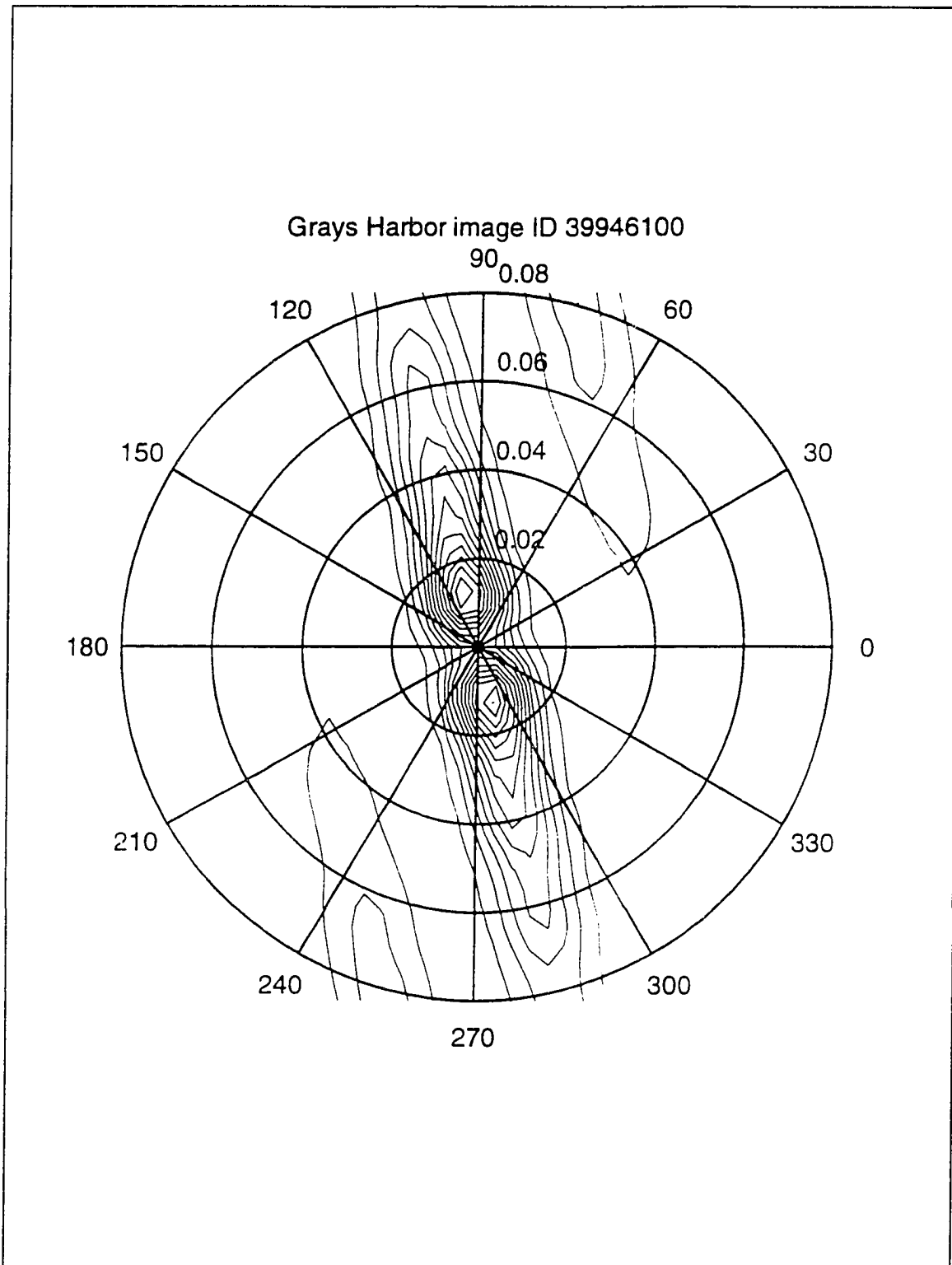
Matlab Generated Wave Products

Figure Appendix:D-1. Grays Harbor Image ID: 159550100 (39946100). Oriented relative to the raw image. Radial distance = 1/wave length (1/m).
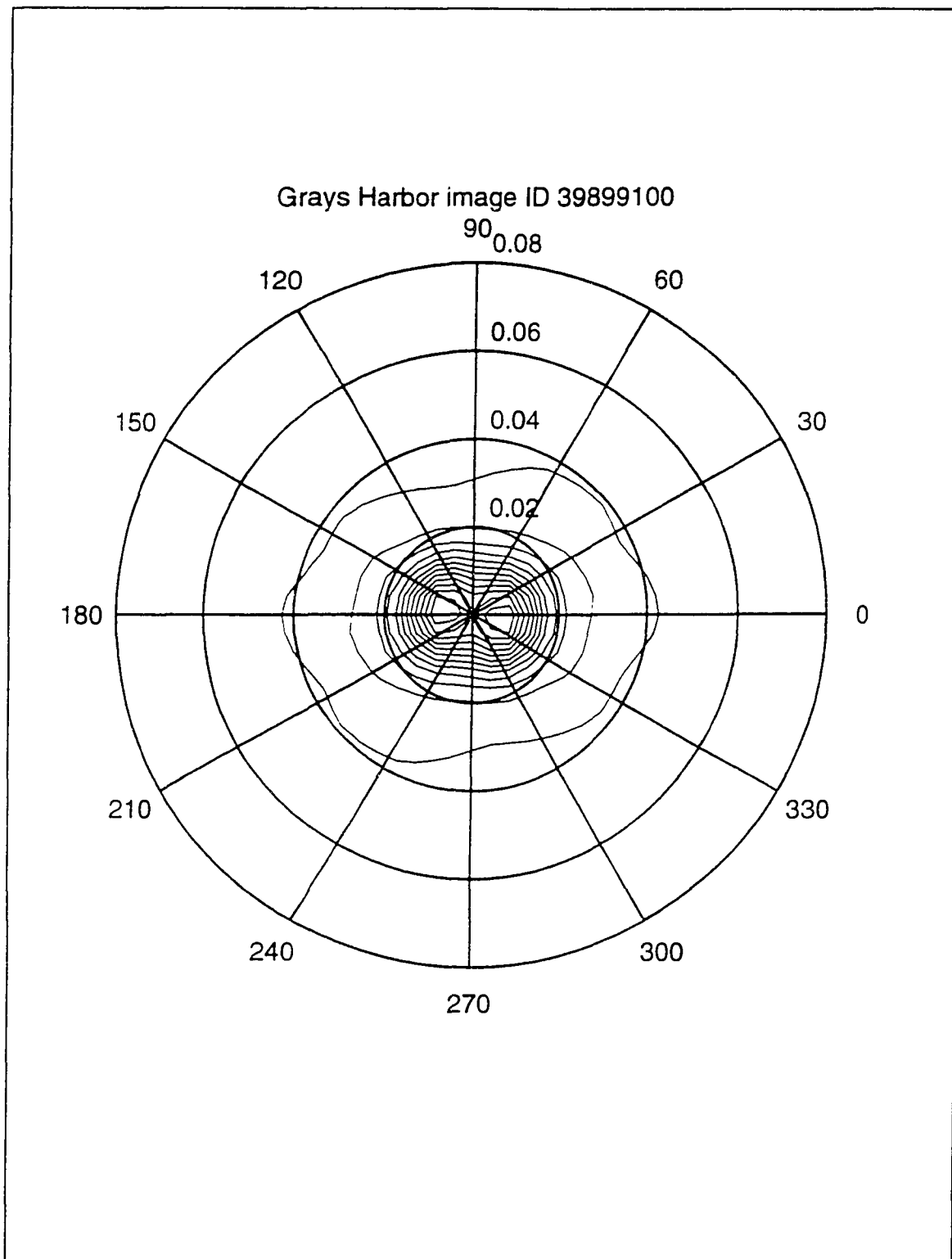
Grays Harbor image ID 39899100

Figure Appendix:D-2. Grays Harbor Image ID: 159548100 (39899100). Oriented relative to the raw image. Radial distance = 1/wave length (1/m).
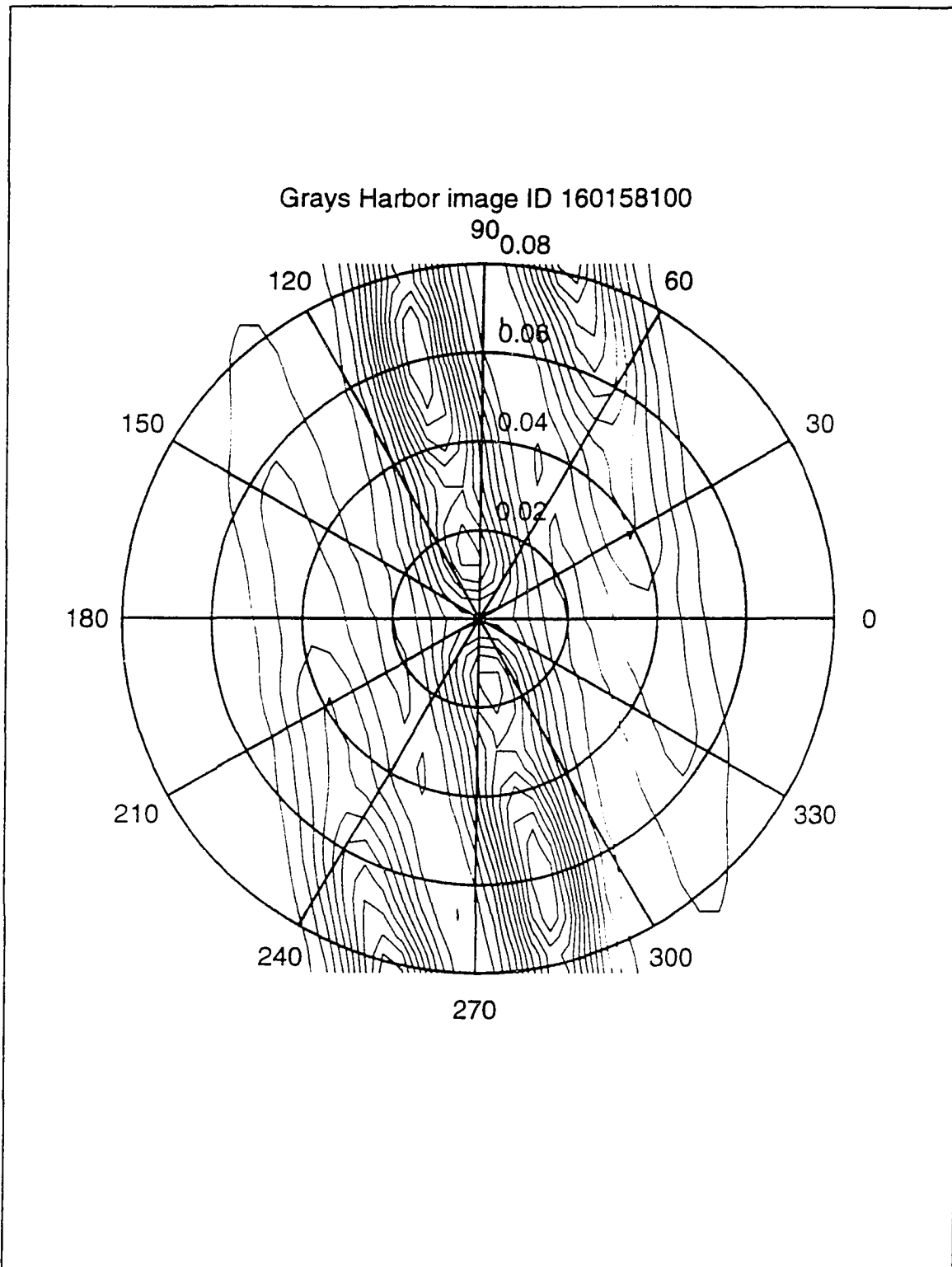
Grays Harbor image ID 160158100

Figure Appendix:D-3. Grays Harbor Image ID: 160158100. Oriented relative to the raw image. Radial distance = 1/wave length (1/m).

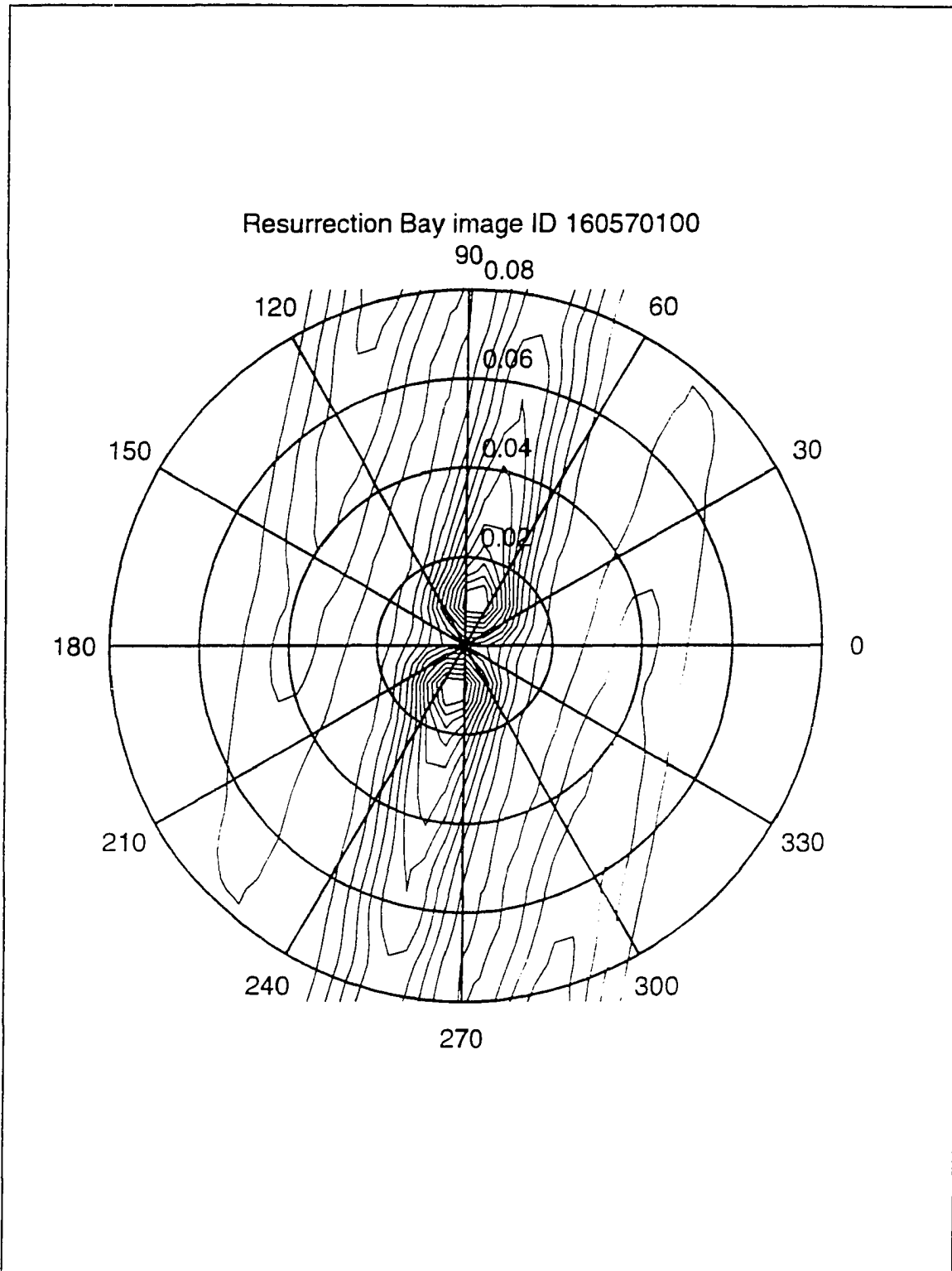**Figure Appendix:D-4.** Resurrection Bay Image ID: 160570100. Oriented relative

to the raw image. Radial distance = 1/wave length (1/m).

Measured Wave Spectra Corresponding

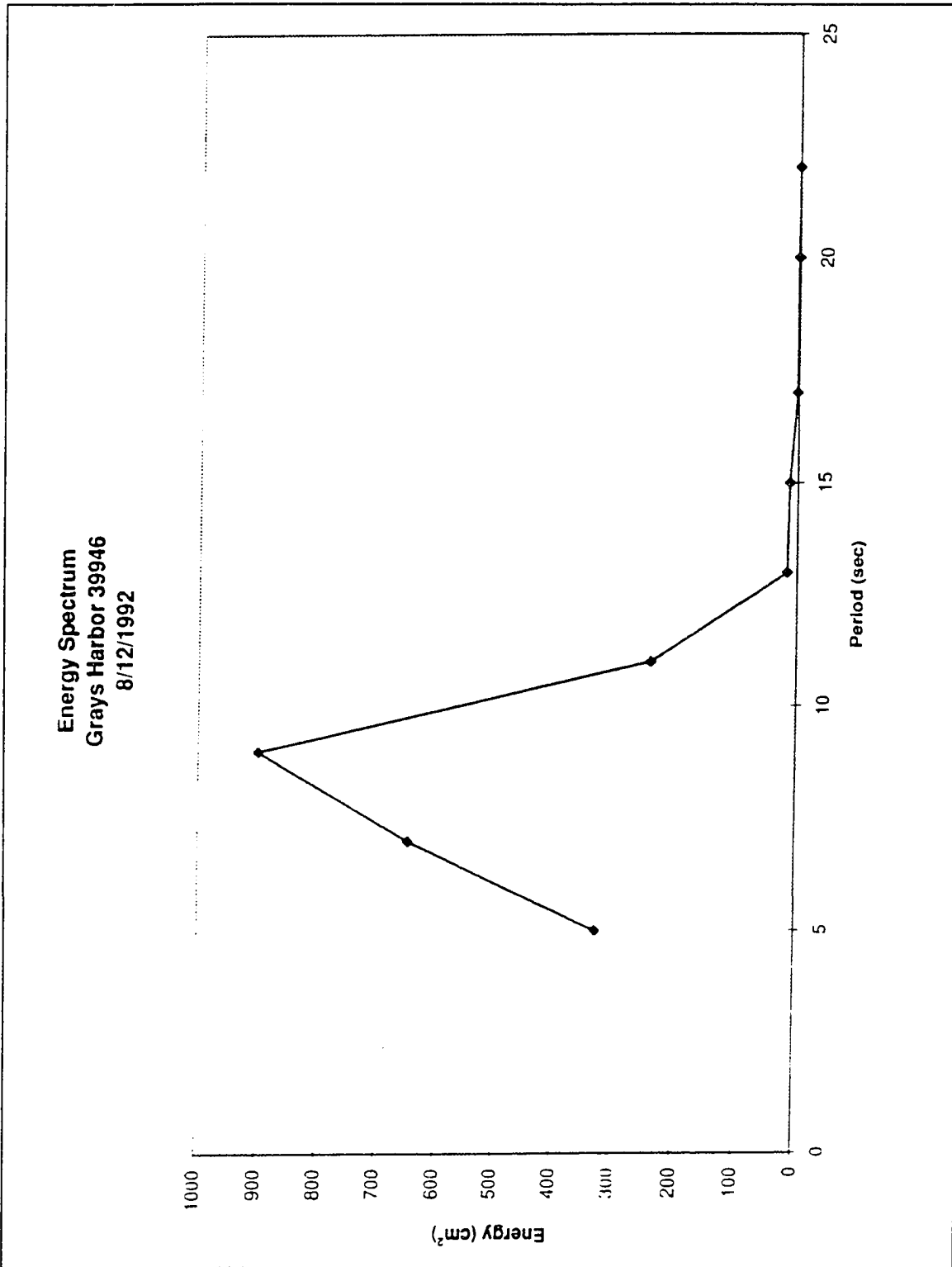# to Matlab Generated Wave Products

131

Figure Appendix:E-1. Corresponds to Grays Harbor Image ID: 159550100 (39946100) (Scripps Institute of Oceanography 1992).
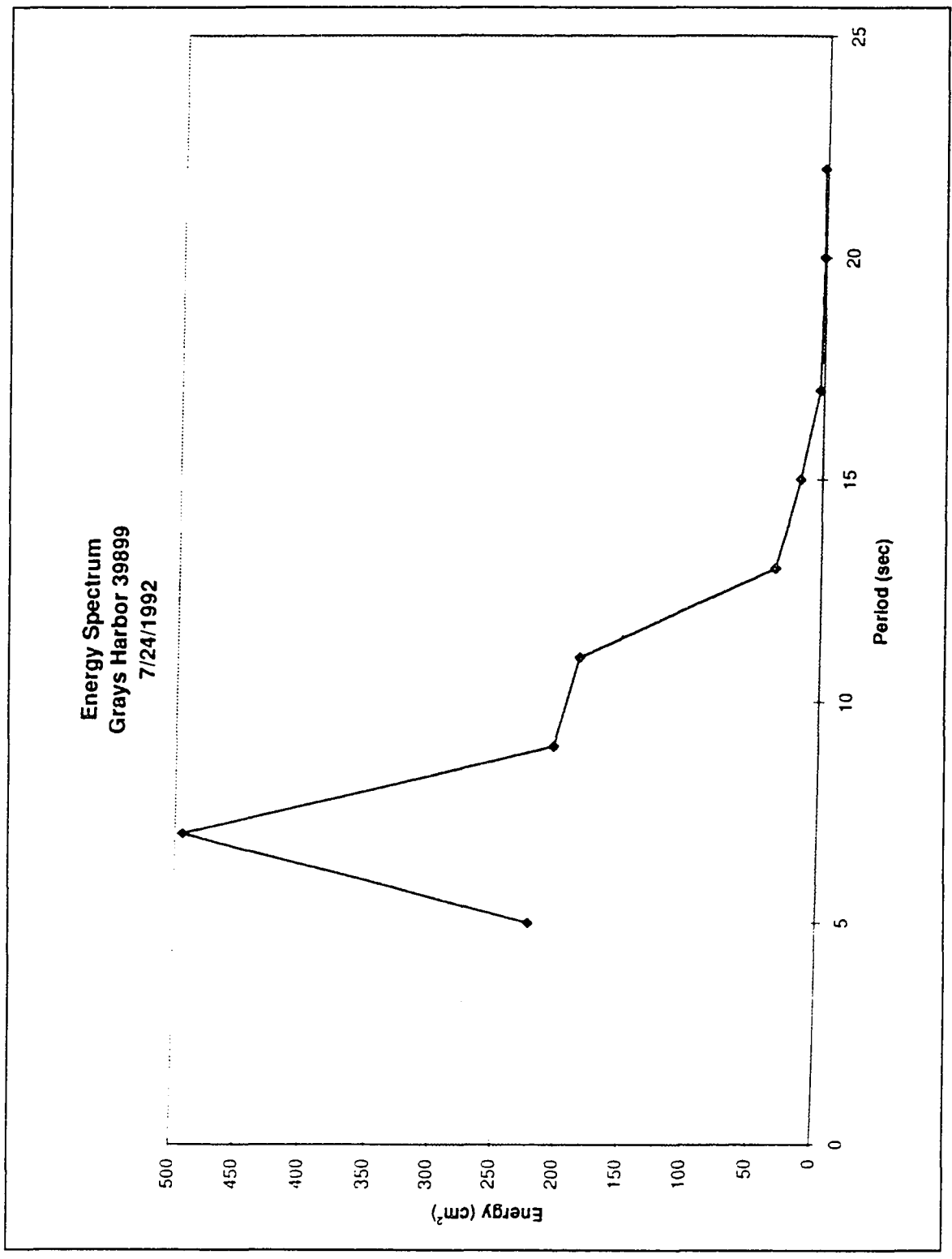
Figure Appendix:E-2. Corresponds to Grays Harbor Image ID: 159548100 (39899100)(Scripps Institute of Oceanography 1992).
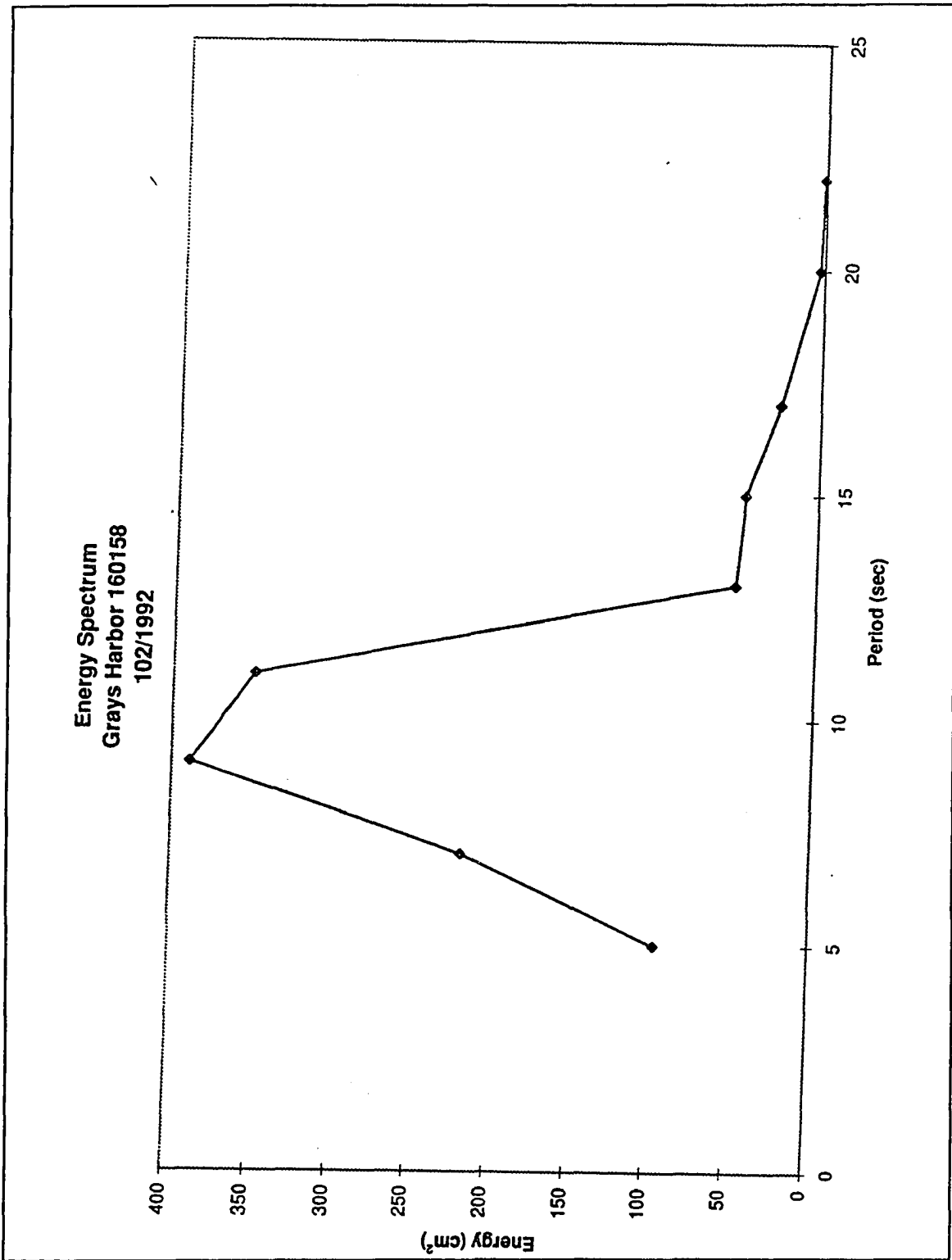
Figure Appendix:E-3. Corresponds to Grays Harbor Image ID: 159548100 (39899100) (Scripps Institute of Oceanography 1992).

WAVE SPECTRUM

ENERGY DENSITY, (m²s)

FREQUENCY, (Hz)

3 NOV 1994   2000 Alaska Std. Time
1280 Seaward Skimmer Buoy

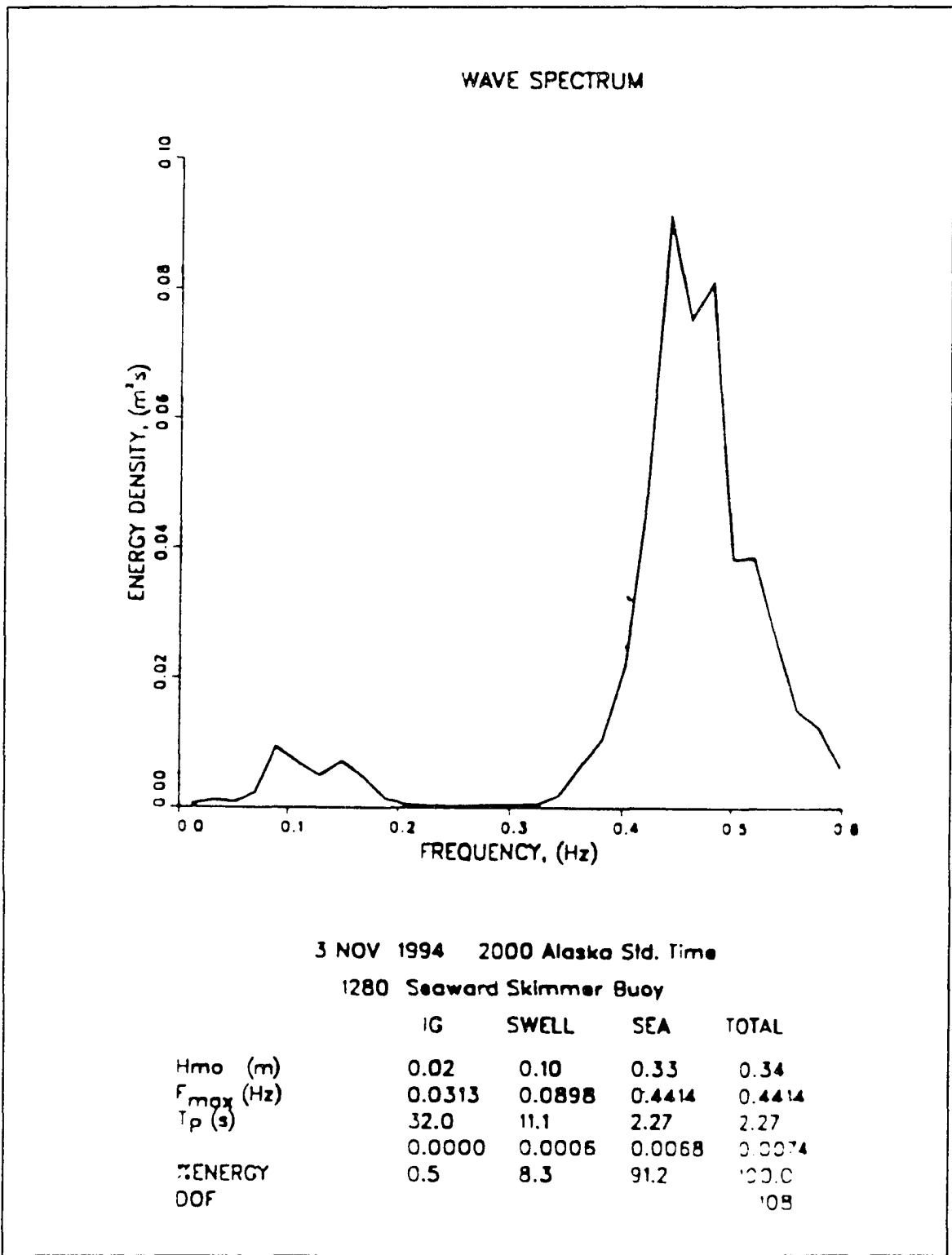|	IG	SWELL	SEA	TOTAL
Hmo (m)	0.02	0.10	0.33	0.34
Fmax (Hz)	0.0313	0.0898	0.4414	0.4414
Tp (s)	32.0	11.1	2.27	2.27
	0.0000	0.0006	0.0068	0.0074
%ENERGY	0.5	8.3	91.2	100.0
DOF				108

Figure Appendix:E-4. Corresponds to Resurrection Bay Image ID: 160570100 (USCOE and IMS 1994).